②

AD-A221 080

WRDC-TR-89-1150

ANALYSIS OF PHASE RETRIEVAL IN ACTIVE IMAGING

J.R. FIENUP
Environmental Research Institute of Michigan
Advanced Concepts Divison
P.O. Box 8618
Ann Arbor, MI 48107-8618

FEBRUARY 1990

Final Report for Period August 1986 - November 1988
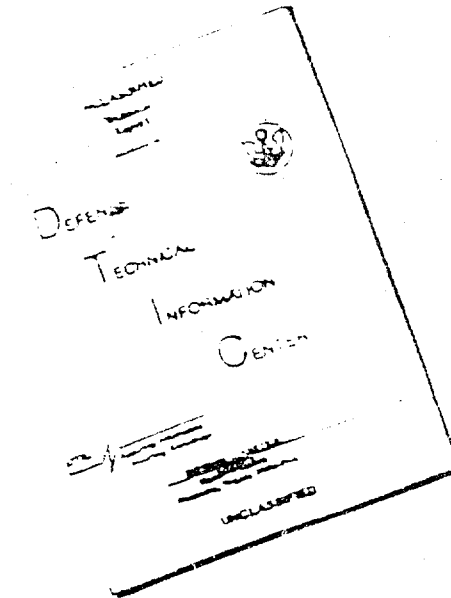
DTIC
ELECTE
JUN 0 5 1990
S E D

90 06 04 108

DISCLAIMER NOTICE

THIS DOCUMENT IS BEST QUALITY AVAILABLE. THE COPY FURNISHED TO DTIC CONTAINED A SIGNIFICANT NUMBER OF PAGES WHICH DO NOT REPRODUCE LEGIBLY.

NOTICE

When Government drawings, specifications, or other data are used for any purpose other than in connection with a definitely Government-related procurement, the United States Government incurs no responsibility or any obligation whatsoever. The fact that the government may have formulated or in any way supplied the said drawings, specifications, or other data, is not to be regarded by implication, or otherwise in any manner construed, as licensing the holder, or any other person or corporation; or as conveying any rights or permission to manufacture, use, or sell any patented invention that may in any way be related thereto.
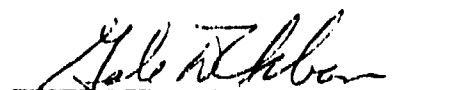
This report is releasable to the National Technical Information Service (NTIS). At NTIS, it will be available to the general public, including foreign nations.

This technical report has been reviewed and is approved for publication.

ROBERT H. FETNER, Capt, USAF
Project Engineer
Electro-Optics Techniques Group
Electro-Optics Branch

DONALD L. TOMLINSON, Chief
Electro-Optics Techniques Group
Electro-Optics Branch

FOR THE COMMANDER

GALE D. URBAN, Chief
Electro-Optics Branch
Mission Avionics Division

If your address has changed, if you wish to be removed from our mailing list, or if the addressee is no longer employed by your organization please notify WRDC/AARI-2 WPAFB, OH 45433-6543 to help us maintain a current mailing list.

Copies of this report should not be returned unless return is required by security considerations, contractual obligations, or notice on a specific document.

REPORT DOCUMENTATION PAGE

1a. REPORT SECURITY CLASSIFICATION Unclassified		1b. RESTRICTIVE MARKINGS (none)		
2a. SECURITY CLASSIFICATION AUTHORITY		3. DISTRIBUTION/AVAILABILITY OF REPORT Approved for public release; distribution unlimited		
2b. DECLASSIFICATION/DOWNGRADING SCHEDULE				
4. PERFORMING ORGANIZATION REPORT NUMBERS(S) 167400-133-F		5. MONITORING ORGANIZATION REPORT NUMBER(S) WRDC-TR-89-1150		
6a. NAME OF PERFORMING ORGANIZATION Environmental Research Institute of Michigan	6b. OFFICE SYMBOL (If applicable)	7a. NAME OF MONITORING ORGANIZATION Avionics Laboratory (WRDC/AARI) Wright Research and Development Center		
6c. ADDRESS (City, State, and ZIP Code) P.O. Box 8618 Ann Arbor, MI 48107		7b. ADDRESS (City, State, and ZIP Code) Wright-Patterson AFB, OH 45433-6543		
8a. NAME OF FUNDING /SPONSORING ORGANIZATION Air Force Weapons Laboratory	8b. OFFICE SYMBOL (If applicable) AROB	9. PROCUREMENT INSTRUMENT IDENTIFICATION NUMBER F33615-83-C-1046		
8c. ADDRESS (City, State, and ZIP Code) Kirtland AFB, NM 87117-6008		10. SOURCE OF FUNDING NUMBERS		

PROGRAM ELEMENT NO.	PROJECT NO.	TASK NO.	WORK UNIT ACCESSION NO.
61101F	ILIR	83	05

11. TITLE (Include Security Classification)

Analysis of Phase Retrieval in Active Imaging

12. PERSONAL AUTHOR(S)

J.R. Fienup

13a. TYPE OF REPORT Final Technical	13b. TIME COVERED FROM 8/1/86 TO 11/7/88	14. DATE OF REPORT (Year, Month, Day) 1990 February	15. PAGE COUNT 167

16. SUPPLEMENTARY NOTATION

This research was partially funded by the in-house independent research fund.

17. COSATI CODES			18. SUBJECT TERMS (Continue on reverse if necessary and identify by block number)
FIELD	GROUP	SUB-GROUP	Phase Retrieval Atmospheric turbulence
20	06		Image reconstruction Intensity interferometry
20	14		Speckle Imaging correlography

19. ABSTRACT (Continue on reverse if necessary and identify by block number)

This report describes a collection of research tasks which develop techniques to reconstruct fine-resolution images of satellites coherently illuminated by lasers Two major imaging modes were developed. In the first, called imaging correlography, an incoherent image of the coherently illuminated target is reconstructed from multiple realizations of the intensity of the nonimaged (aperture-plane) laser speckle pattern backscattered from the target. In the second mode, a coherent image of the target is reconstructed from a single realization of the nonimaged laser speckle pattern. In the latter mode, reconstruction methods were developed for the case of a target which contains a strong glint (or glints) and for the case in which one has partial information about the phase of the optical field backscattered by the target.

20. DISTRIBUTION/AVAILABILITY OF ABSTRACT XX UNCLASSIFIED/UNLIMITED ☐ SAME AS RPT. ☐ DTIC USERS	21. ABSTRACT SECURITY CLASSIFICATION Unclassified	
22a. NAME OF RESPONSIBLE INDIVIDUAL Mr. William Martin	22b. TELEPHONE (Include Area Code) (513) 255-6361	22c. OFFICE SYMBOL WRDC/AARI

DD Form 1473, JUN 86   Previous editions are obsolete.
ERIM 116

UNCLASSIFIED
SECURITY CLASSIFICATION OF THIS PAGE

PREFACE

The research reported here was performed in the Optical Science Laboratory of the Advanced Concepts Division, Environmental Research Institute of Michigan (ERIM). The work was sponsored by the Air Force Weapons Laboratory (AFWL) through the Wright Research and Development Center (WRDC) under Contract F33615-83-C-1046. At AFWAL/AARI the Project Monitor was Lt. Robert Fetner and the Program Manager was Mr. William Martin. At AFWL/AROB, the Program Manager was Maj. Paul S. Idell.

This final technical report covers research performed from 1 August 1986 to 7 November 1988, during which time there were three successive associated efforts. (For the sake of readability this report describes all three efforts together, covering topics in a logical rather than chronological order.) The principal investigator at ERIM was James R. Fienup. The other major contributors to this work were Ron S. Goodman and Ann M. Kowalczyk. Additional contributors were Carl C. Aleksoff, Stuart R. DeGraaf, John H. Seldin, and Christopher C. Wackerman.

Accession For

NTIS GRA&I	
DTIC TAB	
Unannounced	
Justification	

By

Distribution/

Availability Codes

| Dist | Avail and/or Special |
| A-1 | |

TABLE OF CONTENTS

v

TABLE OF CONTENTS (Continued)

TABLE OF CONTENTS (Continued)

LIST OF FIGURES

LIST OF FIGURES (Continued)

LIST OF FIGURES (Continued)

LIST OF FIGURES (Continued)

LIST OF TABLES

1.0 INTRODUCTION

To obtain useful images of satellites from the ground, large apertures are needed. According to the laws of diffraction, to obtain a resolution ρ at a range-to-target R with light of wavelength λ, an aperture of diameter about $D = \lambda R/\rho$ is required. At optical or near-infrared wavelengths, we would therefore need an aperture on the order of one meter in diameter for low-altitude earth-orbiting satellite, and an aperture the size of a football field for geosynchronous satellites. Conventional telescopes fail to achieve this for two reasons. First, for the case of high-altitude satellites, the required large apertures are well beyond the current state of the art. Second, for all cases, atmospheric turbulence limits the resolution to an effective aperture diameter of r_o (Fried's parameter), which is typically in the range of 0.05 to 0.20 meters, a small fraction of what is needed. Compensated imaging systems, consisting of wavefront sensors coupled with adaptive optics to correct for atmospheric turbulence in real-time, may work well for the low-altitude case, but that technology does not scale well for the high-altitude case.

This report describes new methods we have developed for reconstructing fine-resolution images of satellites which circumvent both the problems of atmospheric turbulence and obtaining large apertures with today's technology. These methods are also advantageous because they employ the simplest, least expensive receiver possible. Hardware complexity is minimized, however, at the expense of software complexity and computing requirements. This trade-off is increasingly advantageous as computers have been evolving much faster than optics and detectors. We have also developed methods that take data from sensors based on other imaging concepts and reduce the phase errors that are present in the data.

While, in this report, we concentrate on the problem of imaging satellites, the methods described here can also be used for other applications such as SDI discrimination and tactical imaging.

The assumed optical system for the majority of this report is as follows. A pulsed laser of long coherence length illuminates the target object. The intensity of the backscattered radiation is detected by an array of simple light-bucket detectors on the ground, distributed over an area of diameter, D. Alternatively, for the low-altitude case, the radiation can be collected by a telescope, but the detector array is placed in a plane conjugate to (i.e., at an image of) the aperture plane, rather than in the usual focal plane.

Since the phase errors due to atmospheric turbulence are introduced in a volume relatively near to the aperture plane, the detected intensities are, to first order, unaffected by the atmospheric turbulence. (The intensity is affected only to the extent that scintillation, caused by strong upper-atmospheric turbulence, is present.) If the phase associated with the intensities could be retrieved, then by digitally back-propagating the wavefront at the aperture plane to a plane at the target object (essentially a Fourier transform), we could obtain a diffraction-limited image. This image would be complex-valued and would suffer from speckle. Since the realization of the image speckle pattern would change for each laser pulse (as the object rotates slightly or translates), by averaging over the intensities of several such images we can average out the speckles and obtain the equivalent of an incoherent, speckle-free image of the object. The required phases can be computed using one of the phase-retrieval (image reconstruction) algorithms developed under this effort. They require either a glint or glints to be present on the object or to have measured partial information about the phase of the wavefront in the aperture plane.

In a second imaging mode, the multiple realizations of the aperture-plane intensities can be averaged so as to obtain the modulus (magnitude) of the Fourier transform of the incoherent image. Again, by the phase retrieval algorithm, the phase of the Fourier transform can be retrieved, allowing the reconstruction of a diffraction-limited incoherent image. We have called this latter mode "imaging correlography." It has the advantage of working under much broader circumstances (no glints or partial phase are required), but has the disadvantage of requiring a large number of laser pulses to build up a sufficient signal-to-noise ratio.

This report describes the techniques developed for these two novel imaging modes and phase-error correction techniques that can be applied to other imaging sensors. It also describes several associated topics, including the comparison of several competing imaging approaches.

In overview, the imaging approaches we have developed, which utilize phase retrieval algorithms, make possible the reconstruction of fine-resolution images of satellites using hardware technology that is available today. The approaches require only light-bucket detectors which require no phasing and do not have to be very fast. The cost of such a system would be a small fraction of the cost of most competing approaches. Alternatively, improved images can be obtained from other imaging sensors by correction of residual phase errors.

Section 2 of this report contains a brief summary of the research accomplishments. Individual topics are described in detail in Sections 3 to 8. References are found at the end of each section.

2.0 SUMMARY OF ACCOMPLISHMENTS

In this section, we briefly summarize the accomplishments of our research on active imaging. Details are given in the sections that follow.

As described in Section 3, we developed a new imaging modality called imaging correlography. In it, multiple arrays of aperture-plane intensity measurements of laser pulses backscattered by the object are collected. By averaging over the autocovariances of these intensity measurements, we arrive at an estimate of the squared modulus of the Fourier transform of the incoherent object (the object reflectivity function for incoherent illumination). From these data, a fine-resolution nonspeckled image can be reconstructed using the iterative Fourier transform (phase retrieval) algorithm.

The basic theory of imaging correlography was developed. Averaging in both the aperture plane and the Fourier transform of the aperture plane were analyzed. Multiple realizations of complex-valued, laser-illuminated reflectivity functions of a satellite model were computer simulated, and the aperture-plane data were simulated. The averages were computed, and Wiener filtering of the resultant Fourier modulus estimates was performed. Images were reconstructed from these data for various numbers of frames (laser pulses). When a large number of frames were processed, high-quality, fine-resolution images were successfully reconstructed.

The same experiments were repeated for the case of a sparse collecting array consisting of a Golay arrangement of six subapertures. The ability of Wiener filtering to correct for the effects of the MTF of the sparse array and the ability to reconstruct fine-resolution images were demonstrated.

The signal-to-noise ratio (SNR) of the simulated correlography data was measured and compared with theoretical predictions, and it was found that they generally agreed well with one another. The number of frames of data required to achieve a given resolution for a particular image of a satellite model was determined. However, this result depends on the spatial-frequency content of the object. The effect of photon noise for low light levels was analyzed, and it was found that the effects of photon noise are small as long as the number of photons per speckle per frame is much greater than two. Alternative Wiener filters for improving the SNR were derived, and an iterative filtering method was suggested.

As described in Section 4, derivations of the results of noncoherent averaging of images and of the correlography quantities for the case of a mixed object were performed. By a mixed object we mean a coherently illuminated object that has both a fixed, deterministic component (such as a glint or glints) and a random, diffuse component. It was found that if the deterministic component of the object consists of a single glint (a fairly common occurance), then the traditional correlography estimators give an incorrect answer; however, a new estimator, denoted as $<I_1 I_2 - \overline{I}^2 + I^2>$, or $<I_1 I_2 - Var(I)>$, gives the correct answer. This new estimator also gives the correct answer when no glint is present.

As described in Section 5, methods were developed for reconstructing a coherent image from a single frame of aperture-plane intensity data when the object has one or more glints. The most successful method is effective for the most difficult case -- when the object has multiple glints not spatially separated from the diffuse component. It consists of three successive algorithms: (1) an autocorrelation tri-intersection algorithm that determines the glint positions and values; (2) the ΔF-synthesis algorithm that produces a

6

partially-reconstructed image; and (3) the iterative Fourier transform algorithm, which completes the reconstruction of a fine-resolution image. This method was demonstrated to reconstruct fine-resolution images from computer-simulated data. The effect of noise was computer-simulated, and the sensitivity of the method to photon noise and to glint strength was determined by computer reconstruction experiments.

Other coherent reconstruction approaches for the case of objects having glints were also investigated. Reconstructions were successfully performed using only the iterative Fourier transform algorithm for the cases of one and two glints on the object. A recursive reconstruction algorithm based on the autocorrelation of the object (which can be computed from the aperture-plane intensity data) was developed for the case of a single glint on the object. The effects of large glints on the quantization error when detecting the intensity data were analyzed. We found that the quantization error could be greatly reduced by having an automatic gain control that would scale down the detected intensity when a very large glint would appear. A variable zero-offset was found to be useful to a lesser extent.

As described in Sections 6 and 7, methods were developed for reconstructing a coherent image from a single frame of aperture-plane intensity data when partial information about the phase of the optical field is available. These methods are also effective when we have partial phase information for the case of incoherent-image reconstruction as well.

As described in Section 6, a new variation of the iterative Fourier transform algorithm, called the expanding weighted modulus algorithm, was developed. It can be applied when the Fourier phase is known well over a small aperture, but is unknown over the large, full aperture. It involves iterating with progressively larger weighting functions

7

imposed on the Fourier modulus data, reconstructing progressively finer-resolution images, effectively bootstrapping from the phase over the small aperture to the phase over the large aperture. The image-domain constraint used for the iterative transform algorithm is a support (finite extent) constraint.

A second case, reconstruction from one bit of phase known over the entire aperture, was also investigated. When the object is "causal" (i.e., is entirely to one side of the optical axis), then the image can be reconstructed easily by a windowing operation and the iterative transform algorithm.

A third case is where the phase is known poorly over the entire aperture, or, equivalently, a noisy phase exists over the entire aperture. This would be the case if we use any other imaging method that results in phase errors. For this case, another variation of the iterative transform algorithm, called the phase variance algorithm, was developed. In it, the given Fourier modulus, which is assumed to be measured with a higher SNR, is reinforced exactly, but the given Fourier phase is reinforced inexactly; it is allowed to wander from the measured phase in accordance with the standard deviation of the error of the phase. Appropriate data were simulated and reconstruction experiments were performed. For the case of incoherent images (for which one has a nonnegativity constraint), the phase variance algorithm converges faster to the solution than the traditional algorithm. For the case of coherent images, the phase variance algorithm produced images of significantly better quality than that given by the noisy measured phase, but left room for further improvement. Thus, the phase variance algorithm should be used to clean up images produced by other imaging methods. Investigation of the effect of photon noise on the Fourier modulus data was performed by computer simulation and reconstruction experiments. It was shown that if the Fourier modulus

8

data are sufficiently noisy, then the phase variance algorithm no longer improves the image. A further algorithm improvement was suggested: allow both the modulus and phase to vary from their measured values, each in accordance with the variance of the noise on that data. Then in the areas of spatial-frequency space where the modulus is less noisy than the phase, the phase is improved by reinforcing the modulus; and in the areas where the phase is less noisy than the modulus, the modulus is improved by reinforcing the phase.

As described in Section 7, another method of correcting phase errors over the entire aperture was developed. Called 2-D shear averaging, it corrects phase errors using a priori information about the statistics of the coherent object -- that it is delta-correlated -- rather than the usual object-domain support constraint. The algorithm is computationally simple, consisting of three steps. First, phase-error differences in each of the two dimensions are estimated from the summation over a sheared product of the given Fourier transform. The derivation of this result is similar to that of the shearing-interferometer wavefront sensor. Next, the phase error is computed from the phase-error differences by a recrusive method, such as those employed for wavefront sensing or Knox-Thompson image reconstruction. Complex exponentials are employed to avoid phase unwrapping difficulties. Finally, the phase-error estimate is subtracted from the given Fourier phase to yield a corrected Fourier transform. Inverse transformation yields the corrected image. Several versions of the algorithm, differing in the way that the sheared product is averaged, were studied. Analysis was performed to predict the residual phase errors left by this statistically-based algorithm. Data with a variety of phase errors were digitally simulated and image reconstruction experiments were performed. For smooth but higher-order 2-D phase errors the 2-D shear averaging algorithm was shown to improve the image quality substantially, although there was room for further image-

quality improvement. Thus, the 2-D shear averaging algorithm should be used to clean up images produced by other imaging methods when the phase errors are slowly varying.

As described in Section 8, several different classes of imaging systems appropriate for imaging satellites were briefly compared, including both active and passive approaches. Several methods for obtaining fine-resolution images, besides the conventional methods of compensated imaging and microwave synthetic-aperture radar, appear to show promise. One good example of a novel approach is an array of sensors, each consisting of a dual-plane detection of laser radiation plus a wavefront sensor. This approach employs a robust form of phase retrieval to determine the optical field in the aperture plane from two arrays of intensity data without requiring heterodyne detection. The wavefront sensor, operating on incoherent light, determines the wavefront error due to atmospheric turbulence. The phase of the latter is subtracted from the phase of the former to yield the phase due to the object alone.

In summary, several different approaches to reconstructing fine-resolution images of satellites, using relatively simple receivers, were developed. These methods could make possible imaging systems of greatly reduced cost and complexity compared with compensated imaging (using adaptive optics). They tend to scale well for the case of deep-space objects, for which the receiver array must be much larger than any existing optical telescope.

10

3.0 IMAGING CORRELOGRAPHY

In this section, the new imaging method we call imaging correlography is described. It makes use of multiple realizations of the intensity of the coherent optical field, backscattered from the object, measured in the aperture plane, to arrive at an incoherent image of the object. The basic concept is described in Section 3.1. The method is demonstrated for sparse arrays of detectors in Section 3.2. The signal-to-noise ratio achieved in computer simulation is compared with theory in Section 3.3. Wiener filtering issues are further discussed in Section 3.4. Correlography for a "mixed" object, i.e. one having a deterministic (glint) component as well as a diffuse component, is described in Section 3.5, where it is shown that a new estimator is required.

3.1 IMAGING CORRELOGRAPHY THEORY AND RESULTS

It is well known that the spatial structure of a fully developed laser-speckle pattern -- produced by the coherent interference of light backscattered from a sufficiently diffuse, reflecting surface -- is dependent on the macroscopic features of the illuminated surface [3.1]. In this Chapter we demonstrate that measurements of the backscattered speckle intensity are sufficient to (uniquely) reconstruct a high-resolution, unspeckled, incoherent image (or brightness distribution) of the coherently illuminated object.

Our approach to image synthesis is based on the fact that from the average energy spectrum of a laser-speckle intensity pattern we can obtain the autocorrelation function of the illuminated object's brightness distribution [3.2]. Here, the object's brightness distribution corresponds to the object's reflectance function or, alternatively, to its irradiance distribution had the object been

11

illuminated by an incoherent light source. Since the Fourier transform of the autocorrelation of the object brightness function is equivalent to the squared modulus of the Fourier transform of the brightness function [3.3], an image of the object can be obtained if the phase associated with this Fourier transform can be determined. Fortunately, a practical solution to this phase-retrieval problem has been demonstrated by Fienup [3.4-3.6], in which an iterative transform algorithm can be used to recover the phase associated with the modulus of the Fourier transform of a real, nonnegative object function, provided that certain boundedness and nonnegativity constraints are continually reinforced throughout the iteration process. The iterative transform algorithm, together with certain digital preprocessing operations (which are described below) permit us to recover complete, unspeckled images from nonimaged speckle data.

Let us suppose that a diffuse object is flood illuminated with a laser whose coherence length is at least twice as long as the object is deep. An array of photodetectors measures the backscattered light intensity in a far-field plane some distance from the object. We assume that the object is optically rough, so that its microscale surface height variations are random and comparable in size with the wavelength of light. This being the case, the reflected laser light is randomly (and coherently) dephased, and the photodetectors in the observation plane record a fully developed laser-speckle pattern.

Each realization of the observed speckle intensity $I_n(u)$ may be expressed as the squared modulus of the Fourier transform of the complex object field:

$$I_n(u) = |F_n(u)|^2 = |\mathcal{F}\{f_n(x)\}|^2 \; , \qquad (3-1)$$

12

where $\mathcal{F}$ denotes a Fourier transform, $f_n(x) = |f_0(x)|^2 \exp[i\phi_n]^{-1}$ is the field reflected by the object, $|f_0(x)|$ is the object's field amplitude reflectivity, and $\phi_n(x)$ is the (random) phase of the nth realization of the reflected object field associated with the object's surface height profile. In the above expression, x represents a two-dimensional spatial (or angular) coordinate vector in object or image space; u represents a two-dimensional coordinate in the measurement plane. The inverse Fourier transform of the observed speckle pattern is proportional to the autocorrelation of the object field, which may be written as

$$r_n(x) = \mathcal{F}\{|F_n(u)| \, H(u)\}$$

$$= [f_n(x) \circledast f_n(x)] * h(x) , \qquad (3\text{-}2)$$

where $\mathcal{F}^{-1}$ denotes an inverse Fourier transform, $*$ denotes a convolution operation, and $\circledast$ denotes an autocorrelation. The aperture function $H(u)$ denotes the region of the measurement plane over which the speckle pattern is observed: $H(u) = 1$ for points within the measurement aperture, and $H(u) = 0$ elsewhere. The function $h(x) = \mathcal{F}^{-1}\{H(u)\}$ is the (diffraction-limited) coherent impulse response; hence $r_n(x)$ is a diffraction-limited (albeit speckled) autocorrelation of the laser-illuminated object.

Using the iterative transform algorithm, one could attempt to reconstruct a complex-valued, speckled image of $f_n(x)$ from $|F_n(u)|^2 H(u)$ or equivalently from $r_n(x)$. However, at present the practical reconstruction algorithm is effective only for certain classes of complex-valued objects if the object's support is known a priori [3.7] and for even more restrictive classes of complex-valued objects if the object support is unknown. (The support is the closed set of points outside which the object is zero.) Such cases are described in Section

13

4. In this section, we concentrate on a method that allows us to reconstruct a real, nonnegative image -- a case for which the iterative transform algorithm is effective for a broad class of objects.

Image recovery begins by estimating the average energy spectrum of the observed speckle pattern by averaging together the squared moduli of many independent speckled autocorrelations $r_n(x)$. This may be referred to as noncoherent averaging of the coherent autocorrelations. Independent realizations of the speckle pattern can be obtained, for example, by laterally displacing the observation plane with respect to the object or by measuring the speckle pattern for slightly different rotations of the object. We can show that as the number N of independent speckle realizations increases, the computed average energy spectrum converges to [3.8]

$$\lim_{N \to \infty} N^{-1} \sum_{n=1}^{N} |r_n(x)|^2 = b|h(x)|^2 + c r_0(x) * |h(x)|^2 \, , \qquad (3-3)$$

where

$$b = c \left[\int |f_0(x')|^2 \, d^2x' \right]^2 \qquad (3-4)$$

is the square of the total measured irradiance,

$$r_0(x) = |f_0(x)|^2 \circledast |f_0(x)|^2 \qquad (3-5)$$

is the autocorrelation of the object brightness function, and c is a constant. Thus the average energy spectrum converges to the sum of an autocorrelation of the desired incoherent image plus a dc term $b|h(x)|^2$, where the dc term is simply the (incoherent) pointspread function of the collecting aperture, possessing a strength b. On subtracting the dc term from the averaged energy spectrum, we obtain a

diffraction-limited autocorrelation of the incoherent object. The square root of the Fourier transform of this incoherent object autocorrelation, then, provides us with an estimate of the modulus of the Fourier transform of the object's brightness function. Note that one can obtain the same results by subtracting a bias from an average of the autocorrelations of $I_n(u)$ and then taking the square root. One can see that the latter approach is analogous to a highly redundant, multichannel intensity interferometer [3.9]. This latter approach is described in more detail in Section 3.2.

We conducted a series of computer experiments to demonstrate that phase retrieval can be used to recover imagery from speckle data processed in this way. Original object data for these experiments were contained in a digitized photograph of a satellite model illuminated with incoherent light. These data comprised approximately 40 x 60 pixels embedded in a 128 x 128 discrete array. Each realization of a coherent (speckled) image of the object was obtained from the digitized photograph by (1) replacing each pixel with a circular-complex Gaussian random variable whose real and imaginary parts possessed variances equal to half of the pixel intensity value and (2) low-pass filtering the result. The filter used to smooth the complex object data corresponds to the aperture function $H(u)$, which was represented by a 64 x 64 square of detector pixels embedded in 128 x 128 array. Multiple realizations of the coherent object data were obtained by using different random-number seeds in the computation of the complex Gaussian random variables. Each coherent image autocorrelation $r_n(x)$ was computed by inverse Fourier transforming the squared modulus of the apertured Fourier transform of the simulated coherent image. Averages of both the speckled autocorrelations and their squared moduli (i.e., the energy spectrum of the speckle-intensity patterns) were then taken. A function proportional to the square of the former, an estimate of the dc term, was subtracted from the latter (the noncoherent average) to arrive at an estimate for the autocorrelation of the incoherent image.

The process of noncoherently averaging object-field autocorrelations and subtracting the dc term is illustrated in Fig. 3-1. The first column contains averages of the squared inverse Fourier transforms of N simulated speckle measurements providing estimates of the speckle energy spectrum, where N is the number of independent speckled autocorrelations noncoherently averaged. The second column shows the corresponding dc term, which, for the case of a square aperture, is a squared $sinc(x)$ [i.e., $(\pi x)^{-1} \sin(\pi x)$] function. The third column shows the results when the dc term is subtracted from the noncoherently averaged autocorrelations of the first column. Note that the speckle artifacts in the averaged autocorrelations (in the first and third columns of Fig. 3-1) disappear as N increases.

The incoherent autocorrelation estimate (with the dc term removed) was then Fourier transformed, and the square root was taken, to arrive at an estimate of the modulus of the Fourier transform of the object brightness function. Negative numbers, resulting from noise associated with the finite-average approximation to an ensemble average, were set to zero before the square root was taken. Images were reconstructed from the Fourier modulus estimates by using the iterative Fourier-transform algorithm [3.5, 3.6], using several cycles of the hybrid input-output algorithm (using $\beta = 0.7$) and the error reduction algorithm until the algorithm appeared to stagnate. The object-domain constraints used were nonnegativity (since an incoherent image is being reconstructed) and a loose support constraint (a rectangle half the size of the smallest rectangle enclosing the autocorrelation).

Data along the first row of Fig. 3-2 illustrate a direct application of the phase-retrieval algorithm to the Fourier modulus estimate. Figure 3-2(A) represents the dc-subtracted autocorrelation for $N = 10^4$ independent speckle patterns. Figure 3-2(B) shows the corresponding Fourier modulus data produced by Fourier transforming the
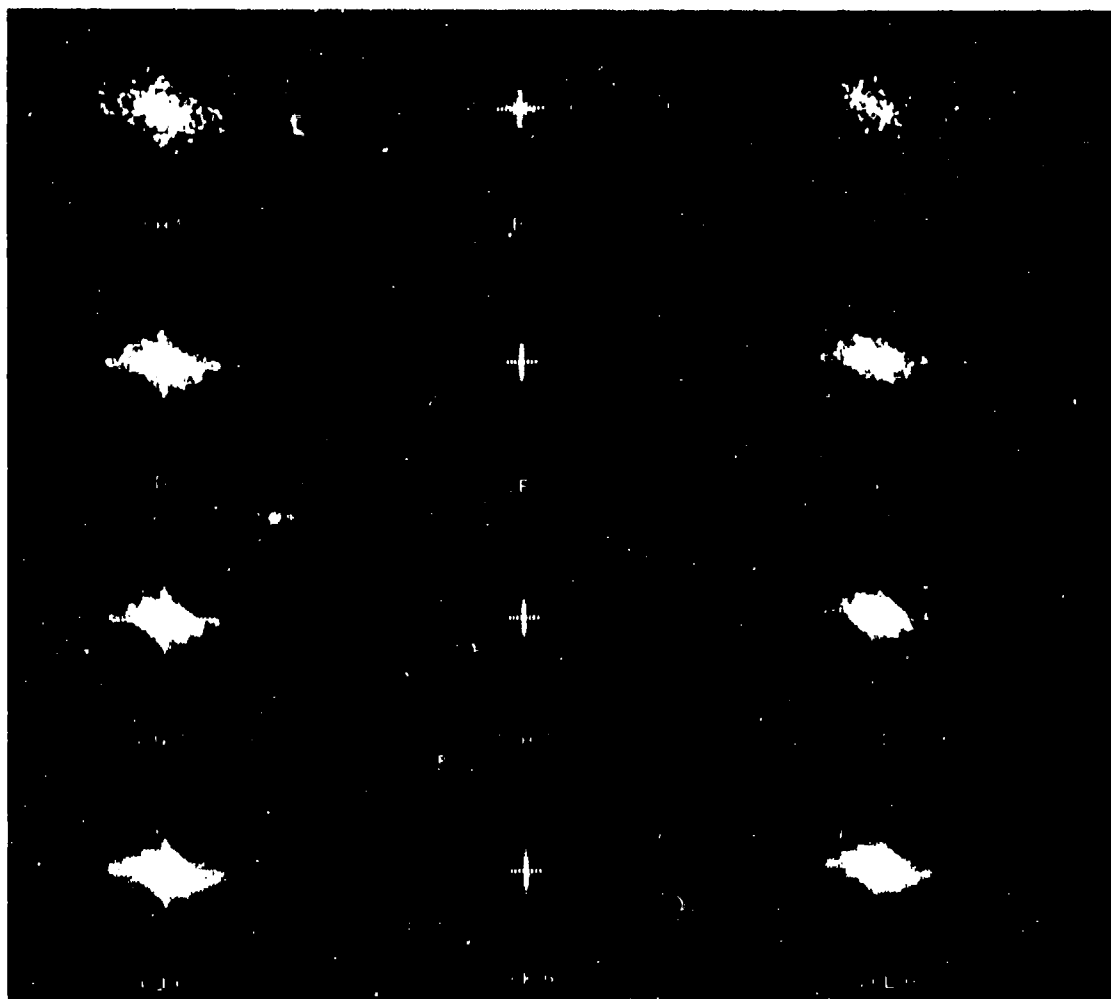
FIGURE 3-1. ESTIMATING THE ENERGY SPECTRUM OF SPECKLE INTENSITY BY NONCOHERENTLY AVERAGING MANY COHERENT SPECKLED IMAGE AUTOCORRELATIONS. (A) Noncoherent average of N = 4 autocorrelations; (B) estimate of dc term; (C), (A) minus (B); (D)-(F) N = 32; (G)-(I) N = 128; (J)-(L) N = 1024.

FIGURE 3-2. IMAGE RECOVERY FROM NONCOHERENTLY AVERAGE AUTOCORRELATION DATA (N = 10,000, FILLED APERTURE). (A) DC-adjusted, noncoherently averaged autocorrelations, (B) estimate of the Fourier modulus of the incoherent object, (C) image reconstructed from (B) using the iterative transform (phase-retrieval) algorithm, (D) Wiener filter, (E) filtered Fourier modulus estimate, (F) image reconstructed from (E), (G) original incoherent object, (H) Wiener filtered, incoherent object, (I) result of Wiener filtering (C).

averaged autocorrelation [Fig. 3-2(A)] and then taking the square root. Figure 3-2(C) is the reconstructed image produced by applying the phase-retrieval algorithm as outlined above. Note that this image is very noisy compared with the original incoherent object, shown in Fig. 3-2(G). Noise in the reconstructed image is due to the fact that a finite number of speckle realizations were used to estimate the Fourier modulus. To reduce these noise effects, we multiplied the Fourier modulus estimate [Fig. 3-2(B)] by a Wiener filter of the form

$$W(\Delta u) = \frac{OTF(\Delta u) \; E_s(\Delta u)}{|OTF(\Delta)|^2 \; E_s(\Delta u) + E_n} \; , \qquad (3-6)$$

where $OTF(\Delta u) = H(u) \circledast H(u)$ is the optical transfer function of the receiver aperture, $E_s(\Delta u)$ is an average energy spectrum for objects of this type (estimated by taking an angular average over the squared Fourier modulus of the object), and E_n is the energy spectrum of the noise. We approximated E_n by a constant whose value was obtained by averaging the squared Fourier modulus estimate over those higher spatial frequencies where the signal-to-noise ratio was less than one. Figure 3-2(D) shows the Wiener filter used for this example.

Figure 3-2(E) shows the filtered Fourier modulus estimate equal to the product of Figs. 2(B) and 2(D). Figure 3-2(F) shows the image reconstructed from the Wiener-filtered Fourier modulus estimate using the phase-retrieval algorithm. Note that the Wiener filter has significantly improved the quality of the reconstructed image in Fig. 3-2(F) over that in Fig. 3-2(C) reconstructed without Wiener filtering. For comparison, the original object [shown in Fig. 3-2(G)] was passed through the Wiener filter of Fig. 3-2(D), with the result shown in Fig. 3-2(H). The image reconstructed from speckle-correlation measurements, shown in Fig. 3-2(F), compares favorably with the filtered object [Fig. 3-2(H)], indicating good performance on the part of the iterative

19

transform reconstruction algorithm. Finally, Fig. 3-2(I) shows the result of applying the Wiener filter to the reconstructed image shown in Fig. 3-2(C). Apparently, Wiener filtering followed by image reconstruction is superior to image reconstruction followed by Wiener filtering.

These results demonstrate the possibility of recovering images from nonimaged laser speckle patterns: by averaging over many realizations of the coherent (speckle) intensity data, an estimate of the autocorrelation and Fourier modulus of the incoherent object can be obtained. And, from the Fourier modulus estimate, it is possible to reconstruct an unspeckled image by applying a phase-retrieval algorithm with a nonnegativity constraint.

Figures 3-3 and 3-4 show results similar to those in Fig. 3-2, but for a smaller number of realizations, N, of the speckle patterns. Figure 3-3 shows the case for N = 1024 realizations and Figure 3-4 the case of N = 128 realizations. As expected, the image quality decreases with fewer number of speckle frames due to the statistical noise associated with a finite number of frames. Section 3-3 will discuss in greater detail the signal-to-noise issues.

Since these computer simulations were performed, laboratory experimental verification of imaging correlography has also been accomplished [3.10].

This section is an expansion of Reference 3.11.

FIGURE 3-3. IMAGE RECOVERY FROM NONCOHERENTLY AVERAGE AUTOCORRELATION
DATA (N = 1024, FILLED APERTURE). (A) DC-adjusted, noncoherently
averaged autocorrelations, (B) estimate of the Fourier modulus of the
incoherent object, (C) image reconstructed from (B) using the iterative
transform (phase-retrieval) algorithm, (D) Wiener filter, (E) filtered
Fourier modulus estimate, (F) image reconstructed from (E), (G)
original incoherent object, (H) Wiener filtered, incoherent object, (I)
result of Wiener filtering (C).
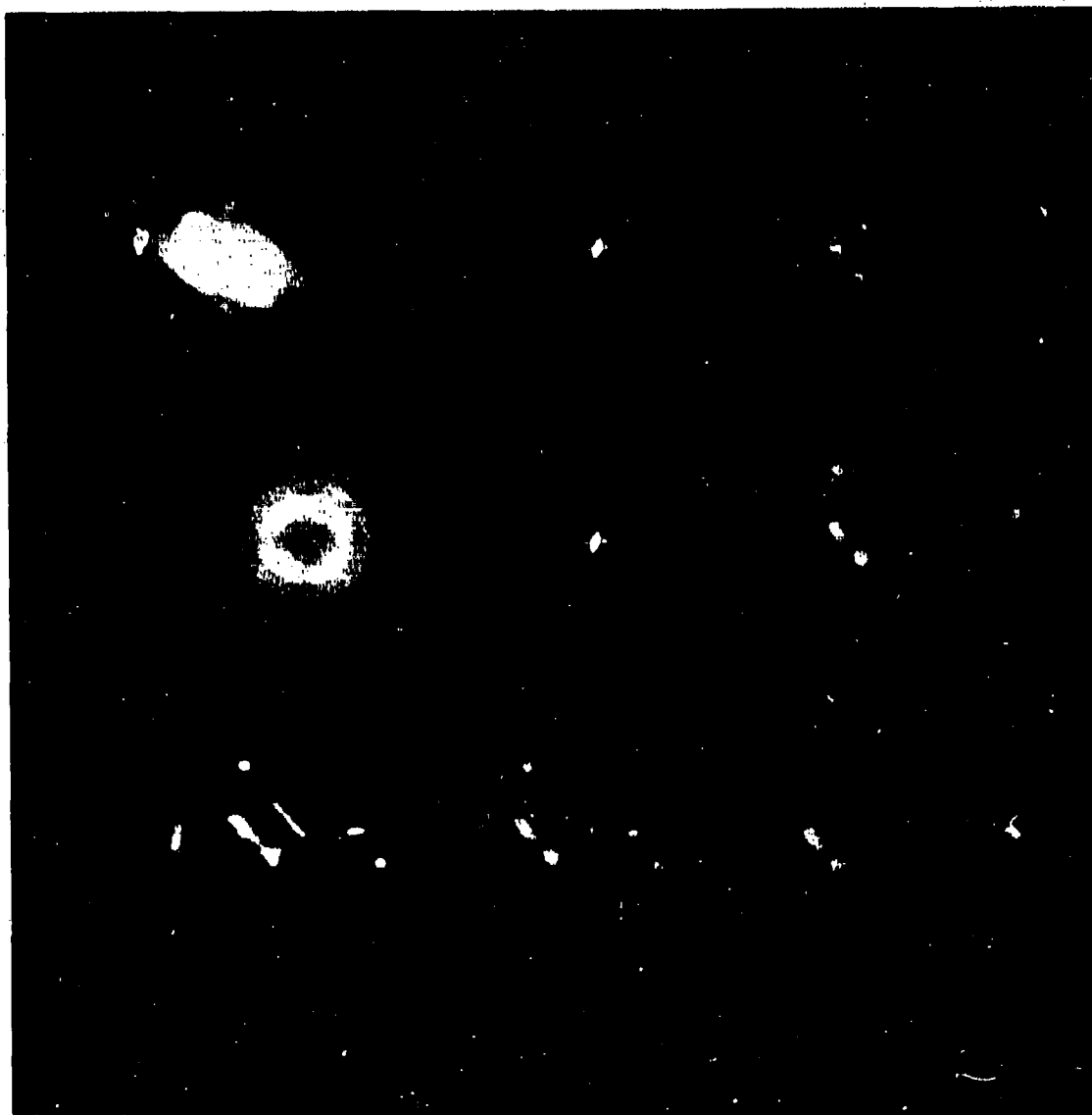
FIGURE 3-4. IMAGE RECOVERY FROM NONCOHERENTLY AVERAGE AUTOCORRELATION DATA (N = 128, FILLED APERTURE). (A) DC-adjusted, noncoherently averaged autocorrelations, (B) estimate of the Fourier modulus of the incoherent object, (C) Wiener filter, (D) filtered Fourier modulus estimate, (E) image reconstructed from (D), (F) original incoherent object, (G) Wiener filtered, incoherent object.

3.2 IMAGING CORRELOGRAPHY WITH SPARSE ARRAYS OF DETECTORS

In this section the use of imaging correlography, introduced in the previous section, with sparse arrays of detectors is discussed and demonstrated through digital simulations. In this case it is important to emphasize the relationship between the aperture function shape and the modulation transfer function (MTF) for the image. For this reason we start with an alternative (but mathematically equivalent) explanation of the correlography process.

Rather than relating, as we have done above in Eq. (3-3), the average energy spectrum of the speckle pattern to the autocorrelation function of the object's brightness function, we can equate the autocovariance of the far-field laser speckle pattern with the energy spectrum of the object's brightness function. This second interpretation suggests the following procedure for image recovery: (1) estimate the autocovariance of the observed speckle intensity, (2) take the square root of the estimated autocovariance, (3) recover the phase associated with this square-root, and finally (4) inverse Fourier transform the assembled Fourier data. Image recovery using this prescription uncovers a close relationship between imaging correlography and image recovery from intensity interferometry [3.13], where the object's Fourier phase information, too, is lost to the measurement process. (The fact that Fourier domain information of incoherent objects can be obtained from far-field correlations is, of course, a consequence of the Van Cittert-Zernike theorem [3.12].)

We can demonstrate the relationship between the autocovariance of the laser speckle pattern and the object energy spectrum by considering the measurement process involved in imaging correlography. Let us suppose that a diffuse object is flood illuminated with a laser so that the object lies entirely within the coherence volume of the laser beam.

23

A two-dimensional array of photodetectors measures the backscattered light intensity in a (far-field) plane some distance z from the object (see Fig. 3-5 for a possible measurement scenario). We assume that the object is optically rough so that its microscale surface height variations are random and of size comparable to or greater than the wavelength of light. Additionally, we assume that the transverse scale size of the surface height fluctuations is small compared to the resolution patch size associated with the collecting array (i.e., the spatial correlation of surface roughness is small compared to $\lambda z/D$, where λ is the wavelength of light, z is the range, and D is the largest array dimension). This being the case, the reflected laser light is randomly (and coherently) dephased and the photodetectors in the observation plane record the intensity pattern of a fully developed laser speckle pattern [3.1].

An estimate of the autocovariance of the measured speckle pattern, I_n [see Eq. 3-1], may be computed as follows from N realizations of the laser speckle intensity:

$$\hat{C}_I(\Delta u; N) = \frac{1}{N} \sum_{n=1}^{N} \int\int_{-\infty}^{\infty} H(u + \Delta u) \, H(u) \left[I_n(u + \Delta u) \, I_n(u) - \overline{I}^2 \right] d^2u$$

$$= \int\int_{-\infty}^{\infty} H(u + \Delta u) \, H(u) \left\{ \frac{1}{N} \sum_{n=1}^{N} \left[I_n(u + \Delta u) \, I_n(u) - \overline{I}^2 \right] \right\} d^2u \quad (3\text{-}7)$$

where $\overline{I}$ is the average intensity of the observed speckle pattern, Δu is a vector separation in the measurement plane, and $H(u)$ is the pupil (aperture) function associated with the collecting array, defined as

$$H(u) = \begin{cases} 1, & \text{for } u \in \text{aperture array} \\ 0, & \text{otherwise} \end{cases} \quad (3\text{-}8)$$

COHERENT ILLUMINATOR

LASER

OBJECT

Y

X

U_y

U_x

UNFILLED
RECEIVER
ARRAY
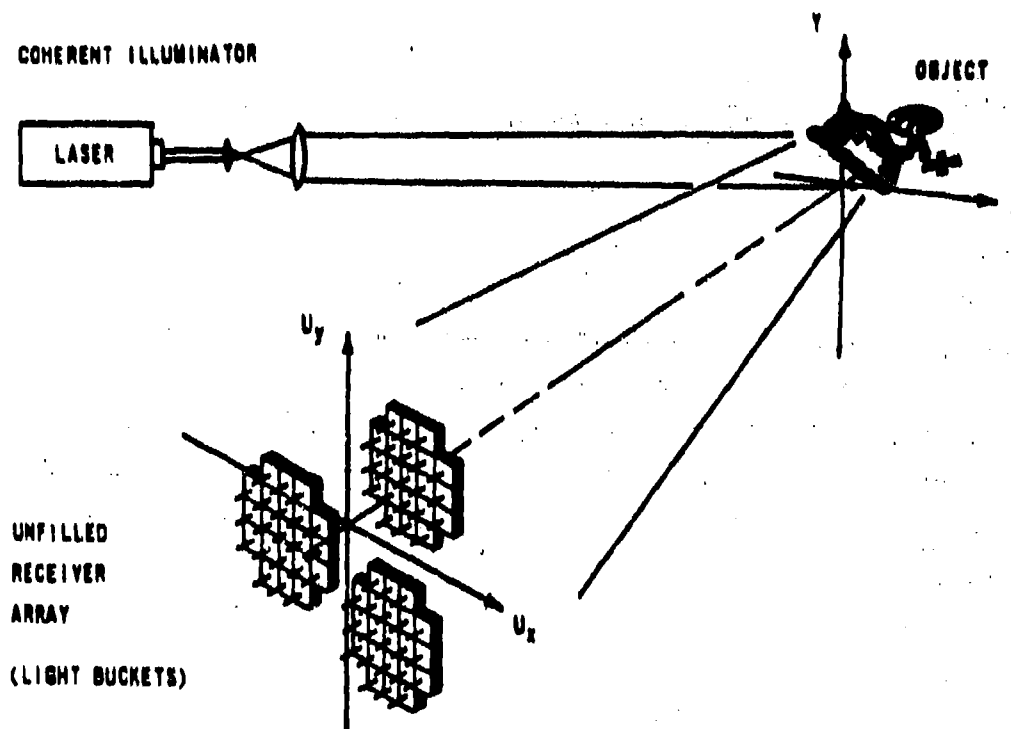
(LIGHT BUCKETS)

FIGURE 3-5. SENSING GEOMETRY FOR A SPARSE-ARRAY IMPLEMENTATION OF IMAGING CORRELOGRAPHY. Light from the laser is expanded to flood illuminate the target object. The backscattered laser speckle intensity is measured with light bucket detectors arranged in an unfilled, two-dimensional array configuration.

In the limit as N (the number of independent observed speckle patterns) approaches infinity, one can use the moment factoring theorem for circular-complex Gaussian (ccg) fields [3.13] to show that

$$\lim_{N \to \infty} \frac{1}{N} \sum_{n=1}^{N} \left[I_n(u + \Delta u) \, I_n(u) - \overline{I}^2 \right] = |\Gamma(\Delta u)|^2 \qquad (3-9)$$

where $\Gamma(\Delta u) = \mathcal{F}[|f_o(x)|^2]$ is the Fourier transform of the object's brightness distribution [i.e., $\Gamma(\Delta u)$ is the mutual intensity of the (complex) speckle field in the measurement aperture, evaluated at field points separated by a vector Δu]. Our ability to invoke the ccg moment theorem above follows from the fact that the observed speckle field is ccg, since the speckle pattern is fully developed. In the limit $N \to \infty$, we therefore find from Eqs. (3-7) and (3-9) that the estimated autocovariance of the speckle intensity observed over the measurement aperture H(u) is given by

$$C_I(\Delta u) = \lim_{N \to \infty} \hat{C}_I(\Delta u; N)$$

$$= OTF(\Delta u) \, |\Gamma(\Delta u)|^2 \qquad (3-10)$$

where OTF(u) is the autocorrelation of H(u). This result demonstrates that $\hat{C}_I(\Delta u; N)$ provides an estimate for $|\Gamma(\Delta u)|^2$, the energy spectrum of the object's brightness function -- the square root of which is an estimate of the Fourier modulus of the object's brightness function. This square root is used in the iterative transform algorithm to retrieve the associated Fourier phase data and thereby reconstruct an image.

We see from Eq. (3-10) that the estimated autocovariance of the observed speckle pattern provides a weighted, or filtered, estimate of the object's energy spectrum. This weighting is completely determined by the spatial arrangement of the detectors making up the collecting aperture. Because this weighting function OTF(Δu) is equal to the autocorrelation of the measurement pupil, we refer to OTF(Δu) as the optical transfer function (OTF) for the imaging correlography system -- with obvious analogy to the OTF arising in the analysis of incoherent imaging systems. The modulation transfer function (MTF), is just the modulus of the OTF; and since the OTF is nonnegative, MTF(Δu) = OTF(Δu). The fact that this OTF is in the form of an autocorrelation allows us to consider the use of sparse arrays of intensity detectors in imaging correlography.

The fact that the OTF for imaging correlography is given by the autocorrelation of the pupil function H(u) suggests a procedure with which to remove sidelobe artifacts introduced by a multiple-aperture (sparse array) measurement scheme. If the detector elements are positioned so that the autocorrelation of the detector array does not drop to zero within the bandpass of the OTF, the object energy spectrum estimated by the imaging correlography process contains essentially the same spatial frequencies as a filled aperture having the same diameter as the sparse array. And, provided that the noise in the estimated autocovariance is not too great, the energy spectrum estimate can be boosted to match the OTF of a completely filled aperture; an image with nearly the resolution of the full aperture is then, in theory, synthesized.

In practical applications of imaging correlography, noise in the Fourier modulus estimate will arise from many sources including detector noise, background flux noise, photon shot noise, and noise that is introduced when a finite number of speckle measurements is used

to estimate the speckle autocovariance. Where all the noise sources additive and uncorrelated with the signal component, one would logically implement the MTF boosting procedure by applying a Wiener-Helstrom filter [3.14] to the Fourier modulus estimate so that the mean-square error between the estimated image and the true (full-resolution) image is minimized. Even if the signal and noise sources do not exactly satisfy these conditions, a Wiener-Helstrom filter is still very advantageous to use [3.14].

For conventional incoherent imaging systems the Wiener-Helstrom filter is of the form

$$W(\Delta u) = \frac{OTF(\Delta u) \; |\Gamma(\Delta u)|^2}{|OTF(\Delta u)|^2 \; |\Gamma(\Delta u)|^2 + E_n(\Delta u)} \qquad (3\text{-}11)$$

where $|\Gamma(\Delta u)|^2$ is the energy spectrum of the object's brightness function, equal to $E_s(\Delta u)$ used in Eq. (3-6), $OTF(\Delta u)$ is the OTF of the collecting aperture, and $E_n(\Delta u)$ is the energy spectrum of the image-domain noise. This filter is based on a model of the imaging process which is given in the Fourier domain as $OTF(\Delta u) \; \Gamma(\Delta u) + $ Noise. However, a better model for imaging correlography is

$$\hat{C}_I(\Delta u; N) = OTF(\Delta u) \; |\Gamma(\Delta u)|^2 + N_c(\Delta u) \quad , \qquad (3\text{-}12)$$

where $N_c(\Delta u)$ is additive noise, for which the appropriate filtering operation to estimate the object's energy spectrum is

$$|\hat{\Gamma}(\Delta u)|^2 = W_c(\Delta u) \; \hat{C}_I(\Delta u; N) \qquad (3\text{-}13)$$

where the filter is given by

$$W_c(\Delta u) = \frac{OTF(\Delta u) \; |\Gamma(\Delta u)|^4}{|OTF(\Delta u)|^2 \; |\Gamma(\Delta u)|^4 + E_c(\Delta u)} \qquad (3-14)$$

where $E_c(\Delta u)$ is the variance of $N_c(\Delta u)$.

Whether taking the square root of the speckle autocovariance then filtering with Eq. (3-11) or filtering the speckle autocovariance with Eq. (3-14), then taking the square root, in either case the MTF is boosted where the signal-to-noise ratio is high and it is depressed where the signal-to-noise ratio is low, thereby resulting in a better Fourier modulus estimate. Indeed, results of the computer simulations presented in the next section demonstrate that such filtering techniques improve the overall quality of imagery recovered in imaging correlography.

We conducted a series of computer experiments to demonstrate that phase retrieval can be used to recover imagery from far-field speckle intensity data collected over a sparse array. The procedure followed here is essentially the same as that reported in Section 3.1, with the exception that here the speckle realizations used to compute an estimate of the incoherent object's energy spectrum are masked with a pupil function H(u) emulating a sparse collecting array.

The original object data for these experiments was the same as described in Section 3.1. For these sparse aperture simulations, we used a Golay-type array [3.15] comprising six subapertures. Figure 3-6 shows the Golay aperture configurations used for this study together with the corresponding OTF's and point-spread functions. The narrower- and wider-segment Golay arrays were both configured to have a 16 pixel separation between adjacent subapertures; the diameters of the
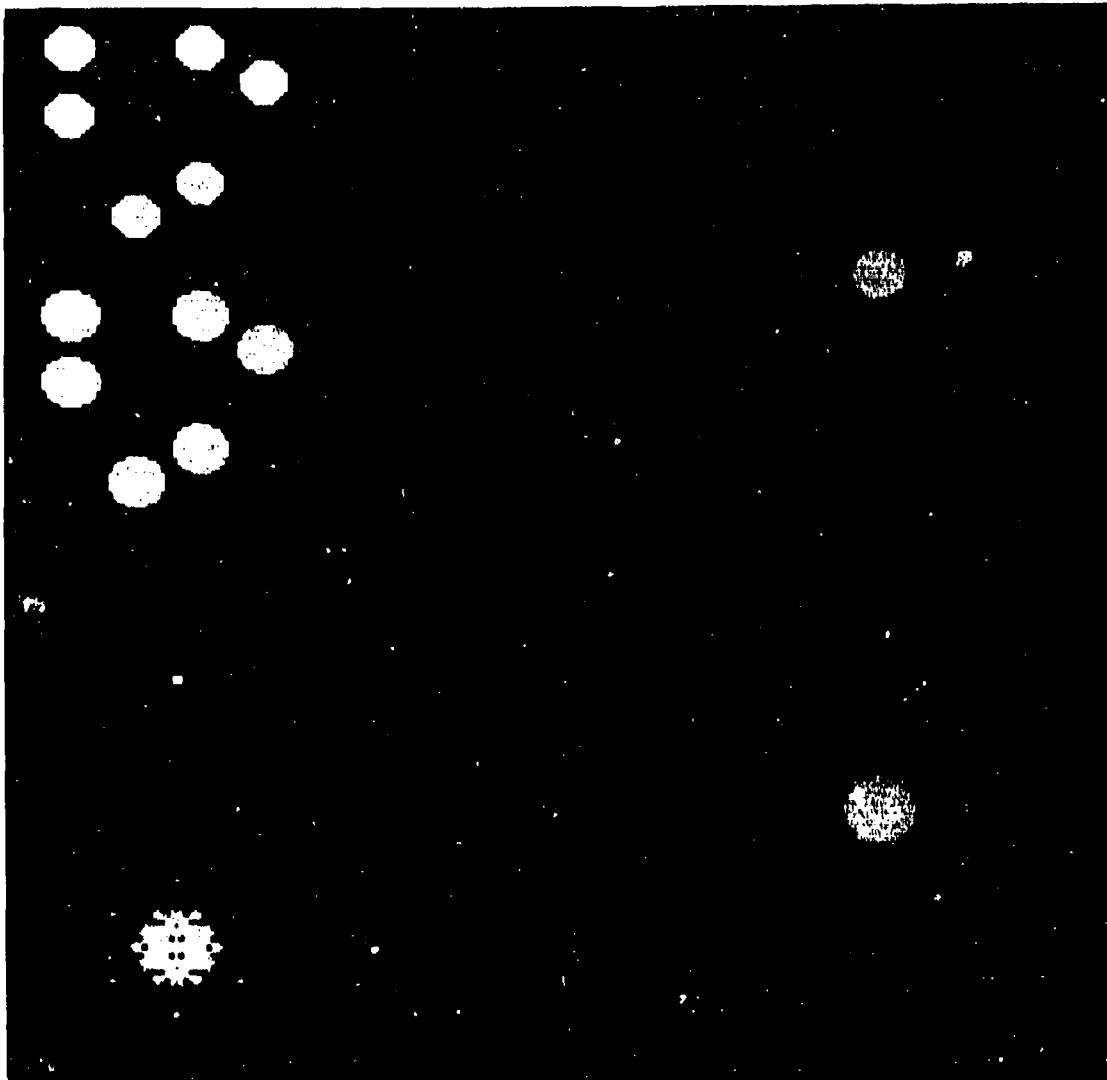
FIGURE 3-6. GOLAY CONFIGURATIONS CONTAINING SIX SUBAPERTURES. Upper left: Aperture functions H(u) for the Golay-6. Right: OTF's corresponding to the Golay-6 aperture functions shown in the upper left. Lower left: Point-spread function associated with the wider-segment Golay-6 aperture.

individual subapertures in the narrower- and wider-segment arrays were 11 and 13 pixels, respectively. In both the cases the OTF, which is the autocorrelation of the pupil function, consists of a large central peak surrounded by 30 satellite peaks. Although the widths of the subapertures for both cases were chosen to be large enough that the OTF does not drop to zero within the bandpass, the narrower-segment array OTF does drop to low values in the regions between the satellite OTF peaks. In the presence of noise, these dips in the OTF could result in information loss at these spatial frequencies. For the wider-segment case, the OTF stays above half of the value of the satellite peaks in the areas between the satellite peaks, as can be seen in Figure 3-7. For this reason the wider-segment Golay array was chosen for the simulation. To perform the filtering operation on the complex object data, the sampled Golay arrays were embedded in a 128 x 128 array. Multiple realizations of the coherent object data are then obtained by using different random number seeds in the computation of the complex Gaussian random variables.

An estimate of the object energy spectrum was formed by processing multiple arrays of pupil-plane speckle intensity data computed from realizations of the filtered coherent object. Several different estimators of the object energy spectrum can be used, such as the one given by Eq. (3-7). Figure 3-8 shows an example of the data that was computed for these experiments, first the average energy spectrum of the speckle intensity was computed by inverse Fourier transforming the square modulus (i.e., the speckle intensity) of the Golay-apertured Fourier transform for each simulated coherent image, and then these speckled energy spectra were averaged together as shown in Figure 3-8(A). After a large number N of independent coherent speckle data sets were processed in this fashion, a DC term (in fact a function, corresponding to a scaled version of the squared modulus of an average of the Fourier transforms of the windowed, speckle intensity arrays
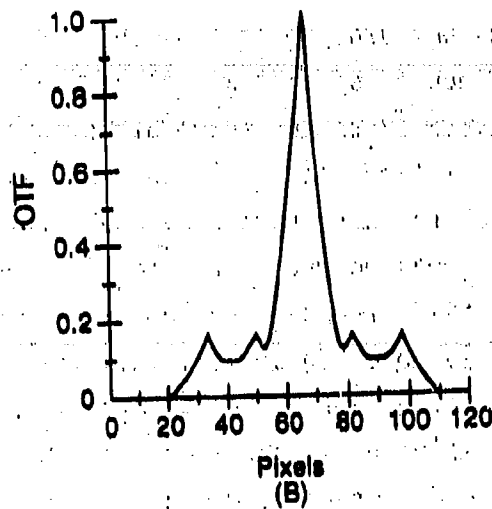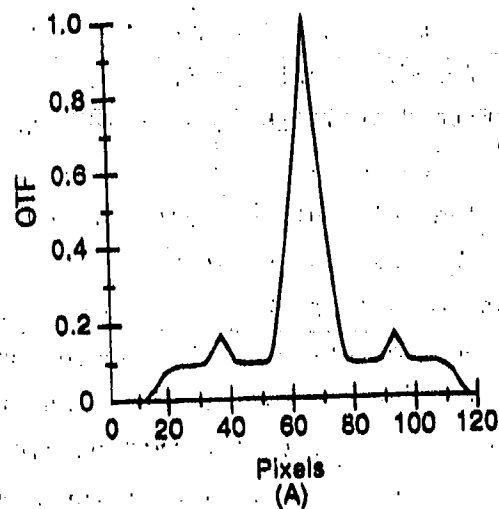
FIGURE 3-7. CROSS SECTIONS OF THE WIDER-SEGMENT GOLAY-6 APERTURE. (A) Horizontal cut through origin of OTF pictured in Figure 3-6; (B) vertical cut through origin.
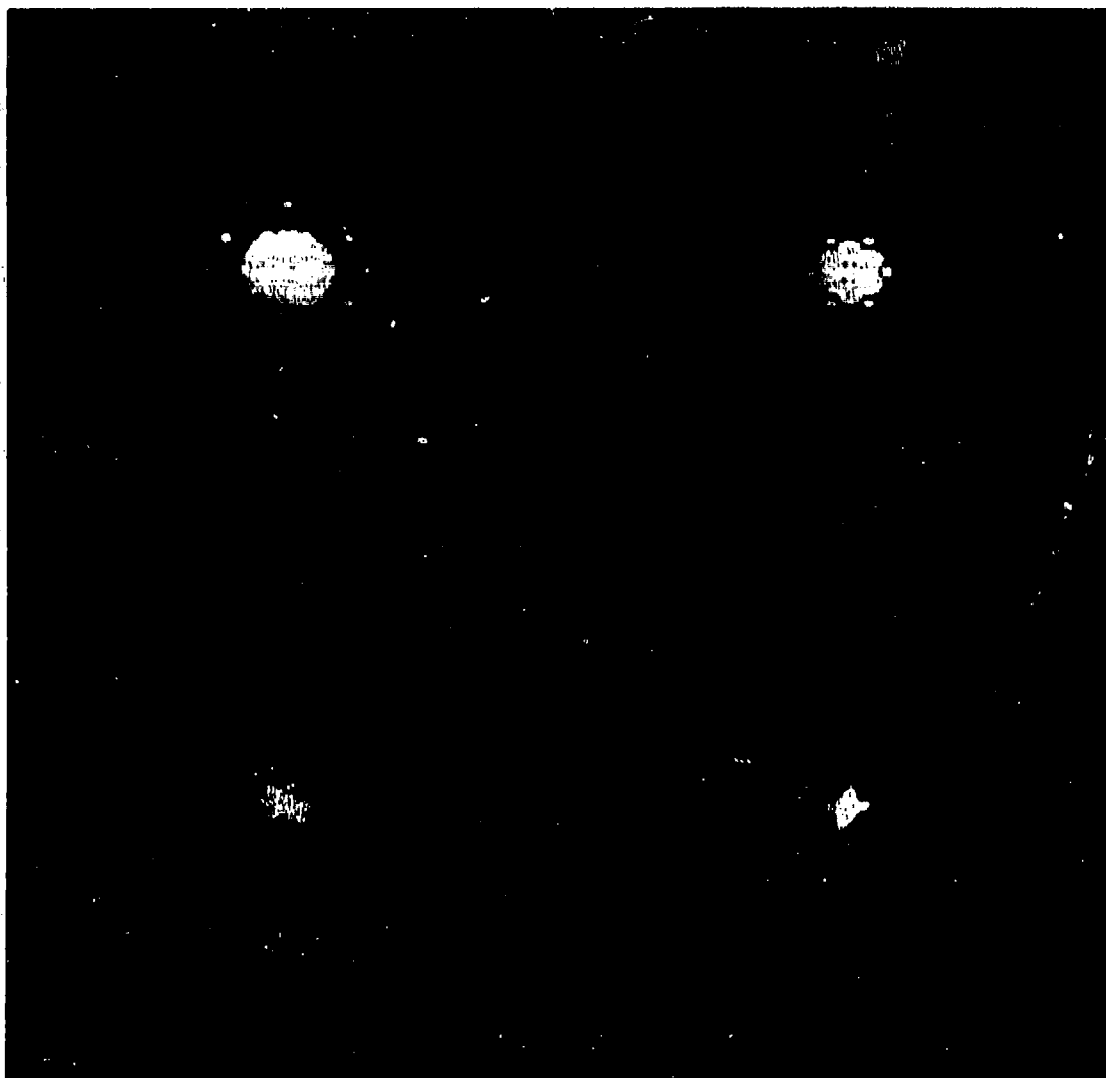
FIGURE 3-8. ESTIMATING THE ENERGY SPECTRUM OF SPECKLE INTENSITY FOR
THE GOLAY-6 APERTURE. (A) Noncoherent average of 1024 autocorrela-
tions; (B) an estimate of the dc-term; (C) (A) minus (B); (D) the
corresponding estimate of the Fourier modulus (the square root of the
estimated autocovariance).

33

observed over the measurement aperture) was computed, as shown in Figure 3-8(B). This DC term was subtracted, with the result shown in Figure 3-8(C). This result was Fourier transformed, providing an estimate of the autocovariance of the observed speckle pattern, which by Eq. (3-10), is an OTF-weighted estimate of the incoherent object's energy spectrum. This is shown in Figure 3-8(D).

Results of image reconstruction experiments applying phase retrieval to the estimate of the object's energy spectrum are shown in Figure 3-9. Figure 3-9(A) shows the averaged energy spectrum (with the DC term removed) of the pupil-plane speckle intensity for the wider-segment Golay-6 array shown in Figure 3-6, for which N = 10,240 independent realizations of speckle intensity were averaged. Figure 3-9(B) is an estimate of the Fourier modulus of the object's brightness distribution computed by taking the square root of the Fourier transform of Figure 3-9(A). Negative numbers, resulting from noise associated with the finite-average approximation to an ensemble average, were set to zero prior to taking the square root. Figure 3-9(C) is the image produced by applying the iterative transform phase-retrieval algorithm [3.6-3.6] to the Fourier modulus data contained in Figure 3-4(B). The procedure for accomplishing phase retrieval involved applying several cycles of the hybrid input-output algorithm (using beta = 0.7) and the error reduction algorithm until the algorithm appeared to stagnate. The object-domain constraints used were non-negativity (since an unspeckled, or incoherent, image is being reconstructed) and a loose support constraint, a rectangle half the size of the smallest rectangle enclosing the average energy spectrum of the observed speckle pattern. The object is guaranteed to fit within this support constraint [3.16].

34

FIGURE 3-9. IMAGE RECOVERY USING THE GOLAY-6 APERTURE, N = 10,240. (A) Average energy spectrum of the measured speckle patterns (with dc-term removed); (B) estimate of the Fourier modulus of the object brightness distribution; (C) image reconstructed from (B) using the iterative transform (phase retrieval) algorithm; (D) Wiener-like filter for the Golay-6 aperture; (E) filtered Fourier modulus estimate; (F) image reconstructed from (E); (G) original incoherent object; (H) filtered, incoherent object; (I) results of filtering (C).

Note that the recovered image shown in Fig. 3-9(C) is very noisy compared with the original incoherent object, shown in Fig. 3-9(G), although a general resemblance of the object has been recovered. Noise in this reconstructed image is due to the fact that a finite (albeit large) number of speckle realizations were used to estimate the Fourier modulus. To reduce these noise effects, we multiplied the Fourier modulus estimate shown in Fig. 3-9(B) by the Wiener-like filter of Eq. (3-11). For these simulations, the energy spectrum of the object was taken to be an angular (spin) average over the squared Fourier modulus of the true object. The noise spectrum was approximated by a constant, whose value was obtained by averaging the squared Fourier modulus estimate over those higher spatial frequencies where the signal-to-noise ratio was less than one. Figure 3-9(D) shows the resulting Wiener filter used for this example. Figure 3-9(E) shows the product of the filter 3-4(D) with the original Fourier modulus estimate 3-9(B).

Figure 3-9(F) shows the image reconstructed from the filtered Fourier modulus estimate 3-9(E) using the phase retrieval algorithm. Note that the filter has significantly improved the quality of the reconstructed image 3-9(F) over that in 3-9(C) reconstructed without filtering. For the purposes of comparison, the original object 3-9(G) was passed through the filter 3-9(D), with the result shown in 3-9(H). The image reconstructed from speckle correlation measurements, shown in Fig. 3-9(F), compares favorably with the filtered object 3-9(H), indicating good performance on the part of the iterative transform algorithm. Figure 3-9(I) shows the result of applying the Wiener filter to the reconstructed image shown in Fig. 3-9(C). It appears, at least for this example, that filtering followed by image reconstruction is somewhat superior to image reconstruction followed by filtering. We might expect to get even better results by using an improved Wiener filter, for example, by using a better estimate of the object power spectrum or by using Eqs. (3-13) and (3-14).

36

One way to evaluate the MTF-boosting properties of the filter of Eq. (3-11) is by inspection of the filter, which is shown in Figure 3-9(D). Notice that it has a local minimum in the center (at zero spatial frequency) and a ring of local maxima at a higher spatial frequency. This compensates, in part, for the rapid drop-off of the OTF that can be seen in Figure 3-7. The ratio of the peak value of the filter to the zero-frequency value is 3.38, a sizable boosting of the OTF at that spatial frequency. This falls short of a complete compensation due to the noise energy spectrum term in Eq. (3-11). For the same reason, the filter drops off for the highest spatial frequencies, where the noise dominates the signal.

Another way to evaluate the MTF-boosting properties of the filter of Eq. (3-11) is to compare the imaging results shown in Figure 3-9 with those obtained with a filled collecting aperture. Figure 3-2 in Section 3.1 shows the results of image recovery from simulations of imaging correlography obtained with a full aperture, where the simulated speckle intensity data were filtered by a square aperture comprising 64 x 64 "detector" pixels fully encompassing the sparse Golay aperture used above. (The width of the Golay array is only 55 pixels.) Except for the form of filtering used to mask the speckle measurement data, the digital processing steps used to produce each frame of Figure 3-2 is identical to that of the corresponding frame of Figure 3-9. The top row of frames of Figure 3-2 correspond to image retrieval with a full aperture, but without Wiener filtering. Note that the resulting image 3-2(C) is noisy, but is significantly better than its sparse array counterpart 3-9(C). The filter shown in 3-2(D) is that prescribed by Eq. (3-11) with the OTF given by the auto-correlation of the filled, square aperture. Figure 3-2(F) shows the image recovered from the Wiener-filtered Fourier modulus 3-2(E) for the filled aperture. Comparing Figures 3-2(F) and 3-9(F) indicates that most of the key features of the object recovered in the filled-aperture

case were also recovered with the sparse, Golay-6 aperture case. However, some of the finer details of the object recovered in the full aperture case were smoothed over in the Golay aperture reconstruction. This loss of resolution for the sparse-aperture case is the result of a smaller OTF(Δu) value (i.e., a lower redundancy), and hence a lower signal-to-noise ratio, for larger spatial frequencies.

The results of this section demonstrate the possibility of recovering images from nonimaged (far-field) laser speckle patterns observed with sparse arrays of intensity detectors. The images obtained using a combination of a Wiener-filtered speckle autocovariance together with the iterative transform phase retrieval algorithm show marked improvement over those obtained without filtering. The fact that the image in Fig. 3-9(F), constructed with sparse arrays of detectors, approaches the quality of the full-aperture image shown in Figure 3-2(F) suggests that the MTF boosting filtering is successful in removing image artifacts due to the sparse collecting aperture.

Figure 3-10 shows similar results for the sparse aperture, but with only N = 1024 realizations averaged. As in the filled-aperture case, the loss in resolution due to a lower signal-to-noise ratio is evident.

3.3 SIGNAL-TO-NOISE RATIO AND RESOLUTION

Up to this point, we have alluded to the fact that the signal-to-noise ratio and the quality of the reconstructed images in imaging correlography increases with the number N of independently observed speckle patterns. More to the point, the error in the speckle autocovariance, and so the Fourier modulus estimate, will improve as the number of speckle measurements increases, whether these speckle measurements arise from additional speckle pattern realizations

FIGURE 3-10. IMAGE RECOVERY USING GOLAY-6 APERTURE, N = 1024. (A) Average energy spectrum of the measured speckle patterns (with dc term removed); (B) estimate of the Fourier modulus of the object brightness distribution; (C) Wiener-like filter for the Golay-6 aperture; (D) filtered Fourier modulus estimate; (E) image reconstructed from (D); (F) original incoherent object; (G) filtered, incoherent object.

(snapshots) or from an increased redundancy in the OTF of the collecting aperture. This flexibility, in choosing between number of snapshots N and collecting array redundancy, can be better appreciated by considering the signal-to-noise ratio (SNR) of the autocovariance estimate achieved in imaging correlography. Assuming that time-sequential measurements of the speckle patterns are statistically independent, we can show that the SNR of the estimate of the object's energy spectrum at spatial frequency Δu provided by the estimator of Eq. (3-7) is given by [3.17, 3.18]

$$ SNR_C(\Delta u; N) = \frac{(N \, L)^{1/2} \, |\mu(\Delta u)|^2}{[3 + 14|\mu(\Delta u)|^2 + 3|\mu(\Delta u)|^4]^{1/2}} \qquad (3\text{-}15) $$

where N is the number of independent speckle patterns (snapshots) observed, $\mu(\Delta u) = \Gamma(\Delta u)/\Gamma(0)$ is the complex coherence factor for the measured speckle field, and

$$ L = L(\Delta u) = N_s \, OTF(\Delta u) \qquad (3\text{-}16) $$

is the number of redundant pairs of speckle intensity in the collecting aperture measured at pixel separation Δu. In the above, N_s is the number of independent samples of intensity (or number of speckles) contained in the measurement aperture H(u). For the case that the noise in the Fourier modulus estimate is dominated by statistical fluctuations in the autocovariance estimate itself (not by photon shot noise, etc.), Eq. (3-15) specifies the trade-off between array redundancy L and number of speckle snapshots N needed to keep the SNR of the estimate at an acceptably high level. Keeping the SNR of the speckle autocovariance, and so the SNR of the estimate of the object's Fourier modulus, at a high level will preserve an acceptable quality in the image recovered using the iterative transform phase-retrieval algorithm.

Notice from Eq. (3-15) that the SNR increases with

(1) increasing aperture size [for a filled aperture SNR α $(L)^{1/2}$ α $(N_s)^{1/2}$ α (aperture area)$^{1/2}$.

(2) increasing object diameter [SNR α $(N_s)^{1/2}$ α (object area)$^{1/2}$]

and

(3) increasing number of snapshots [SNR α $(N)^{1/2}$].

For high spatial frequencies, $|\mu(\Delta u)|^2 \ll 1$ and

$$SNR_c(\Delta u; N) \simeq \sqrt{NN_s \; OTF(\Delta u)} \; |\mu(\Delta u)|^2/\sqrt{3} \quad . \tag{3-17}$$

These higher spatial frequencies are of interest in obtaining resolvable detail in the reconstructed image.

In order to test the accuracy of these SNR expressions, we computer-simulated speckle frames, performed the correlography averaging, and determined the error in the estimate of $|\mu|^2$. Taking the Fourier transform of the data averaged according to Eq. (3-3) yields an OTF-weighted estimate of the power spectrum of the incoherent object, as given by Eq. (3-10). Normalizing that to unity at zero spatial frequency yields an estimate of $OTF(\Delta u)$ $|\mu(\Delta u)|^2$. The variance the estimate of $|\mu|^2$, from Eq. (3-15), is

$$Var\{|\hat{\mu}(\Delta u)|^2\} = [3 + 14|\mu(\Delta u)|^2 + 3|\mu(\Delta u)|^4]/[NN_s \; OTF(\Delta u)] \quad . \tag{3-18}$$

Therefore the variance of the estimate of $OTF(\Delta u)$ $|\mu(\Delta u)|^2$ is

$$Var\{OTF(\Delta u) \; |\hat{\mu}(\Delta u)|^2\} = OTF(\Delta u) \; [3 + 14|\mu(\Delta u)|^2 + 3|\mu(\Delta u)|^4]/(NN_s) \quad .$$
$$\tag{3-19}$$

41

In order to compare theory with simulation results, it is necessary to compute the statistics of the simulated data over large areas in the frequency domain. However, the variability of OTF(Δu) over such an area would confuse the results. Hence we also looked at an estimate of $\sqrt{OTF(\Delta u)} \, |\mu|^2$, which has a variance

$$Var\{\sqrt{OTF(\Delta u)} \, |\mu(\Delta u)|^2\} = OTF(\Delta u) \, Var\{|\mu(\Delta u)|^2\}$$

$$= [3 + 14|\mu(\Delta u)|^2 + 3|\mu(\Delta u)|^4]/(NN_s) \quad (3-20)$$

which is independent of OTF(Δu). Thus we considered the two absolute errors

$$e_w(\Delta u) = OTF(\Delta u) \, |\hat{\mu}(\Delta u)|^2 - OTF(\Delta u) \, |\mu(\Delta u)|^2 \quad (3-21)$$

with the natural OTF weighting, with variance given by Eq. (3-19), and

$$e_u(\Delta u) = \sqrt{OTF(\Delta u)} \, |\hat{\mu}(\Delta u)|^2 - \sqrt{OTF(\Delta u)} \, |\mu(\Delta u)|^2 \quad (3-22)$$

with $\sqrt{OTF}$ weighting, with variance given by Eq. (3-20), which is not weighted by the OTF. This $\sqrt{OTF}$-weighted data was obtained by dividing the naturally-OTF-weighted data by $\sqrt{OTF(\Delta u)}$ [the result was set to zero where OTF(Δu)=0].

Figure 3-11 shows these two absolute errors, for the filled-aperture case described in Section 3.1. The middle-grey areas have zero error, the lighter areas have positive error, and the darker areas have negative error. Figures 3-12 and 3-13 show the same thing for the Golay aperture case described in Section 3.2. Note that for the OTF-weighted case, the error is maximum near Δu=0 (at the center) and falls to zero at the edges where OTF(Δu) $\simeq$ 0, as predicted by Eq. (3-19).

FIGURE 3-11.   FOURIER INTENSITY ERROR FOR FILLED APERTURE.

FIGURE 3-12.   SQUARED   FOURIER   MODULUS   ERROR   FOR   GOLAY-6 APERTURE
(N = 128).

44

FIGURE 3-13.   SQUARED   FOURIER   MODULUS   ERROR   FOR   GOLAY-6 APERTURE
(N = 1024, 10,240).

45

For the $\sqrt{\text{OTF}}$-weighted ("unweighted") case the errors are more uniformly distributed across the frequency plane, as predicted by Eq. (3-20). Because we normalize the estimated data to unity at $\Delta u = 0$, by definition we made the absolute error equal to zero at $\Delta u = 0$. It is interesting to note that the correlation distance of the absolute error appears to decrease as the number, N (K in the figures), of frames averaged, increases. This effect is presently not understood.

The averaging to compute the statistics of the error was done over a 32 x 32-pixels square area shown in Figure 3-13(A) for the Golay-aperture case and in the same-sized square in the corner of the square filled-aperture case. In these areas $\sqrt{\text{OTF}(\Delta u)} \approx 0.20$ for the filled aperture and ≈ 0.10 for the Golay aperture. In both cases, since the object fits within a rectangle of size 40 x 60 pixels embedded in a 128 x 128 array, the number of samples per speckle in the aperture plane is (128 x 128)/(40 x 60) = 6.83. The areas of the filled and Golay apertures were measured to be 64 x 64 = 4096 and 822 pixels, respectively. Consequently, the value of N_s, the number of speckles in the aperture is 4096/6.83 = 600 for the filled aperture and 822/6.83 = 120 for the Golay aperture. These areas of integration were chosen to be at large $|\Delta u|$ for which $|\mu(\Delta u)| \ll 1$, so that the theoretical variance expressions simplify to

$$\text{Var}[\text{OTF}(\Delta u) \, |\hat{\mu}(\Delta u)|^2] \approx 3 \, \text{OTF}(\Delta u)/(NN_s) \qquad (3\text{-}23)$$

and

$$\text{Var}[\sqrt{\text{OTF}(\Delta u)} \, |\hat{\mu}(\Delta u)|^2] \approx 3/(NN_s) \, . \qquad (3\text{-}24)$$

In addition, for the $\sqrt{\text{OTF}} \, |\mu|^2$ case, averages of the statistics were taken over the entire array in order to obtain better statistics. In this case it was also assumed that $|\mu| \ll 1$ enabling us to use Eqs. (3-23) and (3-24). Although it is not true for small values of $|\Delta u|$,

these areas are relatively small compared with the total array size; consequently, when averaging over the entire array the assumption that $|\mu|^2 \ll 1$ is reasonable.

Table 3-1 compares the theoretical expressions for the noise variance given by Eqs. (3-23) and (3-24) with the measured variance of the simulated data. Individual values do not agree very well because it was not possible to integrate over large enough areas to get good statistics. The last column, the ratio of the measured variance to the theoretical variance, shows that for roughly half the cases the measured variance exceeded the theoretical variance, and for the other half it was less. Thus on average the measured noise variance roughly agrees with the theoretical expression, giving confirmation of the theory.

Next we compute the number of frames required to achieve a given resolution for a particular imaging scenario. Figure 3-14 [3.19] shows the spin (angularly) averaged $|\mu(\Delta u)|^2$ for the satellite object at a finer resolution than for the version of the image shown earlier in this Section. For this version the object fit within a 128 x 128 array embedded in a 256 x 256 array, and its Fourier transform was not weighted by an OTF function. Hence its resolution was about 4 times better in each dimension than the image shown in Figure 3-2(G). The value of $|\Delta u|$ at the highest spatial frequency shown in Figure 3-14 is therefore equivalent to collecting an array of about 128 x 128 speckles. Thus an aperture of size 32 x 32 speckles would achieve a resolution equivalent to $\Delta u = 0.25$ on this chart, at which $|\mu|^2 \approx 0.012$. At half this spatial frequency (i.e., $\Delta u = 0.125$ on this plot) one would have $|\mu|^2 \approx 0.02$. Achieving resolution at one-half the highest spatial frequency passed by the aperture is a reasonable goal, since for that spatial frequency $OTF(\Delta u) \approx 0.5$, whereas for higher spatial frequencies the SNR given by Eq. (3-17) drops off rapidly

Table 3-1

Comparison of Noise Variance Theory
with Simulations

For OTF(Δu) $|\hat{\mu}(\Delta u)|^2$, 32 x 32 regions where $|\mu|^2 \ll 1$:

Aperture	N	σ^2 Theory	σ^2 Measured	Ratio
Filled	1,024	.10 E-5	.40 E-6	0.4
Filled	1,024	.10 E-5	.62 E-6	0.6
Filled	10,000	.10 E-6	.19 E-6	1.9
Filled	10,000	.10 E-6	.25 E-6	2.5
Golay	128	.20 E-4	.37 E-4	1.8
Golay	1,024	.25 E-5	.13 E-5	0.5
Golay	10,240	.25 E-6	.12 E-6	0.5

For $\sqrt{OTF(\Delta u)}$ $|\hat{\mu}(\Delta u)|^2$, entire array, assume $|\mu|^2 \ll 1$:

Aperture	N	σ^2 Theory	σ^2 Measured	Ratio
Filled	1,024	.3 E-5	.26 E-5	0.9
Filled	10,000	.3 E-6	.76 E-6	2.5
Golay	128	.20 E-3	.26 E-3	1.3
Golay	1,024	.24 E-4	.15 E-4	0.6
Golay	10,240	.24 E-5	.13 E-5	0.5

because both OTF(Δu) and $|\mu(\Delta u)|^2$ are decreasing rapidly. Plugging these numbers ($N_s = 32 \times 32$, OTF $= 0.5$, $|\mu|^2 = 0.02$) into Eq. (3-17) yields $SNR_c \simeq 0.26N^{1/2}$. Therefore in order to achieve a given SNR_c for this example, the required number of independent frames is $N \simeq 15\ SNR_c^2$. If, for example, a faithful image requires $SNR_c = 10$, then 1,500 frames would be required to achieve a faithful image. Recall that, for this example, since 32×32 speckles were assumed to be in the filled aperture, and 1/2 the maximum spatial frequency was reconstructed, then this image would have a space-bandwidth product of 16×16 resolution elements (e.g.: 20 cm resolution for an object of width 3.2m in diameter).

If the array size were doubled in each dimension in order to achieve 10 cm resolution, then $N_s = 64 \times 64$, keep OTF(Δu) $= 0.5$, from Figure 3-14 $|\mu|^2 \simeq 0.012$, and $SNR_c \simeq 0.31\ N^{1/2}$; and one needs $N \simeq 10\ SNR_c$. For $SNR_c = 10$, this requires $N = 1,000$ frames. Thus from this example, we see that as the array size and resolution increase, the number of frames can decrease. However, this is not always the case: it depends upon whether the product of the aperture length with $|\mu(\Delta u)|^2$ increases or decreases as the aperture length and Δu increase together; this depends upon the characteristics of the target. An object consisting of a small collection of point-like scatterers or dominated by glints will have a $|\mu(\Delta u)|^2$ that falls off much more slowly than for a uniform, very extended object. Consequently the point-like objects require far fewer frames to achieve a given resolution. Note also that for the example of the larger aperture, in order to get the 20 cm resolution one could be required to gather only $N \simeq 4\ SNR_c^2$, or 400 frames for $SNR_c = 10$, versus 1,500 frames required for the smaller aperture. Thus, we see the trade-off between the array area (in particular its redundancy) and the number of frames in order to achieve a given SNR_c at a given spatial frequency: it is the product NN_s OTF(Δu) that matters.

49
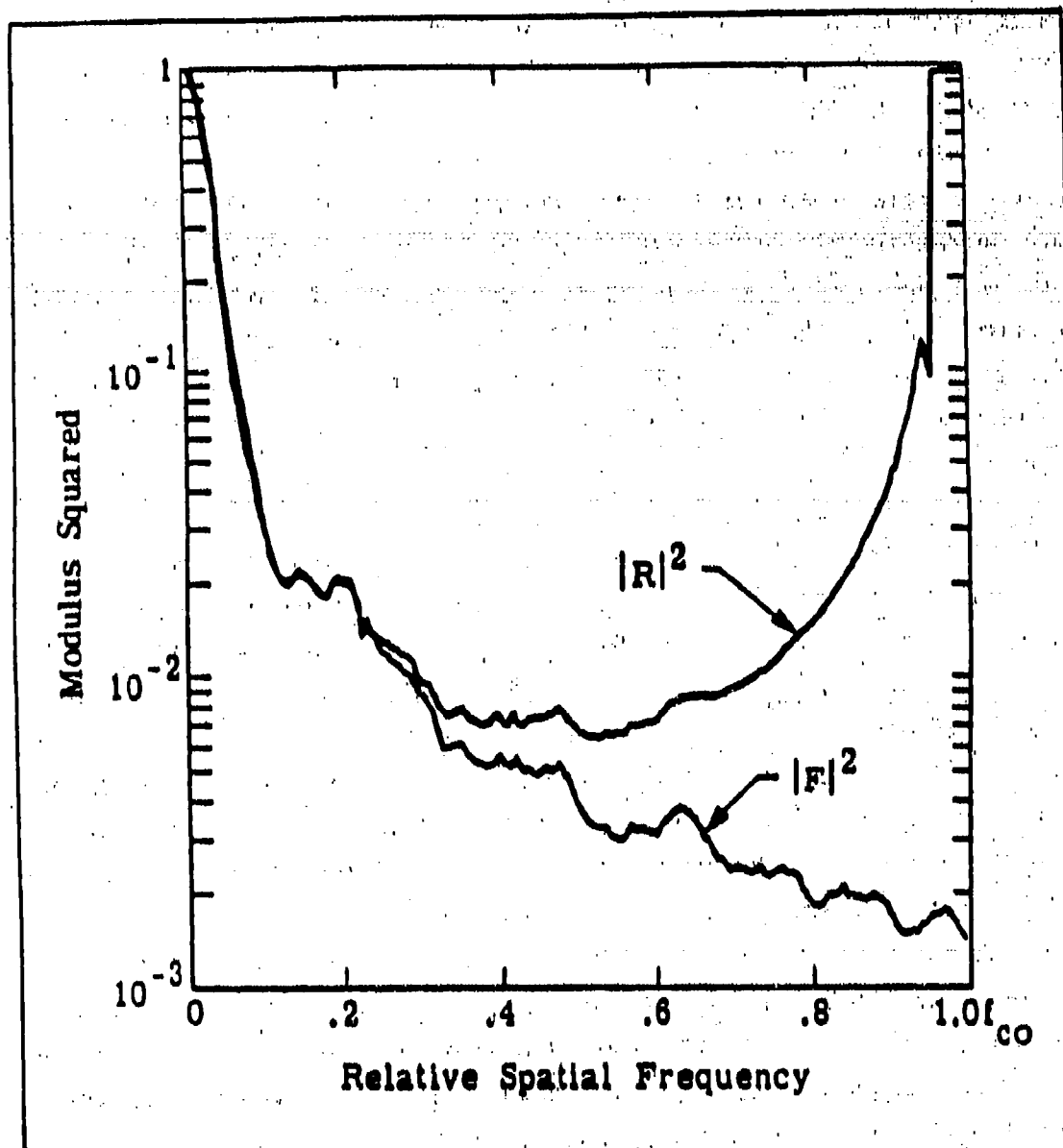
FIGURE 3-14. SQUARED FOURIER MODULUS FOR P72-2 SATELLITE MODEL (FROM REF. 3.19).

The above noise analysis included only the effects of approximating the ensemble average by averaging over a finite number of realizations. The variance of the noise that includes both finite averaging noise and photon noise is given by $[NN_s \, OTF(\Delta u)]^{-1}$ times [3.18]

$$(3 + 14 \, |\mu|^2 + 3 \, |\mu|^4) + \left[\frac{4(1 + 2 \, |\mu|^2)}{M \, <n>} + \frac{1 + |\mu|^2}{M \, <n>^2} \right]$$

where the first set of terms is due to finite averaging and the second is due to photon noise, M is the number of detectors (pixels) per speckle, and $<n>$ is the mean number of photons per detector. Thus for $|\mu|^2 \ll 1$, the finite averaging noise variance is proportional to 3, while the photon noise variance is proportional to $4/(M <n>) + 1/(M <n>^2)$. For M = 4, the two noise variances are equal for $<n>$ = 1/2 photon per detector or M $<n>$ = 2 photons per speckle. Consequently, independent of the array redundancy and the number of realizations, photon noise will be negligible as long as the number M $<n>$ of photons per speckle is much greater than two.

In summary, we have demonstrated via computer simulations that it is possible in principle to recover an incoherent image of a laser-illuminated object from multiple realizations of detected speckle intensities collected over sparse arrays. This would permit the reconstruction of fine-resolution images despite phase errors due to atmospheric turbulence. The expressions for signal-to-noise ratio as a function of spatial frequency, array redundancy, and number of speckle realizations shows that large amounts of array redundancy and/or large numbers of speckle realizations are required to reconstruct an image of large space-bandwidth product.

Sections 3.2 and 3.3 are an expansion of References 3.20 to 3.22.

3.4 WIENER FILTERING

The Wiener-Helstrom filters given by Eqs. (3-11) and (3-14) were shown to improve image quality; however, they are probably not the optimum linear filters. In this section, we describe two different filters that could yield better results and a different formulation of the problem that would lead to a different filter. Since none of these were implemented and proven, they should be considered speculative at this point.

3.4.1 Recursive Wiener Filter

In the Wiener-Helstrom filters given by Eqs. (3-11) and (3-14), we must know both an average power spectrum of the signal (estimated by $|\Gamma|^2$ and $|\Gamma|^4$, respectively) and the power spectrum of the noise, $E_n(\Delta u)$. The noise can often be determined by measuring the signal plus noise in a region of spatial-frequency space where the signal is small. In practice, estimation of the power spectrum of the object is a bigger problem. Use of spin-averages of an ensemble of images from the class of objects of interest is one approach. Another approach is to use the realization of the given data. This can be done by the method that follows.

For simplicity, first consider the conventional imaging model:

$$g = s * g_o + n \qquad\qquad (3-25)$$

where
$\qquad g_o$ = the ideal image

$\qquad s$ = the psf

$\qquad n$ = noise

$\qquad g$ = the measured image

52

which, in the Fourier domain is

$$G = SG_0 + N \quad . \tag{3-26}$$

Assuming g_0 and n are independent stochastic processes, both zero-mean Gaussians, then the least mean-squared error linear estimator for g_0 is $\hat{g}_0 = \mathcal{F}^{-1}\left[\hat{G}_0\right]$ where [3.14]

$$\hat{G}_0 = WG \tag{3-27}$$

and

$$W = \frac{S^*|G_0|^2}{|S|^2 |G_0|^2 + |N|^2} = \frac{S^*}{|S|^2 + |N|^2/|G_0|^2} \tag{3-28}$$

where $|N|^2$ and $|G_0|^2$ are the power spectral densities of the object and the noise, respectively. Helstrom notes that although the images generally will not satisfy the statistical assumption stated above, "Nevertheless... it can be expected to be effective when applied to these images as well." So the Wiener-Helstrom filter is not optimum, but it should be effective and it is very simple to use.

A big problem with the Wiener-Helstrom filter is that, although S is often known very well from the system parameters and the expected $|N|^2$ can be analyzed ahead of time, the object power spectrum, $|G_0|^2$ is usually unknown. Helstrom suggested using a constant for $|G_0|^2$. However, this is a very bad assumption since it is well known that the power spectra of real, nonnegative objects has a large peak at low spatial frequencies and then drops off at higher frequencies, typically at a rate proportional to (spatial frequency)$^{-1}$.

A new method is to use the data itself as the estimate of the object power spectrum. Namely, use

$$|\hat{G}_0|^2 = |G|^2 \; . \tag{3-29}$$

However, as seen from Eq. (3-26), this may be a poor estimate. Using this estimate in Eqs. (3-27) and (3-28) yields the Wiener-filtered Fourier transform

$$G_1 = W_0 G \tag{3-30}$$

where

$$W_0 = \frac{S^*}{|S|^2 + |N|^2/|G|^2} \; . \tag{3-31}$$

Now $|G_1|^2$ is a better estimate of $|G_0|^2$ than $|G|^2$ is. Therefore it makes sense to form a new Wiener filter

$$W_1 = \frac{S^*}{|S|^2 + |N|^2/|G_1|^2} \tag{3-32}$$

and apply this to the data. This supposedly will yield a better estimate still. Thus we can get successively better approximations of the Wiener filter, W_n, and of the object's power spectrum, $|G_{n+1}|^2 = |W_n G|^2$, via

$$W_n = \frac{S^*}{|S|^2 + |N|^2/|G_n|^2} \; . \tag{3-33}$$

The recursive estimation of the object's power spectrum will converge to a stable solution when

$$|G_\infty|^2 = |G_{n+1}|^2 = |G_n|^2$$

$$= \left| \frac{S*G}{|S|^2 + |N|^2/|G_n|^2} \right|^2 \qquad (3\text{-}34)$$

Solving for $|G_\infty|^2$:

$$|G_\infty|^2 = 0$$

or

$$|G_\infty|^4 \, |S|^4 + |G_\infty|^2 \, |S|^2 \, (2|N|^2 + |G|^2) + |N|^4 = 0 \qquad (3\text{-}35)$$

which simplifies to

$$|G_\infty|^2 = \left(2|S|^2 \right)^{-1} \left(|G|^2 - 2|N|^2 \pm \sqrt{|G|^4 - 4|N|^2 \, |G|^2} \right) . \qquad (3\text{-}36)$$

Note that for $|G|^2 \gg |N|^2$, $|G_\infty|^2$ approaches $|G|^2/|S|^2$ for the positive-square-root solution, the expected result. In this same limit, the negative square root yields zero, and so only the positive square root should be used in Eq. (3-36). Plugging this into Eq. (3-33) yields

$$W_\infty = \frac{S* \left(|G|^2 - 2|N|^2 + \sqrt{|G|^4 - 4|N|^2 \, |G|^2} \right)}{|S|^2 \left(|G|^2 + \sqrt{|G|^4 - 4|N|^2 \, |G|^2} \right)} \qquad (3\text{-}37a)$$

$$= \frac{S* \left(1 + \sqrt{1 - 4|N|^2/|G|^2} \right)}{2|S|^2} \qquad (3\text{-}37b)$$

55

$$= \frac{2S^* |N|^2/|G|^2}{|S|^2 \left[1 - \sqrt{1 - 4|N|^2/|G|^2}\right]} \quad . \tag{3-37c}$$

Note that for $|N|^2/|G|^2 \ll 1$,

$$W_\infty = \frac{S^*}{|S|^2} \left[1 - \frac{|N|^2}{|G|^2}\right] \tag{3-38}$$

and as $|N|^2/|G|^2 \rightarrow (1/4)^-$,

$$W_\infty \rightarrow \frac{1}{2} \frac{S^*}{|S|^2} \quad . \tag{3-39}$$

For $|N|^2/|G|^2 > 1/4$, Eq. (3-37) is invalid. By performing the recursive calculation of Eq. (3-33) for this situation, it was found that $|G_n|^2$ became progressively smaller, so that for $|N|^2/|G|^2 > 1/4$,

$$|G_\infty|^2 \rightarrow 0 \text{ and } W_n \rightarrow 0 \quad . \tag{3-40}$$

It has not yet been assessed which of the Wiener filters discussed above is best.

Conversion of these results to the case of imaging correlography is accomplished by replacing G in the equations above by $\hat{C}_I(\Delta u; N)$.

3.4.2 Iterative Nonlinear Filter

A completely different approach to filtering is as follows. Suppose that $g_0(x)$ and $g(x)$ of Eq. (3-25) are spatially limited to some support defined by

$$g_s(x) = \begin{cases} 1 & , & x{:}g_0(x) > 0 \\ 0 & , & x{:}g_0(x) = 0 \end{cases} \tag{3-41}$$

for a nonnegative $g_0(x)$ and $g(x)$. Further it is assumed that the support, $S_s(u)$, of $S(u)$:

$$S_s(u) = \begin{cases} 1 & , & u{:}S(u) > 0 \\ 0 & , & u{:}S(u) = 0 \end{cases} \tag{3-42}$$

is known. Then we can use the iterative transform algorithm to better estimate $g_0(x){*}s(x)$ and $G_0(u) \, S(u)$ by iteratively setting successive estimates of $G_0(u) \, S(u)$ to zero wherever $S_s(u) = 0$ and setting successive estimates of $g_0(x){*}s(x)$ to zero whenever it is negative or where $g_s(x)$ is zero. Since functions satisfying these conditions in both domains form convex sets, this error-reduction algorithm is a projections-onto-convex-sets (POCS) algorithm which, by Youla's analysis [3.23], has strong convergence properties (it may not be unique, though). This iterative would reduce the noise and is an alternative to Wiener filtering.

3.4.3 Improved Noise Model

The new methods for filtering described above attempt to makeup for the lack of knowledge of the power spectrum of the signal. In this section we point out that additional analysis needs to be performed in order to properly model the noise.

The two signal-plus-noise models assumed for the filtering actually performed were [see Eq. (3-12)] $OTF(\Delta u)\ \Gamma(\Delta u) + N$ and $OTF(\Delta u)\ |\Gamma(\Delta u)|^2 + N_c$. After the image reconstruction experiments were oerformed, the signal-to-noise ratio, proportional to $\sqrt{OTF}$, given by Eqs. (3-15)-(3-17), was analyzed. Since the signal is proportional to OTF, this implies that the noise is also proportional to $\sqrt{OTF}$. This fact was verified by the analysis and digital experimental described in Section 3.3. Thus in order to derive an optimum linear filter for imaging correlography it will be necessary, in future research, to derive a new Wiener-type filter based on a model in which the additive noise is weighted by $\sqrt{OTF}$.

REFERENCES

[3.1] J.W. Goodman, "Statistical Properties of Laser Speckle Patterns," in _Laser Speckle and Related Phenomena_, 2nd ed., J.C. Dainty, ed. (Springer-Verlag, New York, 1984), pp. 9-75.

[3.2] L.I. Goldfischer, "Autocorrelation Function and Power Spectral Density of Laser-Produced Speckle Patterns," J. Opt. Soc. Am. **55**, 247-253 (1965).

[3.3] R.N. Bracewell, _The Fourier Transform and its Applications_, (McGraw-Hill, San Francisco, 1978), p. 115.

[3.4] J.R. Fienup, "Reconstruction of an Object from the Modulus of Its Fourier Transform," Opt. Lett. **3**, 27-29 (1978).

[3.5] J.R. Fienup, "Phase Retrieval Algorithms: A Comparison," Appl. Opt. **21**, 2758-2769 (1982).

[3.6] J.R. Fienup and C.C. Wackerman, "Phase Retrieval Stagnation Problems and Solutions," J. Opt. Soc. Am. A **3**, 1897-1907 (1986).

[3.7] J.R. Fienup, "Reconstruction of a Complex-Valued Object from the Modulus of Its Fourier Transform Using a Support Constraint," J. Opt. Soc. Am. A **4**, 118-123 (1987).

[3.8] S. Lowenthal and H. Arsenault, "Image Formation for Coherent Diffuse Objects: Statistical Properties," J. Opt. Soc. Am. **60**, 1478-1483 (1970).

[3.9] R. Hanbury-Brown, _The Intensity Interferometer_, (Taylor and Francis, London, 1974).

[3.10] P.S. Idell, J.D. Gonglewski, D.G. Voelz, J. Knopp and B. Speilbusch, "Image Synthesis from Nonimaged Laser Speckle Patterns: Experimental Verification," J. Opt. Soc. Am. A **4** (13) p. 27 (1987).

[3.11] P.S. Idell, J.R. Fienup and R.S. Goodman, "Image Synthesis from Nonimaged Laser Speckle Patterns," Opt. Lett. **12**, 858-860 (1987).

[3.12] J.W. Goodman, _Statistical Optics_ (John Wiley and Sons, New York, 1985), p. 207.

[3.13] Reference 3.12, p. 271.

[3.14] C.W. Helstrom, "Image Restoration by the Method of Least Squares," J. Opt. Soc. Am. 57, 297-303 (1967).

[3.15] M. Golay, "Point Arrays Having Compact Nonredundant Autocorrelations," J. Opt. Soc. Am. 61, 272-273 (1971).

[3.16] J.R. Fienup, T.R. Crimmins and W. Holsztynski, "Reconstruction of the Support of an Object from the Support of Its Autocorrelation," J. Opt. Soc. Am. 72, 610-624 (1982).

[3.17] J.C. Marron, "Accuracy of Fourier Magnitude Estimation from Speckle Intensity Measurements," J. Opt. Soc. Am. A 5, 864-870 (1988).

[3.18] K. O'Donnell, "Time-Varying Speckle Phenomena in Astronomical Imaging and in Laser Scattering," Ph.D. Thesis, University of Rochester, Rochester, N.Y. (1983).

[3.19] G.B. Feldkamp and J.R. Fienup, "Noise Properties of Images Reconstructed from Fourier Modulus," in 1980 International Optical Computing Conference, W.T. Rhodes, ed., Proc. SPIE 231, 84-93 (1980).

[3.20] P.S. Idell and J.R. Fienup, "Imaging Correlography with Sparse Collecting Arrays," in Digital Image Recovery and Synthesis, Proc. SPIE 828-21 (August 1987).

[3.21] J.R. Fienup and P.S. Idell, "Imaging Correlography with Sparse Arrays of Detectors," Opt. Engr. 27, 778-784 (1988).

[3.22] J.R. Fienup, R.S. Goodman and P.S. Idell, "Incoherent Image Reconstruction from Multiple Laser Speckle Patterns," J. Opt. Soc. Am. A 4(13), p. 105 (1987) (abstract).

[3.23] D.C. Youla, "Generalized Image Restoration by the Method of Alternating Projections," IEEE Trans. Circuits, Systems, CAS-25, 694-702 (1978).

4.0 IMAGING AND CORRELOGRAPHY WITH A MIXED OBJECT

4.1 INTRODUCTION

In the previous section it was assumed, for the multiple realizations employed in imaging correlography, that the optical fields reflected by the object are diffuse, zero mean, and uncorrelated. However this will not be true when the object has one or more glint components. In this section we analyze the case in which the object's reflectivity contains both a diffuse component and a glint, or deterministic, component. Here we consider not only imaging correlography, but other imaging modalities as well.

In most instances we model the imaging process as either coherent or incoherent. From a coherent system one can get an incoherent image either by (1) noncoherently averaging the intensities of many coherent images or (2) by heterodyne interferometry with multiple realizations or (3) by imaging correlography, which involves first averaging the autocorrelations of the intensities of the aperture-plane fields to estimate the energy spectrum of the incoherent object, then reconstructing an image by phase retrieval. In the analysis of the formation of an incoherent image from multiple realizations of coherent data, one usually assumes that the object is diffuse. In what follows we analyze the case for a mixed object, i.e. one that contains both a deterministic component and a diffuse, variable component. All three modes of obtaining an incoherent image from coherent data of a mixed object will be analyzed.

4.2 MIXED OBJECT MODEL

We assume that the object is coherently illuminated and that its complex amplitude reflectivity consists of two components, a deterministic component $g(x)$ (where x is a 2-D spatial or angular coordinate) and a diffuse component, $d_n(x)$:

$$f_n(x) = g(x) + d_n(x) \quad . \qquad (4-1)$$

The subscript n indicates the realization number, where $d_n(x)$ is assumed to have different realizations of phase, due to a rough surface-height distribution, as the look angle changes slightly. The underlying incoherent object, i.e. the object intensity reflectivity had it been illuminated by incoherent light, of the diffuse component is given by

$$d_I(x) = <|d_n(x)|^2>_n \qquad (4-2)$$

where $<\bullet>_n$ denotes an ensemble average. We assume that $d_n(x)$ is zero mean and spatially uncorrelated:

$$<d_n(x)>_n = 0 \qquad (4-3a)$$

and

$$<d_n(x_1) \, d_n^*(x_2)>_n = d_I(x_1) \, \delta(x_1 - x_2) \quad . \qquad (4-3b)$$

In the aperture plane, in the far-field relative to the object, the complex amplitude of the backscattered radiation is given by the Fourier transform of the coherent object,

$$F_n(u) = G(u) + D_n(u) \qquad (4-4)$$

62

where the functions represented by uppercase letters are the Fourier transforms of the functions represented by the corresponding lowercase letters, and u is a 2-D coordinate in the aperture plane. The component $G(u)$ is deterministic. The diffuse component has the following properties:

$$<D_n(u)>_n = 0 \qquad (4\text{-}5)$$

and

$$<D_n(u_1)\ D_n^*(u_2)>_n = \Gamma_D(u_1 - u_2) = \Gamma_D(\Delta u) \qquad (4\text{-}6)$$

where superscript * denotes complex conjugate, $\Delta u = u_1 - u_2$, and, by the van Cittert-Zernike theorem,

$$\Gamma_D(\Delta u) = \mathcal{F}[d_I(x)] \qquad (4\text{-}7)$$

where $\mathcal{F}$ denotes Fourier transformation. $|D_n(u)|^2$ would be a fully-developed speckle pattern (with negative exponential point statistics) and $D_n(u)$ is circular-complex Gaussian (ccg) distributed.

An example of an object satisfying the assumptions above is one with a rough component, $d_n(x)$, that rotates slightly to result in different realizations, plus an unchanging component $g(x)$. The unchanging component could be a part that does not rotate or it could be a single unresolved corner reflector or stable glint.

4.3 NONCOHERENT AVERAGING OF COHERENT IMAGES

A single realization of a coherent image of the object through an aperture $A(u)$, with coherent impulse response $a(x) = \mathcal{F}^{-1}[A(u)]$, is

63

$$a(x) * f_n(x) = a(x) * g(x) + a(x) * d_n(x) \quad , \qquad (4\text{-}8)$$

where $*$ denotes convolution. The average image intensity is

$$\langle |a(x) * f_n(x)|^2 \rangle_n = |a(x) * g(x)|^2 + \langle |a(x) * d_n(x)|^2 \rangle_n$$

$$+ [a^*(x) * g^*(x)] [a(x) * \langle d_n(x) \rangle_n] + c.c. \qquad (4\text{-}9)$$

where c.c. denotes complex conjugate. The second term is

$$\langle |a(x) * d_n(x)|^2 \rangle_n = \langle |\int a(x_1) d_n(x - x_1) dx_1|^2 \rangle_n$$

$$= \int \int a(x_1) a^*(x_2) \langle d_n(x - x_1) d_n^*(x - x_2) \rangle_n dx_1 dx_2$$

$$= \int |a(x_1)|^2 d_I(x - x_1) dx_1$$

$$= |a(x)|^2 * d_I(x) \qquad (4\text{-}10)$$

where use was made of Eq. (4-3b). Using this and Eq. (4-3a), Eq. (4-9) simplies to

$$\langle |a(x) * f_n(x)|^2 \rangle_n = |a(x) * g(x)|^2 + |a(x)|^2 * d_I(x) \quad . \quad (4\text{-}11)$$

That is, in the noncoherently averaged intensity image of a mixed object, the deterministic component images as in a coherent system (i.e., convolution with the coherent impulse response, then modulus squared) while the diffuse component images as in an incoherent system (i.e., incoherent object convolved with the incoherent impulse response which is the squared modulus of the coherent impulse response). This result holds both for optical imaging systems and for microwave SAR. More about this image will be said in the next section.

64

4.4 HETERODYNE-INTERFEROMETRY AVERAGING

The second imaging mode is to measure complex fields in the aperture plane using heterodyne detection, then calculate the average coherence function for multiple realizations. This differs somewhat from conventional amplitude interferometry, since (ignoring aperture effects for the moment)

$$\Gamma_F(u_1, u_2) = <F_n(u_1) \, F_n^*(u_2)>_n$$

$$= G(u_1) \, G^*(u_2) + <D_n(u_1) \, D_n^*(u_2)>_n$$

$$+ G^*(u_1) <D_n(u_2)>_n + c.c.$$

$$= G(u_1) \, G^*(u_2) + \Gamma_D(u_1 - u_2) \qquad (4\text{-}12)$$

is not stationary due to the presence of the deterministic term. Direct image reconstruction from $\Gamma_F(u_1, u_2)$ is not possible because the two terms on the right-hand side of Eq. (4-12) cannot be easily separated out.

Consider the use of spatial integration or averaging. We denote

$$< \bullet >_s = \int \bullet \, du_1 \qquad (4\text{-}13)$$

We also write $<<\bullet>_n>_s$ as $<\bullet>_{ns}$. Including the aperture functions explicitly in Eq. (4-12) and spatially integrating the ensemble average, for a given value of $\Delta u = u_1 - u_2$ (or $u_2 = u_1 - \Delta u$), yields

$$\langle A(u_1)\, A(u_2)\, \Gamma_F(u_1,\, u_2)\rangle_s = \langle A(u_1)\, F_n(u_1)\, A(u_2)\, F_n^*(u_2)\rangle_{ns}$$

$$= \langle A(u_1)\, G(u_1)\, A(u_2)\, G^*(u_2)\rangle_s + \langle A(u_1)\, A(u_2)\, \Gamma_D(u_1 - u_2)\rangle_s$$

$$= (AG)\bullet(AG)(\Delta u) + S(\Delta u)\, \Gamma_D(\Delta u) \qquad\qquad (4\text{-}14)$$

where $(AG)\bullet(AG)(\Delta u)$ denotes the autocorrelation of $A(u)\, G(u)$ evaluated at Δu, and $S(\Delta u)$ is proportional to the optical transfer function due to the aperture $A(u)$:

$$S(\Delta u) = A\bullet A(\Delta u) = \langle A(u_1)\, A(u_2)\rangle_s$$

$$= A_o\, OTF(\Delta u) \qquad\qquad (4\text{-}15)$$

where $OTF(\Delta u)$ is the optical transfer function for the aperture $A(u)$ and

$$A_o = \int A^2(u)\, du \quad . \qquad\qquad (4\text{-}16)$$

Inverse Fourier transforming Eq. (4-14) as a function of Δu, one gets the image

$$|a(x) * g(x)|^2 + |a(x)|^2 * d_I(x) = \langle |a(x) * f_n(x)|^2\rangle_n \qquad (4\text{-}17)$$

which is identical to the noncoherently averaged intensity image in Eq. (4-11). We refer to this image as the incoherent image of the mixed object. It is not clear whether there exists an incoherent object that would give rise to such an image, but for convenience we define the incoherent mixed object, $f_I(x)$, by

$$|a(x)|^2 * f_I(x) = <|a(x) * f_n(x)|^2>_n \quad . \tag{4-18}$$

The Fourier transform of the incoherent image of the incoherent mixed object is

$$S(\Delta u) \; F_I(\Delta u) = (AG) \oplus (AG)(\Delta u) + S(\Delta u) \; \Gamma_D(\Delta u) \tag{4-19}$$

where $F_I(\Delta u)$ is the Fourier transform of the incoherent mixed object.

From Eqs. (4-1), (4-2), and (4-3a), the noncoherently averaged object is

$$<|f_n(x)|^2>_n = |g(x)|^2 + <|d_n(x)|^2>_n$$

$$+ g^*(x) <d_n(x)>_n + c.c.$$

$$= |g(x)|^2 + d_I(x) \tag{4-20}$$

An incoherent image of the noncoherently averaged object would be

$$|a(x)|^2 * <|f_n(x)|^2>_n = |a(x)|^2 * |g(x)|^2 + |a(x)|^2 * d_I(x) \quad . \tag{4-21}$$

Note that this generally differs from the incoherent image of the mixed object in Eqs. (4-11) and (4-17), except when $g(x)$ is a single delta-function, in which case they are the same, that is $|a(x)|^2 * |g(x)|^2 = |a(x) * g(x)|^2$. Consequently, the noncoherently averaged object is generally different from the incoherent mixed object. From Eq. (4-19), the incoherent mixed object would be the inverse Fourier transform of $S^{-1}(\Delta u) \; [(AG) \oplus (AG)(\Delta u)] + \Gamma_D(\Delta u)$. However, it is not clear whether the first term yields a reasonable "object" component in the general case.

4.5 CORRELOGRAPHY/INTENSITY INTERFEROMETRY

In conventional correlography (diffuse component only), since $D_n(u)$ is ccg, the Gaussian moment theorem can be used to obtain (ignoring aperture effects for the moment)

$$<|D_n(u_1)|^2 \, |D_n(u_2)|^2>_n = |<D_n(u_1) \, D_n^*(u_2)>_n|^2 + <|D_n(u_1)|^2>_n <|D_n(u_2)|^2>_n$$

$$= |\Gamma_D(u_1 - u_2)|^2 + T_D^2 \qquad (4\text{-}22)$$

where T_D is the average intensity, so that the desired energy spectrum of $d_I(x)$ can be obtained from the measured data:

$$|\Gamma_D(u_1 - u_2)|^2 = <|D_n(u_1)|^2 \, |D_n(u_2)|^2>_n - T_D^2 \quad . \qquad (4\text{-}23)$$

Since all the terms in Eq. (4-23) are stationary, spatial averaging can also be included in Eq. (4-23) to yield the same result.

For the mixed-object case, represented by Eqs. (4-1) and (4-4), the expression analogous to Eq. (4-22) has sixteen terms:

$$<|F_n(u_1)|^2 \, |F_n(u_2)|^2>_n$$

$$= |G(u_1)|^2 \, |G(u_2)|^2 + |G(u_1)|^2 <|D_n(u_2)|^2>_n + |G(u_2)|^2 <|D_n(u_1)|^2>_n$$

$$+ |G(u_1)|^2 \Big[G^*(u_2) <D_n(u_2)>_n + c.c. \Big] + |G(u_2)|^2 \Big[G^*(u_1) <D_n(u_1)>_n + c.c. \Big]$$

$$+ <|D_n(u_1)|^2 \, |D_n(u_2)|^2>_n$$

$$+ G^*(u_2) <D_n(u_2) \, |D_n(u_1)|^2>_n + c.c.$$

$$+ G^*(u_1) \; \langle D_n(u_1) \; |D_n(u_2)|^2 \rangle_n + c.c.$$

$$+ G^*(u_1) \; G^*(u_2) \; \langle D_n(u_1) \; D_n(u_2) \rangle_n + c.c.$$

$$+ G^*(u_1) \; G(u_2) \; \langle D_n(u_1) \; D_n^*(u_2) \rangle_n + c.c. \quad . \tag{4-24}$$

Using $\langle D_n(u_1) \rangle_n = 0$, $\langle D_n(u_2) \; |D_n(u_1)|^2 \rangle_n = 0$, and $\langle D_n(u_1) \; D_n(u_2) \rangle_n = 0$, this simplifies to

$$\langle |F_n(u_1)|^2 \; |F_n(u_2)|^2 \rangle_n = |G(u_1)|^2 \; |G(u_2)|^2$$

$$+ |G(u_1)|^2 \langle |D_n(u_2)|^2 \rangle_n + |G(u_2)|^2 \langle |D_n(u_1)|^2 \rangle_n$$

$$+ |\Gamma_D(u_1 - u_2)|^2 + \langle |D_n(u_1)|^2 \rangle \langle |D_n(u_2)|^2 \rangle_n$$

$$+ G^*(u_1) \; G(u_2) \; \Gamma_D(u_1 - u_2) + c.c.$$

$$= \langle |F_n(u_1)|^2 \rangle_n \langle |F_n(u_2)|^2 \rangle_n + |\Gamma_D(u_1 - u_2)|^2$$

$$+ G^*(u_1) \; G(u_2) \; \Gamma_D(u_1 - u_2) + c.c. \tag{4-25}$$

where we have used, from Eq. (4-4),

$$\langle |F_n(u)|^2 \rangle_n = \langle |G(u) + D_n(u)|^2 \rangle_n$$

$$= |G(u)|^2 + \langle |D_n(u)|^2 \rangle_n + \langle G^*(u) \; D_n(u) \rangle_n + c.c.$$

$$= |G(u)|^2 + \langle |D_n(u)|^2 \rangle_n$$

$$= |G(u)|^2 + \Gamma_D(0) \quad . \tag{4-26}$$

Notice that Eq. (4-25) is not stationary.

Now consider the spatial integration of Eq. (4-25), in which we include explicit aperture functions:

$$\langle A(u_1) \, |F_n(u_1)|^2 \, A(u_2) \, |F_n(u_2)|^2 \rangle_{ns}$$

$$= \langle A(u_1) \, \langle |F_n(u_1)|^2 \rangle_n \, A(u_2) \, \langle |F_n(u_2)|^2 \rangle_n \rangle_s$$

$$+ \langle A(u_1) \, A(u_2) \, |\Gamma_0(u_1 - u_2)|^2 \rangle_s$$

$$+ \langle A(u_1) \, G^*(u_1) \, A(u_2) \, G(u_2) \, \Gamma_0(u_1 - u_2) \rangle_s + c.c. \qquad (4-27)$$

$$= (A \, \langle |F_n|^2 \rangle_n) \bullet (A \, \langle |F_n|^2 \rangle_n)(\Delta u) + S(\Delta u) \, |\Gamma_0(\Delta u)|^2$$

$$+ [(AG) \bullet (AG)(\Delta u)]^* \, \Gamma_0(\Delta u) + c.c. \qquad (4-28)$$

where $\Delta u = u_1 - u_2$. From Eq. (4-19) we have

$$S^2(\Delta u) \, |F_I(\Delta u)|^2 = |(AG) \bullet (AG)(\Delta u)|^2 + S^2(\Delta u) \, |\Gamma_0(\Delta u)|^2$$

$$+ \left[(AG) \bullet (AG)(\Delta u)\right]^* \, S(\Delta u) \, \Gamma_0(\Delta u) + c.c. \qquad (4-29)$$

Inserting this into Eq. (4-28) yields

$$\langle A(u_1) \, |F_n(u_1)|^2 \, A(u_2) \, |F_n(u_2)|^2 \rangle_{ns}$$

$$= (A \, \langle |F_n|^2 \rangle_n) \bullet (A \, \langle |F_n|^2 \rangle_n)(\Delta u)$$

$$+ S(\Delta u) \, |F_I(\Delta u)|^2 - S^{-1}(\Delta u) \, |(AG) \bullet (AG)(\Delta u)|^2 \qquad (4-30)$$

where we define

$$
S^{-1}(\Delta u) = \begin{cases} 1/S(\Delta u) & , \quad S(\Delta u) > 0 \\ 0 & , \quad S(\Delta u) = 0 \end{cases} \tag{4-31}
$$

As in conventional correlography, Eq. (4-30) relates the ensemble and spatially averaged aperture-plane intensities to the sum of an OTF-weighted power spectrum of the incoherent (mixed) object and the square of the average intensity (or more precisely, the autocorrelation of the ensemble averaged intensity). However, the deterministic component does not add to the bias in the same way as the diffuse component, requiring the subtraction of the additional (the last) term in Eq. (4-30).

$|G_n(u)|^2$ can be determined as follows. For $u_2 = u_1 = u$ ($\Delta u = 0$), Eq. (4-25) gives

$$
\langle |F_n(u)|^4 \rangle_n = (\langle |F_n(u)|^2 \rangle_n)^2 + \Gamma_D^2(0) + 2|G(u)|^2 \, \Gamma_D(0) \tag{4-32}
$$

where we have used the fact that $\Gamma_D(0)$ is real valued. Eqs. (4-26) and (4-32) constitute a set of two simultaneous equations in two unknowns, $|G(u)|^2$ and $\Gamma_D(0)$. Their solution yields

$$
|G(u)|^4 = 2(\langle |F_n(u)|^2 \rangle_n)^2 - \langle |F_n(u)|^4 \rangle_n \tag{4-33}
$$

and

$$
\begin{aligned}
\Gamma_D(0) &= \langle |F_n(u)|^2 \rangle_n - |G(u)|^2 \\
&= \langle |F_n(u)|^2 \rangle_n - \sqrt{2(\langle |F_n(u)|^2 \rangle_n)^2 - \langle |F_n(u)|^4 \rangle_n} \quad . \tag{4-34}
\end{aligned}
$$

71

For a complete solution of $|F_I(\Delta u)|^2$ from Eq. (4-30), one must determine the last term in Eq. (4-30) from the data, a task yet to be accomplished.

Note that for $G(u) = 0$ (i.e., no deterministic component), Eq. (4-30) reduces to the conventional correlography result, and for $D_n(u) = 0$ (i.e., only a deterministic component), the last two terms (the interesting ones) in Eq. (4-30) cancel, leaving a useless equality.

Single-glint case.

Now consider the specific case for which the deterministic component of the object is a single delta function (a glint or corner reflector):

$$g(x) = b \, \delta(x - x_0) \quad . \tag{4-35}$$

Then we have

$$G(u) = b \, \exp(-i2\pi u x_0) \quad , \tag{4-36}$$

$$\left.\begin{array}{c} <|\hat{f}_n(x)|^2>_n \\ f_I(x) \end{array}\right\} = |b|^2 \, \delta(x - x_0) + d_I(x) \quad , \tag{4-37}$$

$$F_I(\Delta u) = |b|^2 \exp(-i2\pi \, \Delta u \, x_0) + \Gamma_D(\Delta u) \quad , \tag{4-38}$$

$$|F_I(\Delta u)|^2 = |b|^4 + |\Gamma_D(\Delta u)|^2$$

$$+ |b|^2 \exp(i2\pi \, \Delta u \, x_0) \, \Gamma_D(\Delta u) + c.c. \quad , \tag{4-39}$$

72

$$\langle |F_n(u)|^2 \rangle_n = |b|^2 + \langle |D_n(u)|^2 \rangle_n = |b|^2 + \Gamma_D(0)$$

$$\equiv \langle |F_n|^2 \rangle_n \qquad (4\text{-}40)$$

and

$$\langle |F_n(u)|^4 \rangle_n = |b|^4 + 4|b|^2 \Gamma_D(0) + 2\Gamma_D^2(0)$$

$$\equiv \langle |F_n|^4 \rangle \qquad (4\text{-}41)$$

the latter two equations being independent of u. For this object, Eq. (4-30) becomes

$$\langle A(u_1) |F_n(u_1)|^2 A(u_2) |F_n(u_2)|^2 \rangle_{ns}$$

$$= S(\Delta u) \left[(\langle |F_n|^2 \rangle_n)^2 + |F_I(\Delta u)|^2 - |b|^4 \right]$$

$$= S(\Delta u) \left[|F_I(\Delta u)|^2 - (\langle |F_n|^2 \rangle_n)^2 + \langle |F_n|^4 \rangle_n \right] \qquad (4\text{-}42)$$

where we used, from Eq. (4-33),

$$|b|^4 = |G(u)|^4 = 2(\langle |F_n|^2 \rangle_n)^2 - \langle |F_n|^4 \rangle_n . \qquad (4\text{-}43)$$

Therefore we can solve for $|F_I(\Delta u)|^2$ for this object in terms of measurable quantities:

$$S(\Delta u) |F_I(\Delta u)|^2 = \langle A(u_1) |F_n(u_1)|^2 A(u_2) |F_n(u_2)|^2 \rangle_{ns}$$

$$+ S(\Delta u) \left[(\langle |F_n|^2 \rangle_n)^2 - \langle |F_n|^4 \rangle_n \right]$$

$$= \langle A(u_1) |F_n(u_1)|^2 A(u_2) |F_n(u_2)|^2 \rangle_{ns} - S(\Delta u) \, \text{Var}_n(|F_n|^2) .$$

$$(4\text{-}44)$$

where $\text{Var}_n(|F_n|^2)$ is the variance over the ensemble of intensity realizations. The incoherent image of this type of mixed object can be reconstructed from Eq. (4-44) via phase retrieval with the help of a nonnegativity constraint.

Note that this differs from the usual $I_1 I_2 - \overline{I}^2$ averaging done for the case of a diffuse object only. In that style of notation, Eq. (4-44) is equivalent to

$$|F_I(\Delta u)|^2 = \langle I_1 I_2 - \overline{I^2} + \overline{I}^2 \rangle . \tag{4-45}$$

Since for a fully-developed speckle pattern

$$\overline{I_D^2} = 2\overline{I}_D^2 \tag{4-46}$$

this estimator is equivalent to

$$|F_I(\Delta u)|^2 = \langle I_1 I_2 - 2\overline{I}^2 + \overline{I}^2 \rangle = \langle I_1 I_2 - \overline{I}^2 \rangle \tag{4-47}$$

for the case of $G(u) = 0$. That is, the estimator of Eqs. (4-44) and (4-45) gives the correct result whether there ' a single glint or no glint, whereas the other estimators, such as $I_1 I_2 - \overline{I}^2$ give the wrong answer if there is a single deterministic glint. The presence of a glint can be detected by computing Eq. (4-43).

Notice that ensemble averaging alone and ensemble averaging followed by spatial averaging yields useful information. However, we were unable to find useful information in spatial averaging alone for

the case of a mixed object. (And spatial averaging followed by ensemble averaging is equivalent to ensemble averaging followed by spatial averaging: $\langle\langle\bullet\rangle_n\rangle_s = \langle\langle\bullet\rangle_s\rangle_n$ for the quantities analyzed.)

This type of image formation would be unaffected by atmospheric turbulence as long as nonisoplanatism and scintillation are not present since only aperture-plane intensities are measured. However, atmospheric turbulence would severely limit conventional coherent imaging or heterodyne interferometry.

5.0 COHERENT IMAGE RECONSTRUCTION FOR OBJECTS HAVING GLINTS

5.1 INTRODUCTION

Ordinarily when we image a space object with a large-aperture earth-bound optical imaging sensor, the resolution is very poor owing to phase aberrations caused by the turbulent atmosphere. An approach to circumvent this problem, initially studied over a decade ago, is laser correlography [5.1]. It involves the illumination of the space object by a coherent laser and the detection of the backscattered intensity pattern in the aperture plane. This speckled intensity pattern is the squared modulus of the Fourier transform of the complex-valued object reflectivity. Ordinarily this allows only an autocorrelation of the object, not an image of the object, to be computed.

For certain favorable object geometries, such as objects having separated parts, an iterative Fourier transform algorithm has been developed that retrieves the phase of the Fourier transform of the object and thereby permits a diffraction-limited complex-valued image to be reconstructed [5.2]. Unfortunately the class of objects for which this approach currently works is too limited. An approach that works for general objects is that of imaging correlography [5.3] described in Section 3. By averaging over the autocorrelations of many aperture-plane speckle intensity patterns, one arrives at the modulus of the Fourier transform of the incoherent object (the object had it been illuminated by an incoherent source such as the sun). In this case the ideal image is real-valued and nonnegative, and an image of a general object can be reconstructed from the Fourier modulus data using the iterative transform algorithm employing the powerful nonnegativity constraint. This concept has recently been verified in laboratory simulations [5.4]. Unfortunately in many circumstances it may be impractical to collect a large enough number of snapshots of aperture-plane speckle patterns to arrive at a good statistical estimate of the

incoherent Fourier modulus. For this reason it is of great interest to be able to reconstruct a coherent image from a single snapshot of data, despite the difficulty mentioned at the beginning of this paragraph.

It has been observed that satellites frequently have strong glint returns (mirror-like reflections off solar panels, for example). It has long been known that if there is a single glint sufficiently separated from the rest of the object, then by the holographic method [5.5] one can easily reconstruct a coherent image from a single snapshot of data. However, such ideal glints would be relatively uncommon. Glints centered on the object or multiple glints would prevent the use of the holographic approach.

In this section we describe methods developed for reconstructing an image having glints from a single realization of the intensity of the aperture-plane speckle pattern from a coherently illuminated object. In Section 5.2 the most successful method we developed is described. It consists of three successivel algorithms. In Section 5.2 is shown reconstructions using just the iterative transform algorithm. A recursive reconstruction algorithm that gave limited success is described in Section 5.3. In Section 5.4 the effect of a large glint on the quantization error of the measured data is analyzed.

5.2 THREE-ALGORITHM METHOD

In what follows, we describe an approach that permits a high-fidelity image to be reconstructed from a single snapshot of aperture-plane intensity data for the case of nonholographic multiple glints located on the object. The approach consists of three algorithms employed successively. The first algorithm reconstructs the glints only, both their positions and their complex values. It involves the triple intersection of translates of the autocorrelation function. The second algorithm uses the reconstructed glints along with the aperture-plane intensity data to arrive at a partially reconstructed coherent

image of the entire object. It is modification of the ΔF-synthesis algorithm in x-ray crystallography. The third algorithm completes the reconstruction of a high-fidelity image using information about the support or size of the object. It is the same iterative Fourier transform algorithm that previously had only been effective for special classes of coherent objects; however, it is effective for general objects having glints that are partially reconstructed by the first two algorithms.

In the subsections that follow, we briefly describe each of the three algorithms that make up the imaging approach and show reconstruction results.

5.2.1 Reconstruction of Glints

In what follows we assume that the object consists of both a glint (or multiple glints) component $g(x)$, and a diffuse extended component, $d(x)$,

$$f(x) = g(x) + d(x) \qquad (5-1)$$

where x is a 2-D coordinate. It is assumed that the Fourier intensity, $|F(u)|^2$, is detected, where $F(u)$, $G(u)$ and $D(u)$ are the Fourier transforms of $f(x)$, $g(x)$ and $d(x)$, respectively. From the Fourier intensity we can compute the object's autocorrelation

$$r_f(x) = [g(x) + d(x)] \circledast [g(x) + d(x)] = \mathcal{F}^{-1}[|F(u)|^2]$$

$$= g(x) \circledast g(x) + d(x) \circledast d(x) + g(x) \circledast d(x) + d(x) \circledast g(x)$$

$$= r_g(x) + r_d(x) + g(x) \circledast d(x) + d(x) \circledast g(-x) \qquad (5-2)$$

where $\mathcal{F}$ denotes Fourier transformation, $\circledast$ denotes cross-correlation, and r_f denotes the autocorrelation of f.

79

If the glint energy is large compared with the energy of the diffuse component, i.e. if

$$K = \frac{\sum\limits_{x} |g(x)|^2}{\sum\limits_{x} |d(x)|^2} \qquad (5\text{-}3)$$

is on the order of one or greater, than the peaks of $r_g(x)$, the autocorrelation of the glints, will exceed the other terms in Eq. (5-2), enabling the glint information to be isolated from the other terms by a thresholding operation (set all values below some threshold to zero). Once $r_g(x)$ is isolated, then the glints can be reconstructed as described below.

We model the glints by

$$g(x) = \sum_{m=1}^{M} g_m \, b(x - x_m) \qquad (5\text{-}4)$$

where M is the number of glints and $b(x)$ is the impulse response of the imaging system [or is a delta function if $g(x)$ represents the object]. The autocorrelation of the glints is given by

$$r_g(x) = g(x) \bullet g(x)$$

$$= \sum_{m=1}^{M} \sum_{n=1}^{M} g_m g_n^* \, b(x - x_m + x_n) \qquad (5\text{-}5)$$

If the glints are spaced nonredundantly, that is if no two vector separations between distinct pairs of glints is the same, then

$$r_g(x_j - x_k) \simeq f_j f_k^* \, b(0) = f_j f_k^* \qquad (5\text{-}6)$$

where for mathematical simplicity we have normalized so that $b(0) = 1$. Eq. (5-6), which embodies the fact that each glint in the autocorrelation arises from the product of two glint values in the object, allows the autocorrelation of the glints to be unraveled. This unraveling can be done in a number of ways, as described in Reference 5.6, Sections 5 to 7. The method we used is a modification of one of the methods to which Ref. 5.6 alludes. It consists of the following steps.

1. To find the glints in $r_f(x)$ that constitute $r_g(x)$, threshold $|r_f(x)|^2$ to define an autocorrelation support function for $r_g(x)$:

$$r_s(x) = \begin{cases} 1, & \text{where } |r_f(x)|^2 \geq \text{threshold} \\ 0, & \text{otherwise} \end{cases} \qquad (5\text{-}7)$$

Then we assume that $r_g(x) \simeq r_s(x) r_f(x)$ except at $x=0$ where $r_d(x)$ corrupts it.

2. Reconstruct the support of the object glints using the autocorrelation support tri-intersection [5.6]

$$r_{s1}(x) = r_s(x) \, r_s(x - x_{max1}) \, r_s(x - x_{maxk}) \qquad (5\text{-}8)$$

where x_{max1} is the location of the maximum of $|r_g(x)|$ outside $x=0$, and x_{maxk} is the location of the maximum of $|r_g(x)|r_s(x)r_s(x-x_{max1})$ outside $x=0$ and $x=x_{max1}$.

3. Multiply $r_{s1}(x)$ by $r_g(x)$, which can be shown to yield either

$$r_{s1}(x) \, r_g(x) = \sum_m |g_m|^2 \, b(x) + g_k^* \sum_{m \neq k} g_m \, b(x - x_m + x_k) \qquad (5\text{-}9a)$$

31

or

$$\bullet \sum_m |g_m|^2 \, b(x) \, g_k \sum_{n \neq k} g_n^* \, b(x - x_k + x_n) \qquad (5\text{-}9b)$$

4. Using a second support function, determine $|g_k|$, which is the value at $x=0$, by the method described in Section 5.1.5. This procedure is required because $r_g(x)$ is corrupted at $x=0$ by $r_d(x)$.

5. Divide Eq. (5-9) by $g_k = |g_k|$ to get

$$\text{glint image} = \sum_{m \neq k} g_m \, b(x - x_m + x_k) \qquad (5\text{-}10a)$$

or

$$\bullet \sum_{n \neq k} g_n^* \, b(x - x_k + x_n) \qquad (5\text{-}10b)$$

where (5-10a) represents an image of the glints (except g_k, which was already reconstructed) and (5-10b) represents a twin (complex conjugated and rotated $180°$) image of the glints. Either is an admissible solution when only the autocorrelation or the Fourier intensity is given.

This process of reconstructing the glints is illustrated in Figure 5-1. The object, in Fig. 5-1(a) is a complex-valued, speckled image of a model of a P72-2 satellite (the diffuse part) with three delta-function glints artificially added on the middle part of the body of the satellite. Previously this was thought to be the most difficult case for imaging using glints. (For a holographic reconstruction there must be only one glint, and it must be separated from the body of the satellite.) In this and all the figures, the modulus of the complex-valued images are shown. Figure 5-1(b) shows the autocorrelation function computed from noise-free Fourier intensity data. Figure 5-1(c) shows the results of thresholding the autocorrelation function $r_f(x)$ to isolate $r_g(x)$, the autocorrelation of the glints. $M = 3$
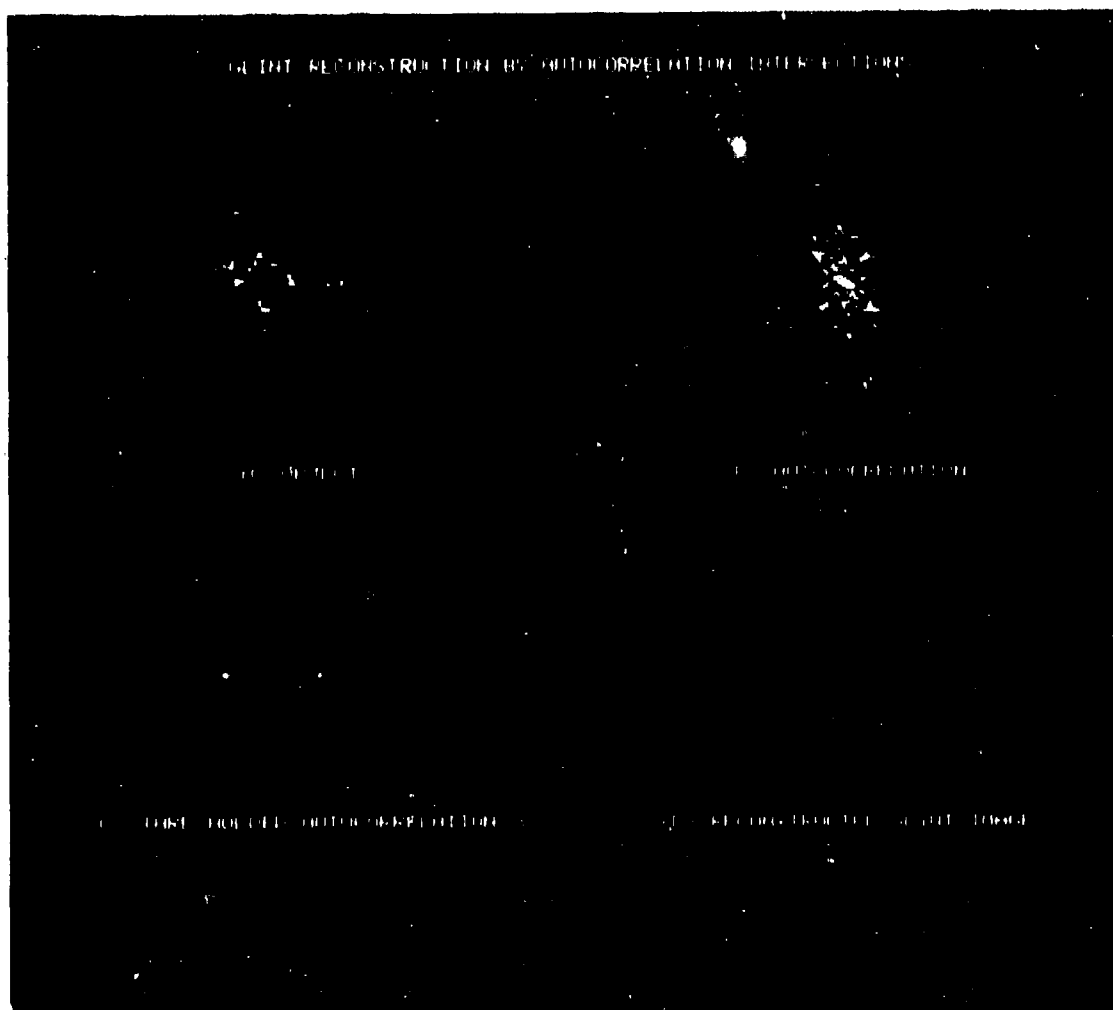
82

FIGURE 5-1. RECONSTRUCTION OF THE GLINT COMPONENT OF THE OBJECT. (A) The object having 3 glints; (B) its autocorrelation; (C) thresholded autocorrelation; (4) glint component of the image reconstructed from (B) and (C).

glints in the object produces $M^2-M+1 = 7$ glints in $r_g(x)$. The five-step procedure described above was then used to successfully reconstruct the glints alone, shown in Figure 5-1(d).

This experiment was repeated for several different values of the K-ratio, as defined by Eq. (5-3). The normalized root-mean-squared (NRMS) error of the glint reconstructions is plotted in Figure 5-2 for two different cases: the three glints positioned on the body of the satellite as described above, and the same three glints positioned just off the body of the satellite. The positions of the glints with respect to the satellite body made little difference. The glints were reconstructed accurately (NRMS error < 0.20) for $K \geq 1.0$.

The examples described above were obtained with a simulated object using simplified delta-function glints. For the case of realistic diffraction-limited glints (being impulse responses spread over more than one pixel), a modification of the first step of the 5-step procedure is required. It involves finding the glints in the autocorrelation by a process related to the CLEAN method from radio astronomy rather than by simple thresholding.

At this point there are several possible approaches to using the reconstructed glint information, $g(x)$, to help to reconstruct the entire object, $f(x)$. In what follows we describe only one of the approaches, the one that appeared to be most effective: first obtain a partial reconstruction by ΔF-synthesis, then complete the reconstruction by the iterative transform algorithm.

5.2.2 ΔF Synthesis Algorithm

ΔF Synthesis is a method taken from x-ray crystallographic reconstruction, adapted by Baldwin and Warner for interferometric astronomical imaging [5.7] and further adapted here for coherent reconstruction when glints are known. It works poorly when little
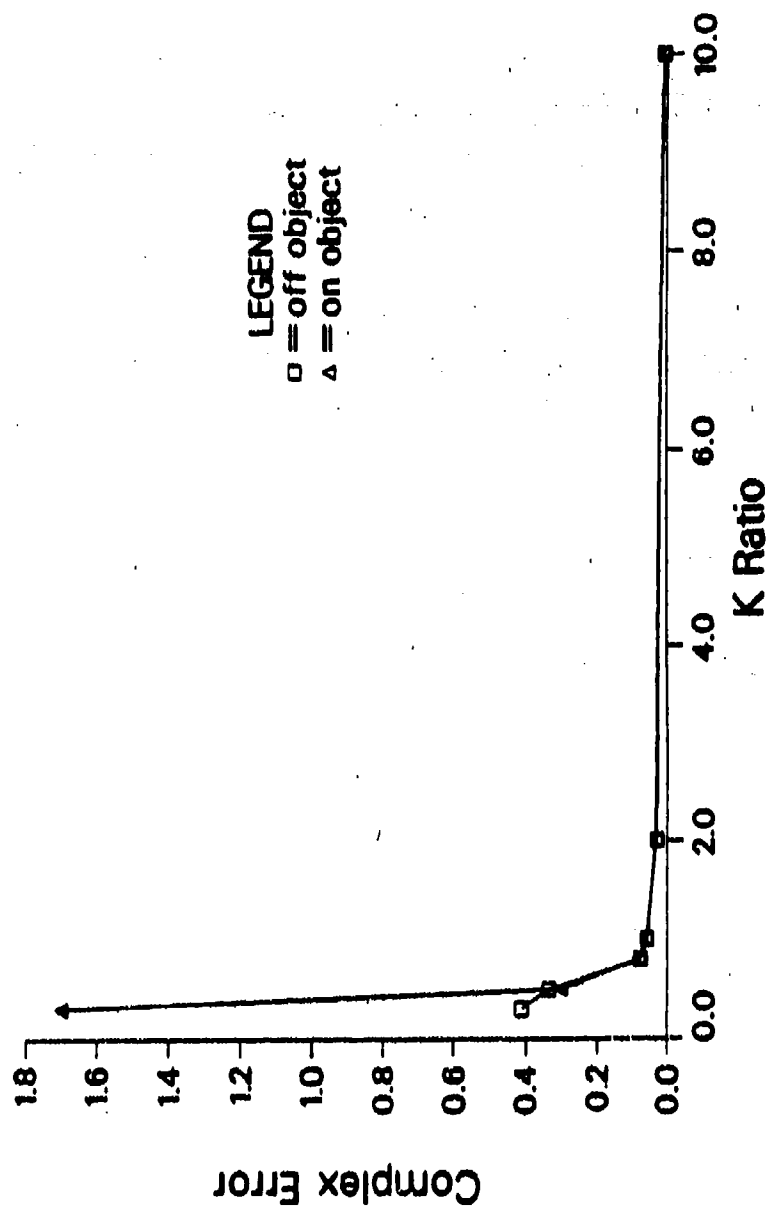
84

Complex Glint Reconstruction Error

FIGURE 5-2. ERROR IN RECONSTRUCTING GLINTS AS A FUNCTION OF RELATIVE GLINT ENERGY. The error is the normalized RMS error of the complex (modulus and phase) reconstructed glints for two different positions of the glint component.

85

about the image is known, but works well when parts of the image are known well. This is the case if the glints are reconstructed as described in the previous section.

One iteration of ΔF synthesis is as follows. At the nth iteration we assume we know some part $g_n(x)$, of the image, where

$$f(x) = g_n(x) + d_n(x) \tag{5-11}$$

and $d_n(x)$ is the unknown part of the image. For the first iteration $g_1(x)$ is the image of the glints reconstructed by the method described in the previous section and $d_1(x)$ is the (unknown) diffuse part of the object. The modulus squared of the Fourier transform of Eq. (5-11) is

$$|F(u)|^2 = |G_n(u)|^2 + G_n^*(u) \, D_n(u) + G_n(u) \, D_n^*(u) + |D_n(u)|^2 \quad . \tag{5-12}$$

Taking the Fourier transform, $G_n(u)$, of $g_n(x)$ and multiplying it by $|F(u)|/|G_n(u)|$ yields

$$
\begin{aligned}
G_n^{'} &= G_n \; |F|/|G_n| \\
&= \left[|G_n|^2 + G_n^* D_n + G_n D_n^* + |D_n|^2 \right]^{1/2} G_n/|G_n| \quad . \\
&\simeq G_n + D/2 + \left(G_n \; |D_n|^2 + G_n^2 D_n^* \right)/\left(2|G_n|^2 \right) \quad . \tag{5-13}
\end{aligned}
$$

using a Taylor-series expansion assuming $|G_n|$ large. Therefore

$$2G_n^{'} - G_n \simeq \underbrace{G_n + D_n}_{F} + \left(G_n \; |D|^2 + G_n^2 D_n^* \right)/|G_n|^2 \quad . \tag{5-14}$$

Inverse Fourier transforming yields

$$2g_n'(x) - g_n(x) = f(x) + \text{other terms.} \qquad (5\text{-}15)$$

That is, by subtracting the input image, $g_n(x)$, from twice the output image, $g_n'(x)$, we reconstruct the entire image, $f(x)$. However, the "other terms" severely corrupt much of the desired image. Nevertheless, the brightest points in Eq. (5-15) outside the previously known image points, $g_n(x)$, are most likely to belong to the object, $f(x)$, rather than to the other terms. Thus we take the brightest new points resulting from the computation of Eq. (5-15) and add those to $g_n(x)$ to form $g_{n+1}(x)$ which represents a larger known portion of the image. This is done repeatedly until a reasonably complete partially-reconstructed image appears.

Figure 5-3 shows the results of the application of ΔF synthesis. Figure 5-3(a) shows the same coherent object with three glints on the body, and Figure 5-3(b) shows the same reconstructed glints as for Figure 5-1. (Any difference in appearance from Figure 5-1 is due to a difference in exposures when photographing the images.) Using the reconstructed glints as $g_1(x)$, Eq. (5-15) was computed, the result of which is shown in Figure 5-3(c). Much of the object is apparent in Figure 5-3(c), but there is a high level of artifacts. Figure 5-3(d) shows the improved results after 12 iterations of ΔF synthesis. The locations of the points assumed to be known at this stage are shown in Figure 5-3(e). Further iterations of ΔF synthesis resulted in little further improvement.

5.2.3 Iterative Fourier Transform Algorithm

The iterative Fourier transform algorithm involves repeatedly Fourier transforming an estimate back and forth between the Fourier domain, where the measured Fourier intensity is reinforced, and the
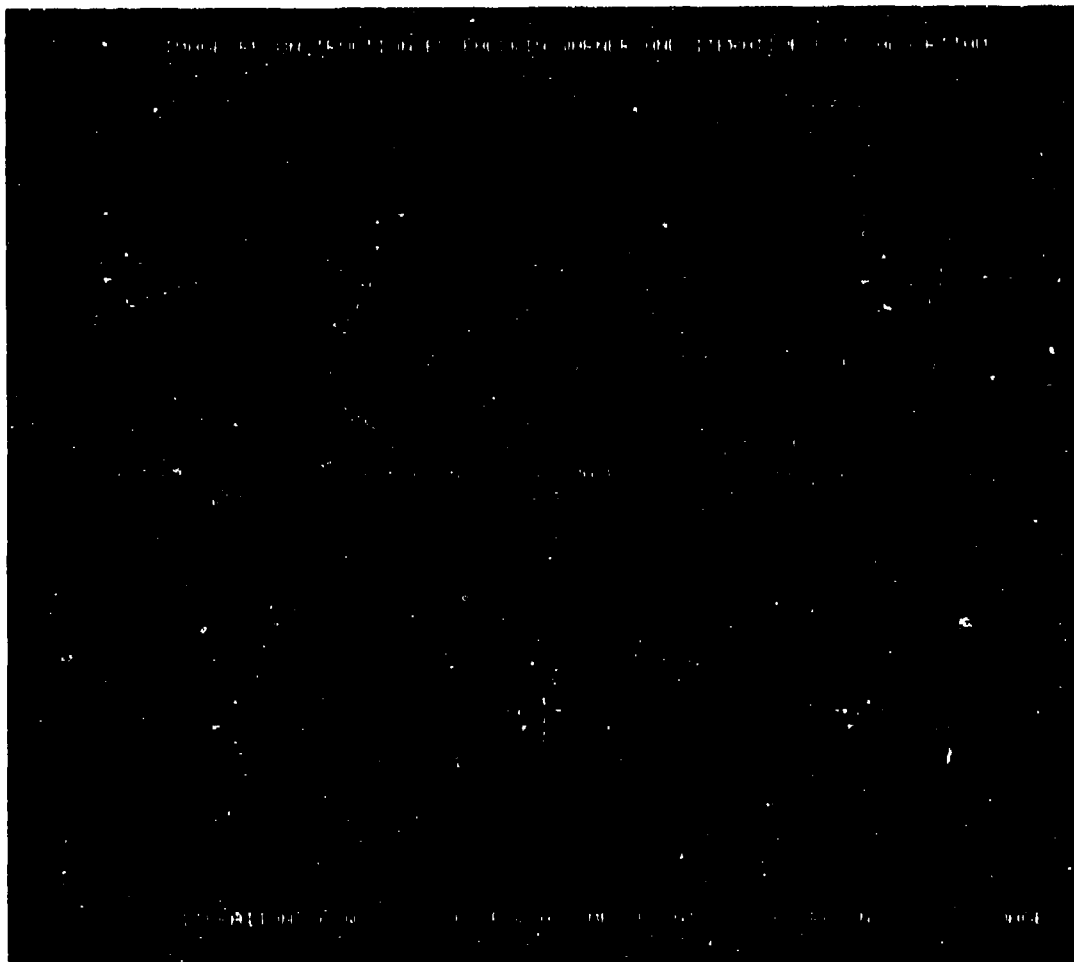
FIGURE 5-3. IMAGE RECONSTRUCTION BY THE THREE-ALGORITHM METHOD. (A) The object; (B) the reconstructed glints (from Figure 5-1); (C) output from one iteration of ΔF synthesis; (D) output from 12 iterations of ΔF synthesis; (E) locations of points assumed to be known in (D); (F) image reconstructed by the iterative transform algorithm staring with (D).

image domain, where a support constraint is enforced. The support constraint, i.e. knowledge that the image is zero outside some well-defined area, can be derived from the autocorrelation of the object [5.6]. The details of the iterative Fourier transform algorithm are described elsewhere [5.2,5.8,5.9]. The partially reconstructed image shown in Figure 5-3(d) was used as an input to the iterative Fourier transform algorithm for which we employed a supports constraint in the form of a crude rectangle inside of which the object loosely fit. The image reconstructed by the iterative Fourier transform algorithm is shown in Figure 5-3(f). It is an excellent reconstruction of the object shown in Figure 5-3(a), despite having assumed total loss of phase information and despite the fact that the glints were in the most unfavorable locations. (Prior to this work it was thought that multiple glints imbedded within the object would be the most difficult case.)

This experiment was repeated for several K-ratios (glint energies), and the results are shown in Figure 5-4 and plotted in Figure 5-5. Very recognizable images were reconstructed for $K \geq 2$ (image NRMS error ≤ 0.35). For $K = 5$, the simulation experiment was repeated for various levels of photon noise in the intensity data. The results are shown in Figure 5-6 and plotted in Figure 5-7. Recognizable images were reconstructed for 10^7 or greater photons per intensity array of 128 x 128 samples (or about 60 x 40 = 3200 speckles), equivalent to about 600 photons per sample or 4000 photons per speckle.

5.2.4 Summary of the Three-Algorithm Method

Prior to this work, coherent image reconstruction from a single snapshot of far-field laser speckle intensity data was possible if the object included a single well-separated (holographic) glint or a very bright glint beyond the edge of the diffuse part of the object. We have developed an approach for reconstructing objects having much less favorable glints, including multiple glints that may be located within
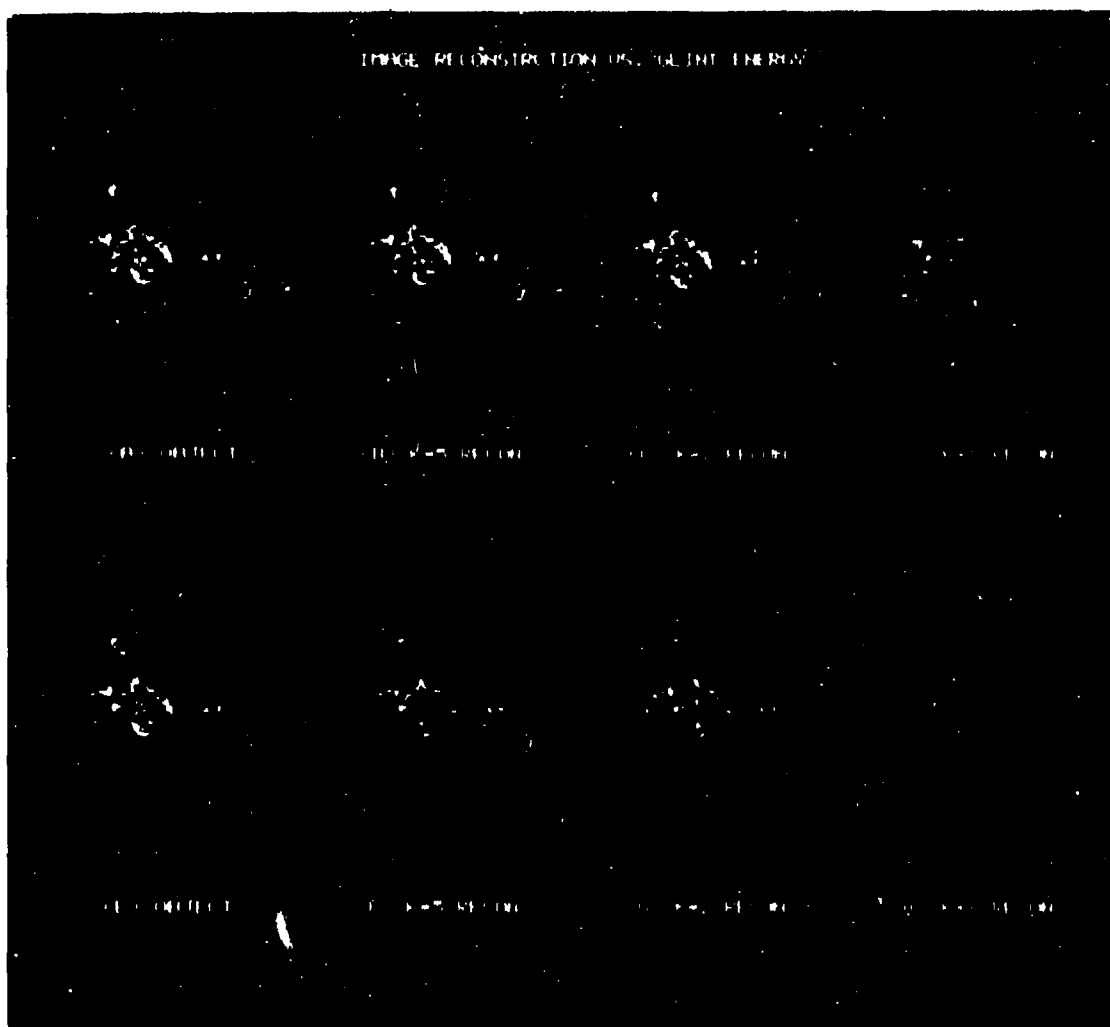
FIGURE 5-4. IMAGES RECONSTRUCTED BY THE THREE-ALGORITHM METHOD FOR VARIOUS GLINT ENERGIES (K-RATIOS). (A)-(D) Three glints off the object, (E)-(H) three glints on the object.

FIGURE 5-5. NORMALIZED RMS ERROR IN RECONSTRUCTING THE IMAGE AS A FUNCTION OF K RATIO.
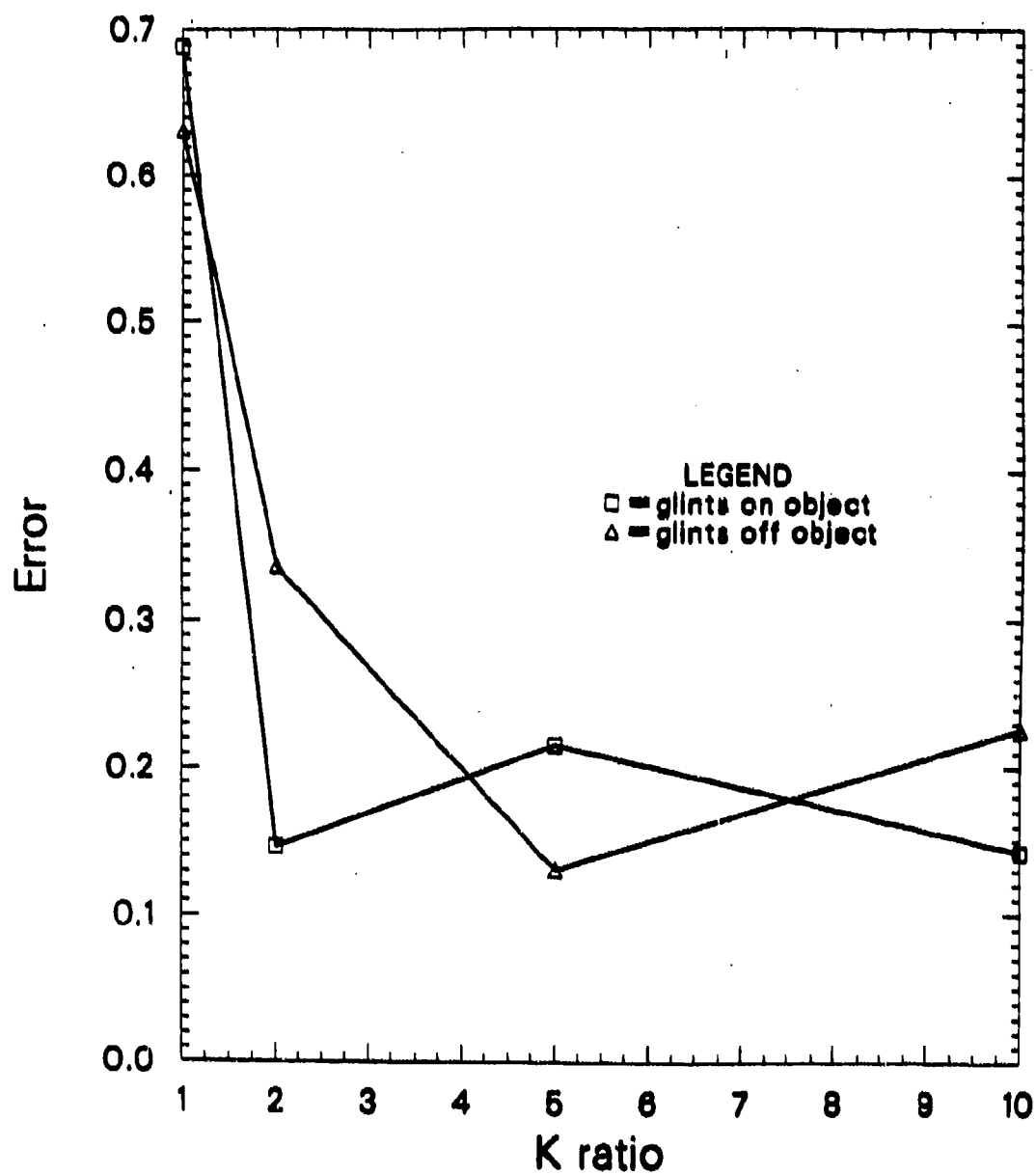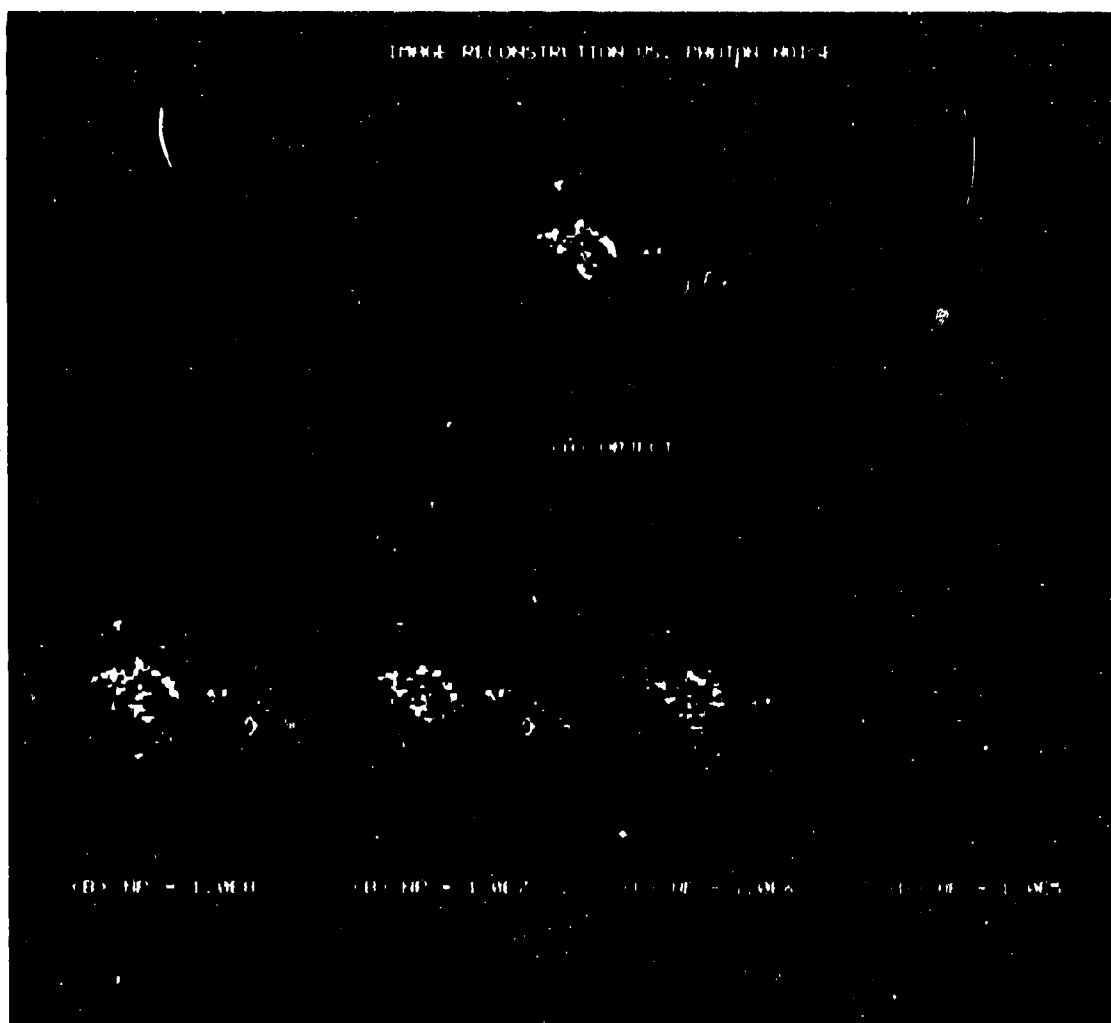
FIGURE 5-6.   IMAGES RECONSTRUCTED BY THE THREE-ALGORITHM METHOD FOR
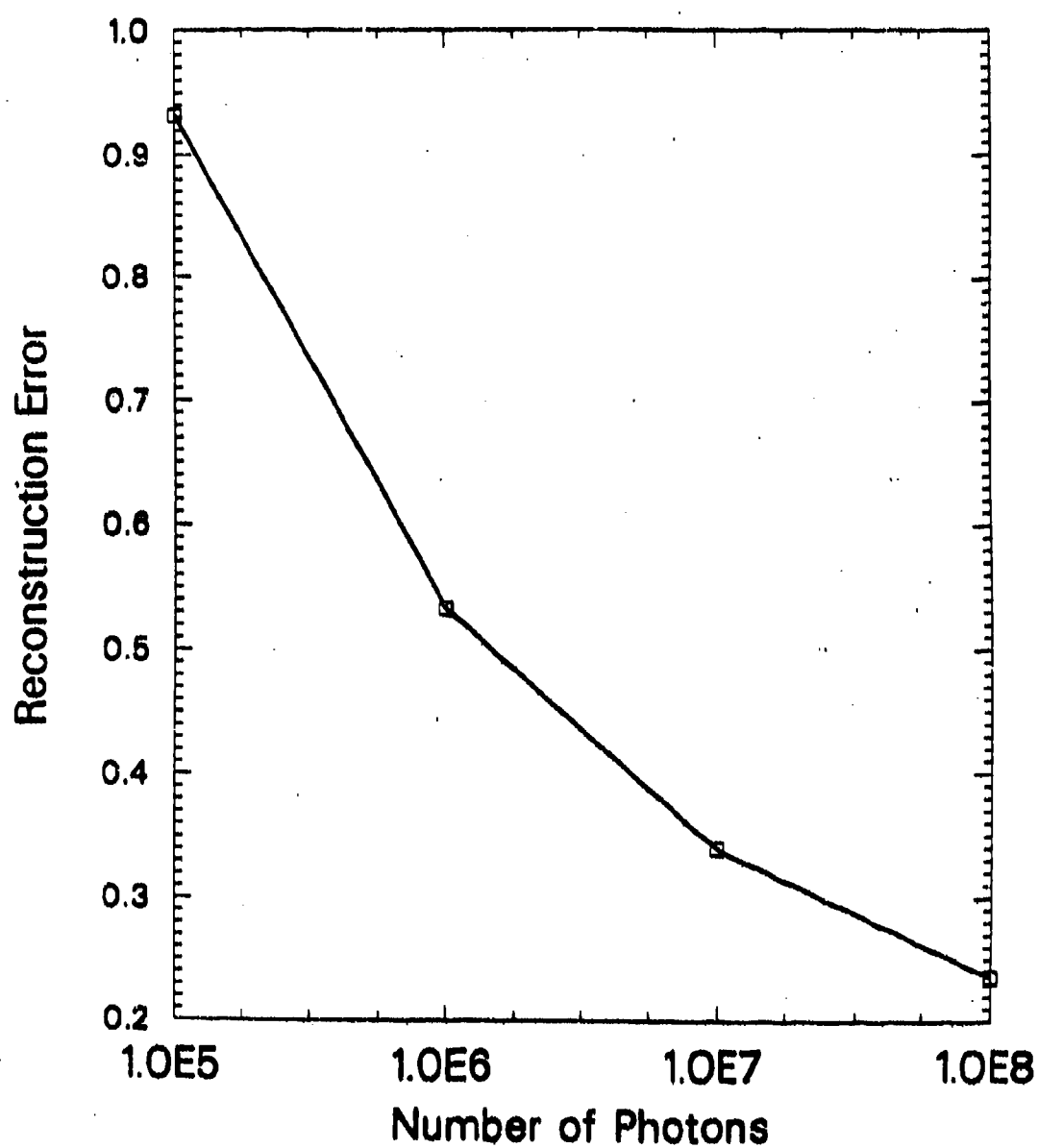VARIOUS PHOTON LEVELS.   K=5 and three glints on object.

FIGURE 5-7. NORMALIZED RMS ERROR VS. NUMBER OF PHOTONS.

the diffuse part of the object. The approach consists of three successive algorithms: (1) a triple intersection of the autocorrelation function that yields an image of the glints alone, (2) the ΔF-synthesis algorithm that uses the image of the glints together with the Fourier intensity data to yield a partial reconstruction of the entire image, and (3) the iterative Fourier transform algorithm that uses the partially reconstructed image together with the Fourier intensity data and a support constraint to complete the reconstruction. For the example investigated having three delta-function glints, good reconstructions were obtained for K = (glint energy)/(diffuse/energy) $\geq$ 2 and 4000 photons per detected speckle (i.e., a relatively high light level).

Further research is required to optimize the approach and to quantify performance for diffraction-limited (as opposed to delta-function) glints, to extend the method to work for extended glints, and to demonstrate the method on laboratory experimental and field data.

5.2.5 Determining $|g_k|$ for Glint Reconstruction

To determine the value of the first glint, $|g_k|$, perform the following steps.

1. Sum over the squared modulus of $r_{s1}(x) r_g(x)$ for $m \neq k$:

$$c_k = |g_k|^2 \sum_{m \neq k} |g_m|^2 = |g_k|^2 \sum_m |g_m|^2 - |g_k|^4 \ . \qquad (5\text{-}16)$$

2. Reconstruct a second image support:

$$r_{s2}(x) = r_s(x) \ r_s(x - x_{max1}) \ r_s(x_{maxj}) \qquad (5\text{-}17)$$

where x_{maxj} is the location of the largest peak of $r_s(x) r_s(x - x_{max1}) r_g(x)$ that is outside $r_{s1}(x)$.

3. As in Step 1, sum over the squared modulus of $r_{s2}r_g(x)$ for $n \neq j$:

$$C_j = |g_j|^2 \sum_{n \neq j} |g_n|^2 = |g_j|^2 \sum_n |g_n|^2 - |g_j|^4 \quad . \tag{5-18}$$

4. Let

$$C_{jk} = r(x_{max1}) = r(x_j - x_k) = g_j g_k^* \quad . \tag{5-19}$$

5. Solve Eqs. (5-16), (5-18) and (5-19) for $|g_k|^2$:

$$|g_k|^2 = |C_{jk}| \left[\frac{C_k - |C_{jk}|^2}{C_j - |C_{jk}|^2} \right]^{1/2} \quad .$$

6. Assume that g_k has zero phase (we can arbitrarily set any one phase value to whatever we want):

$$g_k = \sqrt{|g_k|^2} \quad . \tag{5-20}$$

Note that a simple method is possible if the object had no diffuse part; however, the diffuse part of the object will usually make a strong contribution to $r_f(0)$, making this 5-step method necessary.

5.3 RECONSTRUCTION WITH ONLY THE ITERATIVE TRANSFORM ALGORITHM

Although the three-algorithm method discussed in the previous section is generally the most robust way to reconstruct an object having glints from a single snapshot of Fourier intensity data, it is also possible to reconstruct using only the iterative transform algorithm (the third algorithm). In this case it is assumed that by inspection of the autocorrelation function, computed from the measured

Fourier intensity, we can determine that there are one or more glints in the object. Furthermore, if there are two glints, then the separation of the glints can also be determined from the autocorrelation.

To start the iterative transform algorithm, two different starting estimates were tried. First, since the autocorrelation function contains the desired image as one of its terms (as described in Sect. 5.3), we chose as an initial estimate a windowed version of the autocorrelation function. Second, we chose the initial estimate to be a bright glint (or glints) surrounded by random noise. In practice the latter initial estimate worked better. It was assumed that the approximate location of the glint (or glints) was known.

Figure 5-8 shows reconstruction results for the case of a single bright glint added near the top center of the speckled satellite image. The support constraint, assumed known a priori, was a rectangle just enclosing the object with the glint. A plot of the normalized RMS error of the reconstructed images as a function of the K ratio is shown in Figure 5-9. The reconstructions are very good for K greater than 0.25. These reconstructions are better than those of the previous section because (1) since there is only one glint, that single glint contains all the energy implied by the K ratio, making it relatively brighter than any of the three glints for the previous case, for any given value of K, and (2) reconstruction from three glints is inherently much more difficult than from a single glint. For the cases of K = 1.0 and 0.5, Poisson noise was added to the Fourier intensity data. The errors in the corresponding reconstructed images is shown in Figures 5-10(a) and (b) respectively.

Figure 5-11 shows reconstruction results for the case of a pair of glints, one of which is in the same position as the case above, and the second is nearer to the center of the object. Figure 5-12 shows a plot of the normalized RMS error as a function of glint strength. Very good reconstructions are obtained for K > 0.5.

FIGURE 5-8. IMAGES WITH A SINGLE GLINT RECONSTRUCTED BY THE ITERATIVE
TRANSFORM ALGORITHM, FOR VARIOUS K RATIOS.

FIGURE 5-9. NORMALIZED RMS ERROR VS. K RATIO FOR IMAGES WITH A SINGLE GLINT RECONSTRUCTED BY THE ITERATIVE TRANSFORM ALGORITHM.

(a)

(b)

FIGURE 5-10. NORMALIZED RMS ERROR VS. DATA ERROR FOR IMAGES WITH A SINGLE GLINT RECONSTRUCTED BY THE ITERATIVE TRANSFORM ALGORITHM. (a) For K=1.0; (b) for K=0.5.
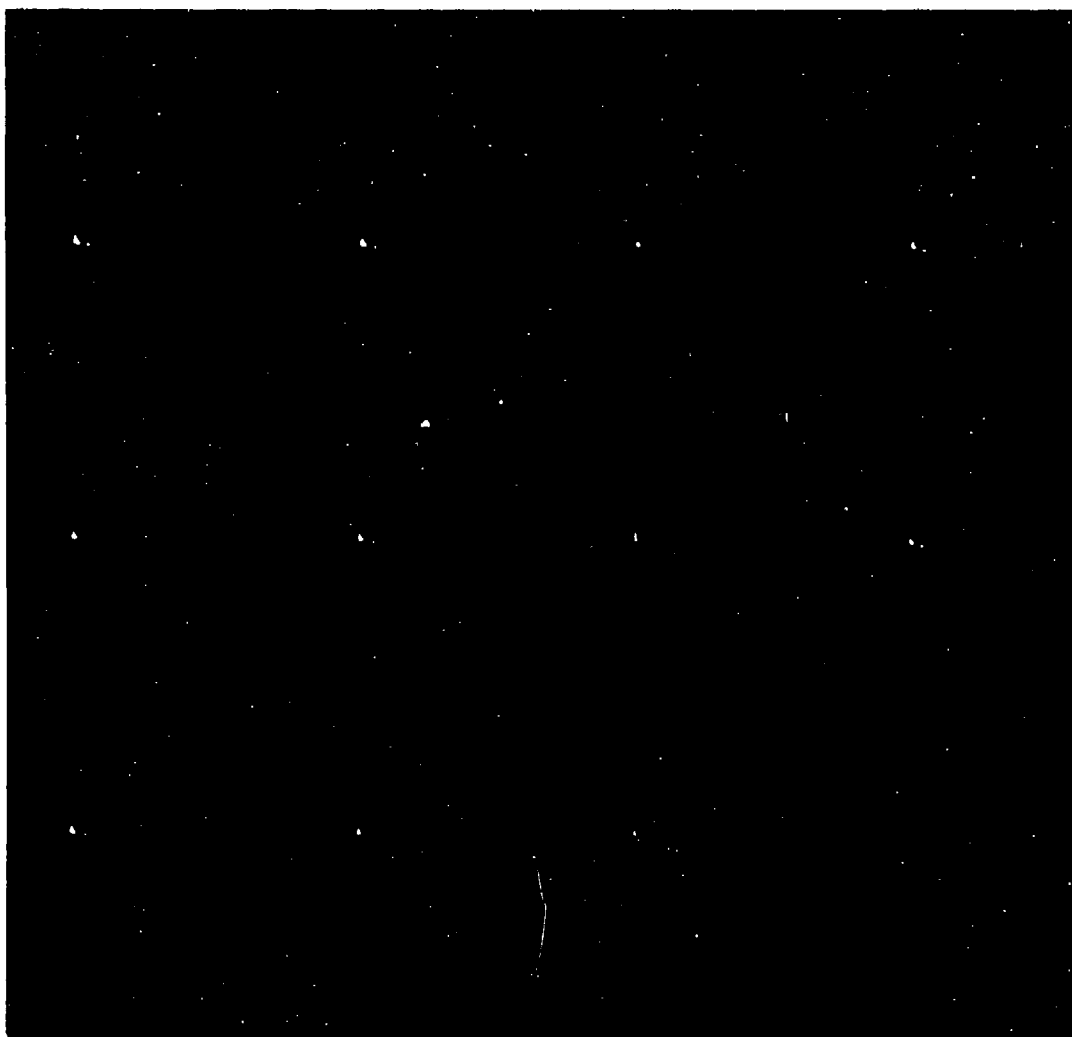
99

FIGURE 5-11. IMAGES WITH TWO GLINTS RECONSTRUCTED BY THE ITERATIVE TRANSFORM ALGORITHM, FOR VARIOUS K RATIOS.

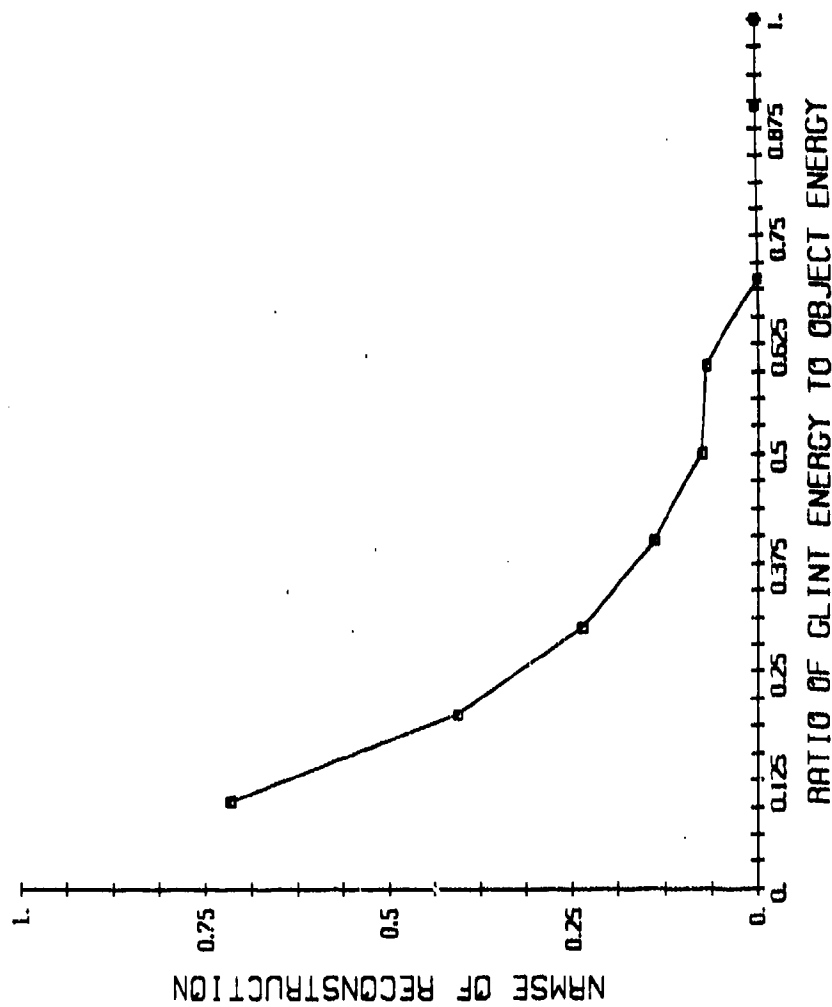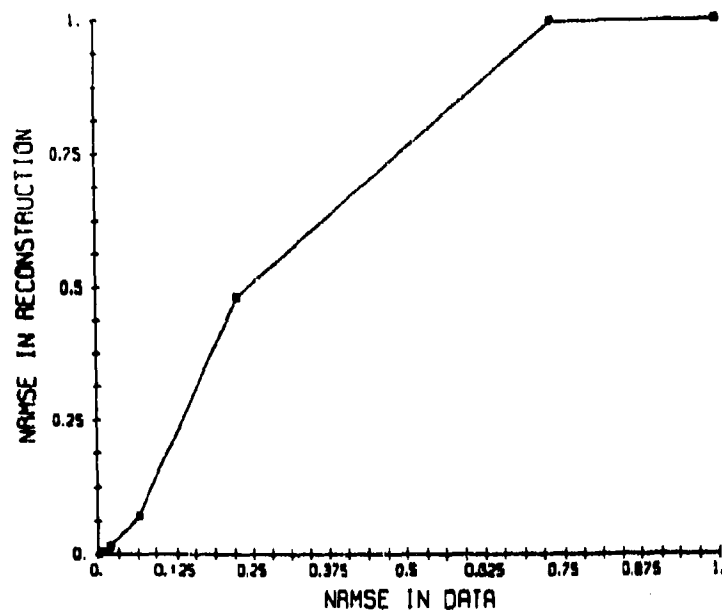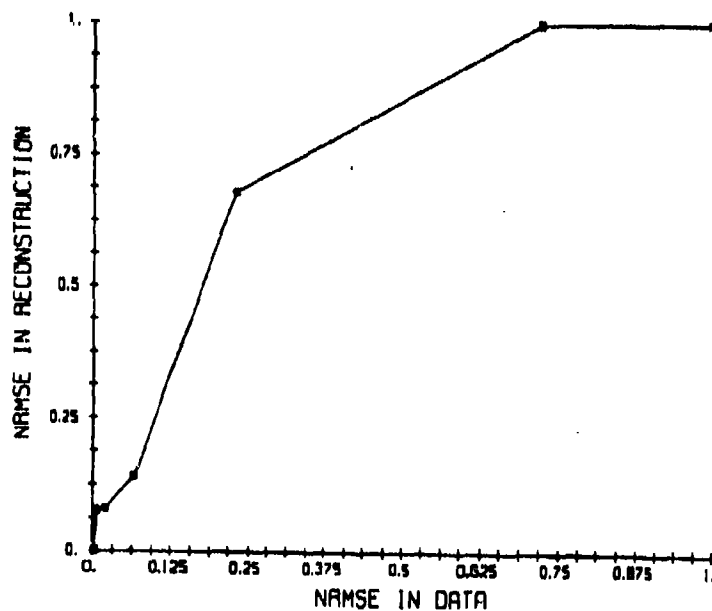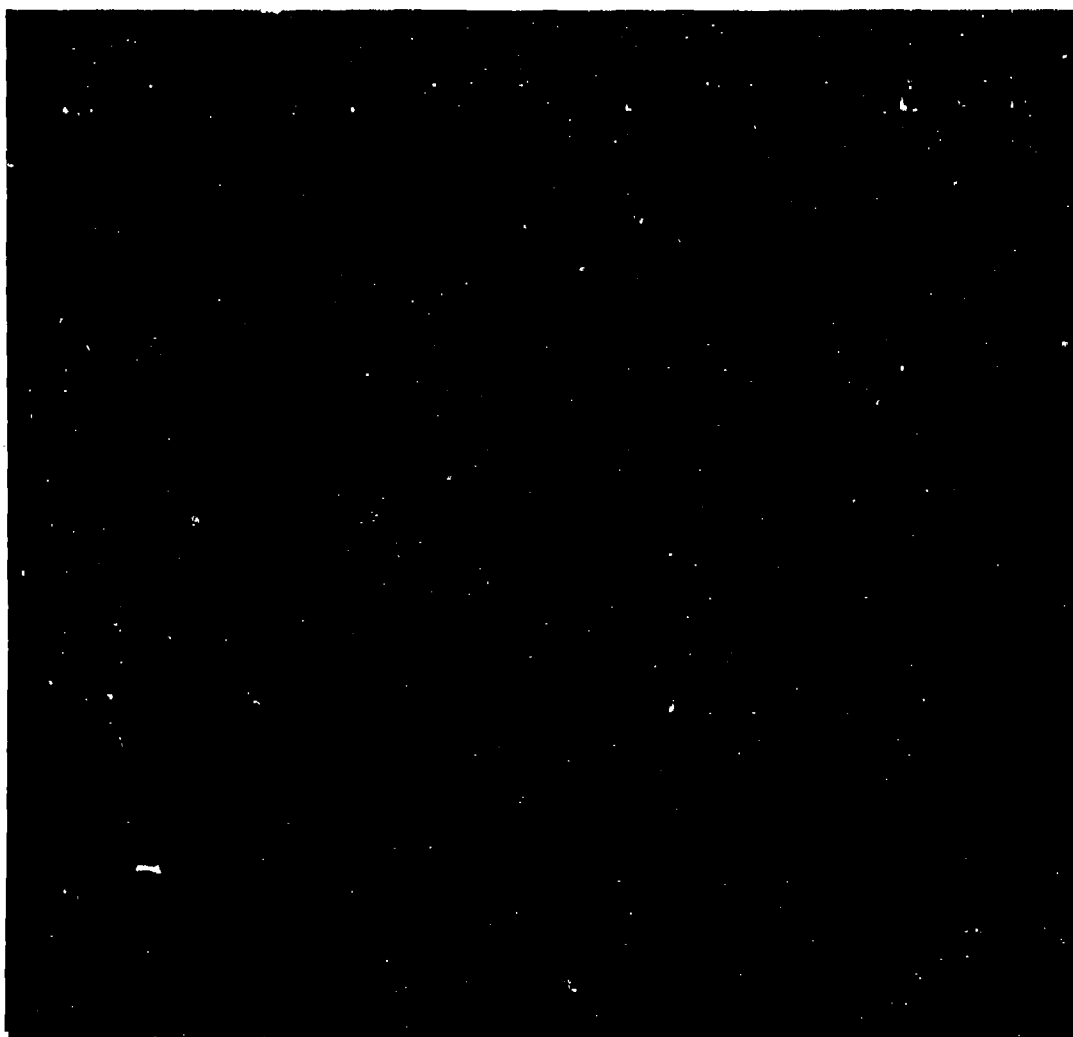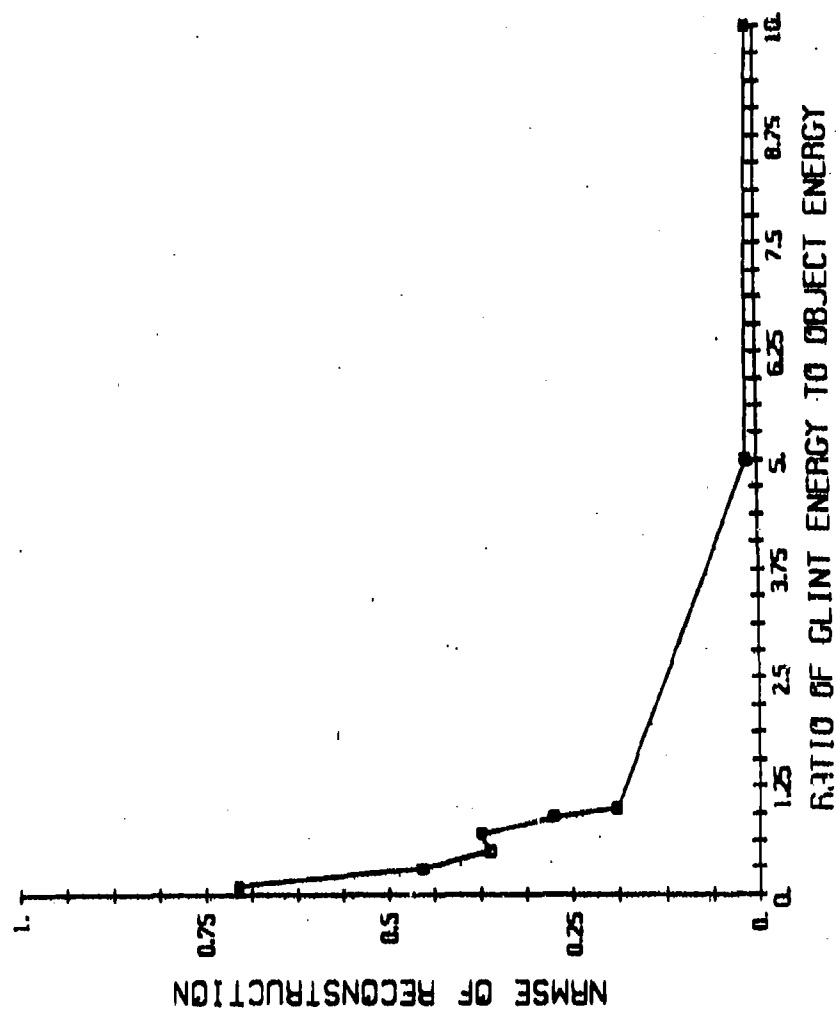FIGURE 5-12. NORMALIZED RMS ERROR VS. K RATIO FOR IMAGES WITH TWO
GLINTS RECONSTRUCTED BY THE ITERATIVE TRANSFORM ALGORITHM.

Diffraction effects due to the aperture are not included in this simulation. The inclusion of diffraction effects would yield poorer performance; further research is needed to develop improved algorithms for this case.

5.4 RECURSIVE AUTOCORRELATION ALGORITHM

Initially a recursive autocorrelation-based reconstruction algorithm was investigated. It was later overshadowed by the algorithms described above, but we include it here for the sake of completeness.

We assume that the object has a single glint of magnitude a and a diffuse part, d(x), so that it can be modeled as

$$f(x) = a \, \delta(x) + d(x) \qquad (5\text{-}21)$$

and its autocorrelation function as

$$r_f(x) = |a|^2 \, \delta(x) + r_d(x) + a^* \, d(x) + a \, d^*(-x) \qquad (5\text{-}22)$$

which contains within it a representation of the diffuse part, d(x), multiplied by a^*. Unless the glint satisfies the holography condition, however, the other terms will overlap the desired term, $a^* \, d(x)$, making it not immediately available. If the glint does not satisfy the holography condition but is to one side of d(x), then only the term $r_d(x)$ overlaps the desired term. Under that circumstance, the following recursive reconstruction algorithm is possible. After estimating the glint strength, first estimate $a^* \, d(x)$ by windowing one side of $r_f(x)$. Then form a second estimate by subtracting from $r_f(x)$ an estimate of $r_d(x)$, computed from the estimate of d(x), and windowing the result. This process is continued until no further changes are made. In practice this method requires a strong glint and was not as successful as the methods described in the previous sections.

102

5.5 EFFECT OF GLINT STRENGTH ON DATA QUANTIZATION ERROR

It is assumed that the laser-illuminated object has a glint component and a diffuse component. It may be that the glint, say from a flat panel, appears only for certain angular orientations of the object. A problem is that the energy from the glint can far exceed the energy from the entire diffuse component of the object. Then aperture-plane detectors having a finite dynamic range (or a finite number of quantization levels) may have the information about the diffuse component overwhelmed by the energy from the glint. In this section this problem is analyzed.

For the case of a single glint, the model for the object is again

$$f(x) = a \, \delta(x) + d(x) \tag{5-23}$$

which has Fourier transform

$$F(u) = a + D(u) \tag{5-24}$$

where $D(u)$ is a zero-mean Gaussian random variable with variance σ^2. The detected quantity is the intensity

$$|F(u)|^2 = |a + D(u)|^2$$

$$= a^2 + 2 a \, Re[D(u)] + |D(u)|^2 \, , \tag{5-25}$$

where we have used the fact that the phase of the glint, a, can, without loss of generality, be set to zero. Letting $w = |F(u)|^2$ and $g = a^2$, the intensity follows a modified Rician or non-central Wishart distribution:

$$p_w(w) = (2\pi)^{-1} \exp[-w/(2\sigma^2)] \, \exp[-g/(2\sigma^2)] \, I_0\left(\sqrt{wg}/\sigma^2\right) \, . \tag{5-26}$$

To simplify this further, we can define intensities normalized to the energy in the diffuse part of the object: replacing $w/(2\sigma^2)$ by w and $g/(2\sigma^2)$ by g, we have

$$p_W(w) = e^{-w} e^{-g} I_0\left(2\sqrt{wg}\right) \qquad\qquad (5\text{-}27)$$

The mean and variance of w are $1 + g$ and $1 + 2g$, respectively.

The assumed quantization operation is illustrated in Figure 5-13, which shows a linear quantizer with an offset γ and N quantization intervals, each of width Δw. For a given value of the relative glint strength, g, the mean-squared error due to the quantization rule on the probability distribution $p_w(w)$ can be numerically computed.

Optimum quantizers were derived for two cases: no glint and a very strong glint. This was accomplished by arriving at a signal-to-noise expression as a function of N, Δw, and γ, and then solving nonlinear equations for the optimum Δw and γ using Newton's method. The results are summarized in Table 5-1.

Table 5.1 Optimum Quantizer Intervals

N	For zero glint		For large glint	
	Δw	SRN(db)	Δw	SRN(db)
256	.04368	37.27	.03076	40.57
512	.02432	42.43	.01650	46.04
1024	.01341	47.65	.00879	51.55
2048	.00734	52.94	.00465	57.11
4096	.00399	58.28	.00245	62.71

The signal-to-noise ratios (SNR's) of four quantizers were compared for the case of a design optimized for g = 10,000 (an enormous maximum glint strength), for various values of N from 256 to 4096, and for

104
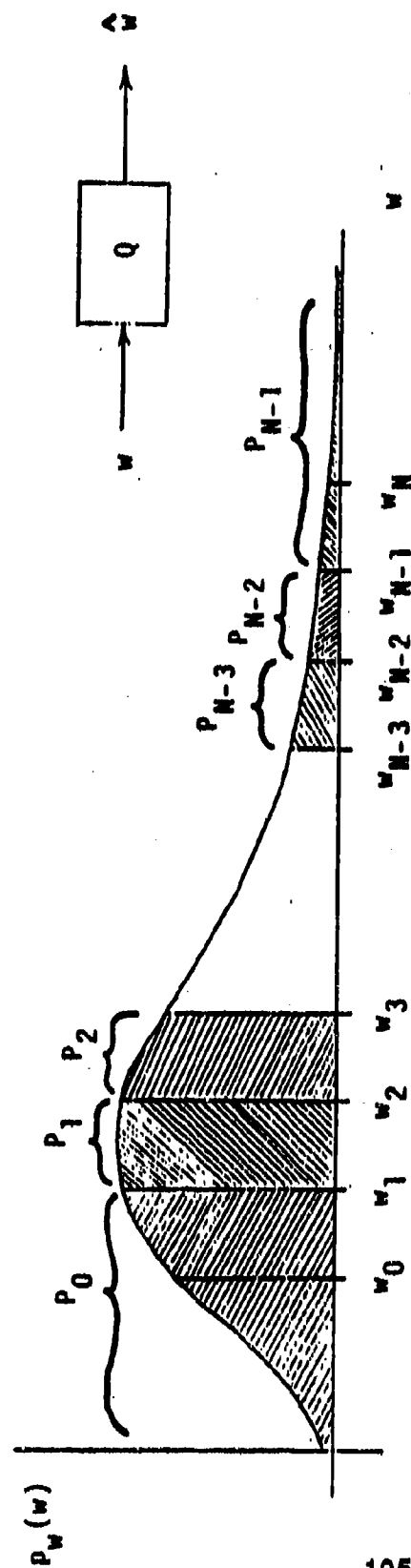
Linear quantizer with offset: $w_n = n\Delta w + \gamma \quad n = 0, \ldots, N$

Quantizer output: $\hat{w}_n = \begin{cases} w_0 + \delta & w < w_0 & \text{underflow} \\ w_n + \delta & w_n \leq w < w_{n+1} & \text{nominal} \\ w_{N-1} + \delta & w \geq w_N & \text{overflow} \end{cases}$

Quantization noise: $e \equiv w - \hat{w}$

FIGURE 5-13. UNIFORM QUANTIZER FOR MODIFIED RICIAN LASER INTENSITY DISTRIBUTION.

105

values of an actual glint strength of 0, 10, 100, 1,000, and 10,000. The results are shown in Table 5.2. From this table it can be seen that with a fixed step size (optimized for g = 10,000), the SNR for the smaller values of g is very poor. The addition of a dynamic, optimum step size yields dramatic improvement in SNR for the smaller-glint cases. The same effect as a dynamic step size can be achieved by an automatic gain control (say, attenuating the light arriving at the detector when the glint becomes very bright). The addition a dynamic, optimum offset yields additional gains in SNR, especially for the brighter-glint cases.

The reason that automatic gain control is important is seen from the fact that in the second term, the information-carrying quantity, of Eq. (5-15) is multiplied by the glint strength.

The major conclusion from this study is that in order to allow for very large glints, we should have a dynamic or adaptive quantizer. The most important feature of the dynamic quantizer would be a variable step size Δw. This could be achieved by an automatic gain control. Helpful, but less important, is to allow for a dynamic offset γ. The results were derived for very large glints; the optimization of the quantizer for intermediate-strength glints, which are likely to occur in practice, would require additional research.

Table 5-2. Comparison of Uniform Quantizers. The tables give the SNR as a function of relative glint strength (along the top row) and number of quantization levels (along the left side).

FIXED OFFSET/FIXED STEP SIZE

SNR (dB)	0	10	100	1000	10000
256	0	.0006	2.05	11.55	21.52
512	0	.0671	7.57	17.57	27.48
1024	.0162	3.71	13.59	23.59	33.29
2048	.750	9.80	19.62	29.62	38.28
4096	3.93	15.83	25.64	35.64	41.85

OPTIMUM OFFSET/FIXED STEP SIZE

SNR (dB)	0	10	100	1000	10000
256	1.??	12.24	22.05	32.05	39.18
512	?.??	18.28	28.09	38.09	41.27
1024	11.28	24.22	34.09	44.09	42.19
2048	17.16	30.25	40.12	50.12	42.37
4096	23.13	35.47	46.13	56.13	42.57

FIXED OFFSET/OPTIMUM STEP SIZE

SNR (dB)	0	10	100	1000	10000
256	37.27	40.26	40.00	30.53	21.52
512	42.43	45.75	43.81	36.50	27.36
1024	47.65	51.05	49.61	42.22	32.98
2048	52.94	56.08	55.44	48.35	39.48
4096	58.28	60.77	61.27	54.25	45.48

OPTIMUM OFFSET/OPTIMUM STEP SIZE

SNR (dB)	0	10	100	1000	10000
256	37.37	40.19	40.57	40.57	40.57
512	42.43	45.53	46.04	46.04	46.04
1024	47.65	49.73	51.55	51.55	51.55
2048	52.94	52.50	57.11	57.11	57.11
4096	58.28	58.07	62.71	62.71	62.71

REFERENCES

[5.1] M. Elbaum et al., "Laser Correlography: Transmission of High-Resolution Object Signatures through the Turbulent Atmosphere," Riverside Research Institute Report T-1/306-3-11 (31 October 1974) (available from NTIS, report AD-A013-424).

[5.2] J.R. Fienup, "Reconstruction of a Complex-Valued Object from the Modulus of Its fourier Transform Using a Support Constraint," J. Opt. Soc. Am. A 4, 118-123 (1987).

[5.3] P.S. Idell, J.R. Fienup and R.S. Goodman, "Image Synthesis from Nonimaged Laser Speckle Patterns," Opt. Lett. 12, 858-860 (1987).

[5.4] P.S. Idell and J. Gonglewski, "Image Synthesis from Nonimaged Laser Speckle Patterns: Experimental Demonstrations of Imaging Correlography," Thirteenth DARPA Strategic Systems Symposium, 20-23 October 1987, Naval Postgraduate School, Monterey, CA.

[5.5] E.N. Leith and J. Upatnieks, "Reconstructed Wavefronts and Communication Theory," J. Opt. Soc. Am. 52, 1123-1130 (1962).

[5.6] J.R. Fienup, T.R. Crimmins, and W. Holsztynski, "Reconstruction of the Support of an Object from the Support of Its Autocorrelation," J. Opt. Soc. Am. 72, 610-624 (1982).

[5.7] J.E. Baldwin and P.J. Warner, "Phaseless Aperture Synthesis," Mon. Not. R. Astr. Soc. 182 411-422 (1978).

[5.8] J.R. Fienup and C.C. Wackerman, "Phase Retrieval Stagnation Problems and Solutions," J. Opt. Soc. Am. A 3, 1897-1907 (1986).

[5.9] J.R. Fienup, "Phase Retrieval Algorithms: A Comparison," Appl. Opt. 21, 2758-2769 (1982).

6.0 IMAGING WITH PARTIAL PHASE INFORMATION

In this section and in Section 7, we describe methods developed for using partial phase information in the phase retrieval/image reconstruction process. For the most difficult objects to reconstruct (complex-valued, having no glints or separated parts), some additional information is essential to obtain a reliable reconstruction, given our present algorithms. One kind of such additional information is partial phase information. Partial phase information can come, for example, from an imaging system that inherently measures or determines the phase. If the partial phase information is nearly complete, so that using that phase yields a useful image, then the phase-retrieval processing can be thought of as a way to clean up the image to improve its quality. This is equivalent to reducing the errors or filling in the gaps in the given partial phase information. If the partial phase information is very incomplete or noisy, then no useful image would result from it, and the phase-retrieval processing would be forming the image in the first place, with the partial phase information helping it to succeed.

Two major cases of partial phase information were considered: (1) phase known well over a small aperture, and (2) noisy phase over the entire aperture. In the first case, it is a matter of filling in the missing phase, but most of the phase is missing. In the second case, it is a matter of correcting the errors in the given phase.

Two scenarios that would correspond to the first case are as follows. Suppose that the object is coherently illuminated with a laser, and intensity measurements are made in an aperture plane of the optical system. In addition, optical field measurements are made over a smaller aperture imbedded in (or contiguous with) the intensity measurements. The optical field measurements could be performed, for example, by heterodyne detection or by two intensity measurements in different planes and the fields reconstructed by the Gerchberg-Saxton

109

algorithm. These optical fields would be aberrated by atmospheric turbulence. In addition, the small aperture would also have a wavefront sensor that measures the atmospheric wavefront error. Aberration-free optical field data could be obtained over the small aperture by subtracting the phase due to the atmosphere from the phase of the measured optical field.

The second scenario representing the first case would be for a system in space having a small, diffraction-limited telescope making optical field measurements, imbedded in a larger aperture over which the aperture-plane intensity measurements are made. In this case a wavefront sensor would not be needed since there would be no atmospheric turbulence to aberrate the optical data for the small, diffraction-limited telescope.

Many different imaging systems could provide data for the second case, that of noisy phase known over the entire aperture. They include active imaging modalities such as the Itek/Western system, triple correlation of aperture-plane intensity, and FOCI and passive imaging modalities such as astronomical speckle interferometry using triple correlation and aperture-plane interferometry using phase closure.

The basic approach to phase retrieval and image reconstruction taken for these scenarios was to use the iterative Fourier transform algorithm to take advantage of all the available data and constraints to form the solution. This approach allows for the combination of a variety of disparate types of information, such as Fourier modulus (square root of intensity), Fourier phase, object-domain support (finite extent) constraint, and nonnegativity (applicable for incoherent images). For the case of phase know well over a small aperture, a variation of the iterative transform algorithm, called the expanding-weighted-mask algorithm, was developed. This initial attempt with the expanding-weighted-mask algorithm gave results that were only partially successful: they were promising but very preliminary and

incomplete. (In a separate, later program funded by the Naval Research Laboratory, this approach was expanded upon and optimized, and yielded very good reconstructed images.) Those preliminary results are described in Section 6.1. For the case of noisy phase over the entire aperture, a variation of the iterative transform algorithm, called the phase variance algorithm, was developed, as described in Section 6.3. In addition, an alternative, entirely new approach was developed for that case: 2-D shear averaging, which is described in Section 7. One other case that was briefly explored was that of knowing one bit of phase. In that case, reconstruction was easily achieved with a windowing of the initial image computed from the given phase followed by cleaning up with the iterative Fourier transform algorithm. This last case, mostly of academic interest since it does not naturally occur in currently known imaging sensors, is described in Section 6.2.

6.1 THE EXPANDING WEIGHTED MODULUS ALGORITHM

If the Fourier intensity is measured over a large aperture and the phase is measured over a small aperture imbedded in the large aperture, then it is possible to use that known phase to help to retrieve the phase over the large aperture. This can be accomplished by enforcing the known phase together with all the other available information (Fourier modulus, object support constraint) using the iterative Fourier transform algorithm.

The support constraint can be gotten from the available data in one of two ways. First, one can use a triple intersection of the autocorrelation support computed from the Fourier intensity to put an upper bound on the support of the object [6.1]. Second, from the small-aperture phase combined with the measured intensity over the small aperture, one can gets a diffraction-limited, but low resolution (owing to the small size of the aperture) image. A support constraint can be formed by an appropriate thresholding of this low-resolution image.

111

The initial estimate for the iterative transform algorithm can be gotten by simply using the complex-valued low-resolution image or by filling the support constraint with complex-valued random numbers.

When the iterative transform algorithm was run with either of the two initial estimates and using either of the two support constraints, and enforcing the small-aperture phase, it stagnated without converging to a solution. Essentially random phases were produced outside the small aperture. Since the ratio of the area of the large aperture to that of the small aperture was chosen to be a large number, the random phases outside the small aperture overwhelmed the influence of the correct phases within the small aperture.

In order to combat this problem, we began development of the expanding weighted modulus algorithm. It consists of the following steps. First the Fourier modulus (the square root of the measured intensity) is multiplied (weighted) by an apodizing function that goes to zero over an area only somewhat larger than the area of the small aperture. Then several iterations are performed. The idea is that with the weighting function in place, the known phase will not be overwhelmed by the unknown phase, which now exists over a much smaller area than before, and furthermore has an associated magnitude that is weighted down in the area of the unknown phase, further reducing its influence. Thus the known phase has a chance to be useful as a constraint that helps to retrieve the unknown phase over the larger area. Next the weighting function is replaced by a weighting function that is nonzero over a wider area. Then more iterations are performed, retrieving the unknown phase over this wider area. This process of widening the weighting function and performing more iterations is repeated until the weighting function is nonzero over the entire large aperture, at which point the entire phase is retrieved and a fine-resolution image is reconstructed.

Several trials of the expanding weighted modulus algorithm were made, and, while the results showed promise, the images that were produced were far from diffraction limited. For these experiments, the weighting functions were chosen to be either rectangle functions or triangle functions, and the number of intermediate weighting functions used was small. (These initial results were greatly improved upon in a separate effort, in which it was found that by using weighting functions with continuous derivatives and using a very much larger number of intermediate weighting functions, the reconstructions could be reliable and of high quality [6.2]).

6.2 RECONSTRUCTION WITH ONE BIT OF PHASE

One bit of phase information, which is equivalent to knowing the sign of the real part of the Fourier transform, is well known to contain considerable information. First of all, if the image is "causal," i.e., it is located completely to one side of the optical axis, then the inverse Fourier transform of the Fourier modulus combined with the one bit of phase yields an image plane with the following components: the desired image, the twin (complex conjugated and reflected about the origin) of the desired image, and noise and artifacts. The strength of the noise and artifacts depends on the degree of oversampling of the Fourier modulus data. With a high degree of oversampling the noise and artifact level can be very low, yielding a good-quality image immediately. This is illustrated in Figure 6-1, which shows the object (a) and the image reconstructed by inverse transforming the Fourier magnitude plus one bit of phase (c). For comparison, Figure 6-1(b) shows the inverse transform of a constant modulus with the one bit of phase. The quality of this latter image shows that the one bit of phase without any modulus information is very useful indeed. Figure 6-1(d) shows the result of using a windowed version of Figure 6-1(c) as an initial estimate, then performing several iterations of the iterative transform algorithm using a support constraint in order to refine the phase. The iterative transform algorithm successfully removed most of the noise and artifacts.

FIGURE 6-1. RECONSTRUCTION WITH ONE BIT OF PHASE. (a) Object, (b) image from a constant modulus combined with one bit of phase, (c) image from the correct modulus combined with one bit of phase, (d) image reconstructed by the iterative Fourier transform algorithm using (c) as an initial estimate.

From Figure 6-1 we see that one bit of phase information is very powerful information, and that what noise and artifacts it introduces can be easily cleaned up by the iterative Fourier transform algorithm. Unfortunately, none of the sensors presently under development yield an accurate measure of one bit of phase, so the results shown in Figure 6-1 are presently of academic interest only.

6.3 PHASE VARIANCE ALGORITHM

In what follows is described a modification of the iterative transform algorithm which uses a poorly-known phase across the Fourier-domain aperture.

Let the object and its Fourier transform be $f(x)$ and $F(u) = |F(u)| \exp[i\Psi(u)]$, respectively. Suppose we measure

$$G_o(u) = |G_o(u)| \exp[i\theta(u)]$$

$$= F(u) \exp[i\phi_e(u)] = |F(u)| \exp\{i[\Psi(u) + \phi_e(u)]\} \qquad (6\text{-}1)$$

where $\phi_e(u)$ is a phase error with known (or known approximately) variance σ. So the measured (noisy) phase is

$$\theta(u) = [\Psi(u) + \phi_e(u)]_{\text{mod } 2\pi} \cdot \qquad (6\text{-}2)$$

The image gotten by inverse Fourier transforming $G_o(u)$ would be $g_o(x)$, a blurred image.

We seek ways to improve the phase estimate over that given by the measurement $\theta(u)$. This may be accomplished by the iterative Fourier transform phase retrieval algorithm which uses additional information in the object domain, such as nonnegativity and/or support constraints to infer the true phase of $F(u)$. Two approaches are described next.

The first approach is to perform the usual phase retrieval algorithm, typically cycles of hybrid input-output (HID) and error-reduction (ER), and simply use $\theta(u)$ as the initial estimate for the Fourier-domain phase. The Fourier-domain constraint would be the measured modulus $|G_0(u)| = |F(u)|$.

The second approach is to constrain the phase during the iterations to lie near $\theta(u)$. Constraining the phase to equal $\theta(u)$ does no good since one would simply get the blurred image with no change. Instead it is more useful to allow the phase to wander from $\theta(u)$, but not let it wander too far. This can be accomplished using the phase variance algorithm, which is described as follows. In the Fourier domain, as well as constraining the modulus to equal $|F(u)|$, constrain the phase to not differ from $\theta(u)$ by more than $c\sigma$, where c, the variance factor, is a real constant on the order of unity. In order to account for 2π ambiguities, this should be performed as follows, where ϕ is the phase of the Fourier transform of the input object to the iterative loop and ϕ' is the altered phase:

$$\phi' = \begin{cases} \theta - c\sigma & , \quad (\phi - \theta)_{mod\ 2\pi} < -c\sigma \\ \phi & , \quad -c\sigma \leq (\phi - \theta)_{mod\ 2\pi} \leq c\sigma \\ \theta + c\sigma & , \quad (\phi - \theta)_{mod\ 2\pi} > c\sigma \end{cases} \qquad (6\text{-}3)$$

$$= \text{VCLIP}[(\phi - \theta)\ mod\ 2\pi,\ -c\sigma,\ c\sigma] + \theta \qquad (6\text{-}4)$$

where

$$\text{VCLIP}(a,\ b,\ c) \equiv \begin{cases} b & ; \quad a < b \\ a & , \quad b \leq a \leq c \\ c & , \quad a > c \end{cases} \qquad (6\text{-}5)$$

is a Numerix array processor math library function. (A convenient way to perform the modulo 2π function is by the successive operations RECO and POLAR, which converts the modulus/phase to real/imaginary and then back to modulus/phase.) This Fourier domain operation is illustrated in Figure 6-2.
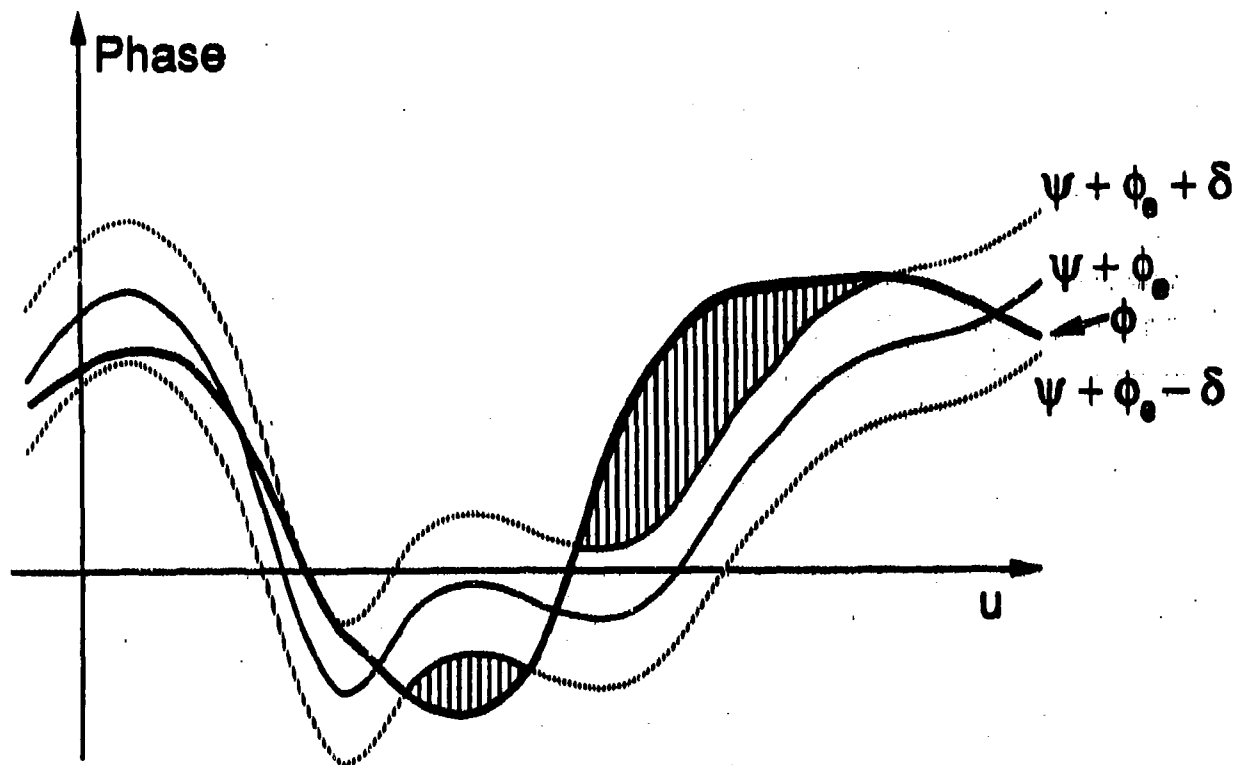
$\psi + \phi_e$ = Degraded phase

ϕ = Computed phase

δ = $c\sigma$ = Phase limit

σ = Phase error standard deviation

FIGURE 6-2. PHASE VARIANCE ALGORITHM. The phase $\phi'(u)$ is constrained to lie within $c\sigma$ of the given phase, $\theta(u)$.

Several variations of the phase variance algorithm were attempted for both the cases of a real, nonnegative object and a complex-valued object. In the object domain we can use either the hybrid-output (HIO) or error-reduction (ER) algorithm while one employs the phase variance algorithm in the Fourier domain. We refer to these two combinations as PVHIO and PVER, respectively. Although HIO usually outperforms ER, we found that PVER usually outperforms PVHIO.

Several values of the variance factor c were tested. The value of c should be small enough to reinforce the given phase values, but large enough to allow the phase the freedom to adjust to become more consistent with the more accurate Fourier modulus data. Generally c in the range of 0.6 to 1.0 worked the best. Increasing or decreasing the value of c as the iterations progressed did not seem to improve convergence.

Two different initial estimates were tested. One was the image $g_0(x)$ obtained using the noisy phase estimate. This is equivalent to starting in the Fourier domain with phase $\phi' = \theta$, the noisy phase. The second was an image consisting of the support constraint filled with uniformly distributed random numbers. Most often the noisy-phase initial estimate performed better than the random initial estimate.

It was found that the phase variance algorithm would improve the estimate for several iterations, and then it would stagnate. The reason for the stagnation appears to be that the outlying noisy phase values for which the phase error $|\phi_e| > c\sigma$ are inconsistent with the phase variance constraint [Eq. (6-3)]. We found it best to stop enforcing the phase variance constraint at this point and thereafter to only enforce the Fourier modulus constraint (along with the image-domain support constraint). That is, after the phase variance algorithm stagnates, continue with the traditional iterative transform algorithm, using cycles of HIO and ER.

After testing numerous combinations of algorithm types and algorithm parameters, we arrived at the following combination that seemed to work the best on average. Perform twenty iterations of PVER with c = 0.8, then ten iterations of ER, and finally several cycles, each cycle consisting of 20 HIO (beta = 0.7) and 10 ER, until stagnation (no further progress) occurs. After every other cycle, enlarge the support constraint by adding to it each nearest-neighbor pixel that was previously outside the support. In order to reduce sidelobes in the image, to make the support constraint more effective when diffraction effects are included, the Fourier modulus should be weighted with an apodizing function. For the experiments described in what follows, we used a weighting function proportional to the autocorrelation of a circle [giving an impulse response of the form $(J_1(r)/r)^2$ to the complex image].

The progress of the iterative transform algorithm is monitored by computing the object domain error metric,

$$ODEM = \sqrt{\frac{\sum_{x \in \gamma} |g'(x)|^2}{\sum_x |f(x)|^2}} \qquad (6\text{-}6)$$

where γ is the set of points at which $g'(x)$ violates the object-domain constraints. It is a measure of how close the output image, $g'(x)$, is to satisfying the object-domain constraints. For these digital simulation experiments, in which we also know the actual object, we can also compute the absolute error,

$$ABSERR = \sqrt{\frac{\sum_x |g'(x - x_s) - f(x)|^2}{\sum_x |f(x)|^2}} \qquad (6\text{-}7)$$

where x_s is the shift of the output image $g'(x)$ that maximizes its correlation with the true object $f(x)$. For images that are recognizable and have some utility, ABSERR is typically below 0.5. For images that are good representations of the object, ABSERR is typically about 0.3 or less.

Figure 6-3 show ABSERR as a function of iteration number for the case of using the original iterative transform algorithm with a random initial estimate, for the case of a real-valued, nonnegative object when there is no Fourier phase information. Each curve represents a different trial of the algorithm with a different random start. For the majority of the cases the HIO algorithm converges to a good image, whereas the ER algorithm rarely does for real, nonnegative objects. When the algorithm was started with a noisy phase estimate, without reinforcing it during the iterations, it did not improve the performance significantly.

Phase errors used for these experiments were generated using McGlammery's method [6.3]. These phase errors are similar to those that would result from atmospheric turbulence. The adjustable parameters of the phase errors are the standard deviation, σ, and the correlation length, corl.

Figure 6-4 shows the convergence (in terms of ABSERR) of the phase variance algorithm for several values of the variance factor, c. From this we see that the optimum value of c for this case is about 0.8 to 1.0. Figure 6-5 shows the same thing in terms of ODEM. Although the values of ODEM are typically much less than the values of ABSERR, they correlate fairly well with the values of ABSERR.

Figure 6-6 show blurred images and images reconstructed by the phase variance algorithm for three different phase errors for the case of a real, nonnegative object. In all three cases, with no noise on the Fourier modulus, the quality of the reconstructed images was the

Reconstruction Using the Original Iterative Algorithm
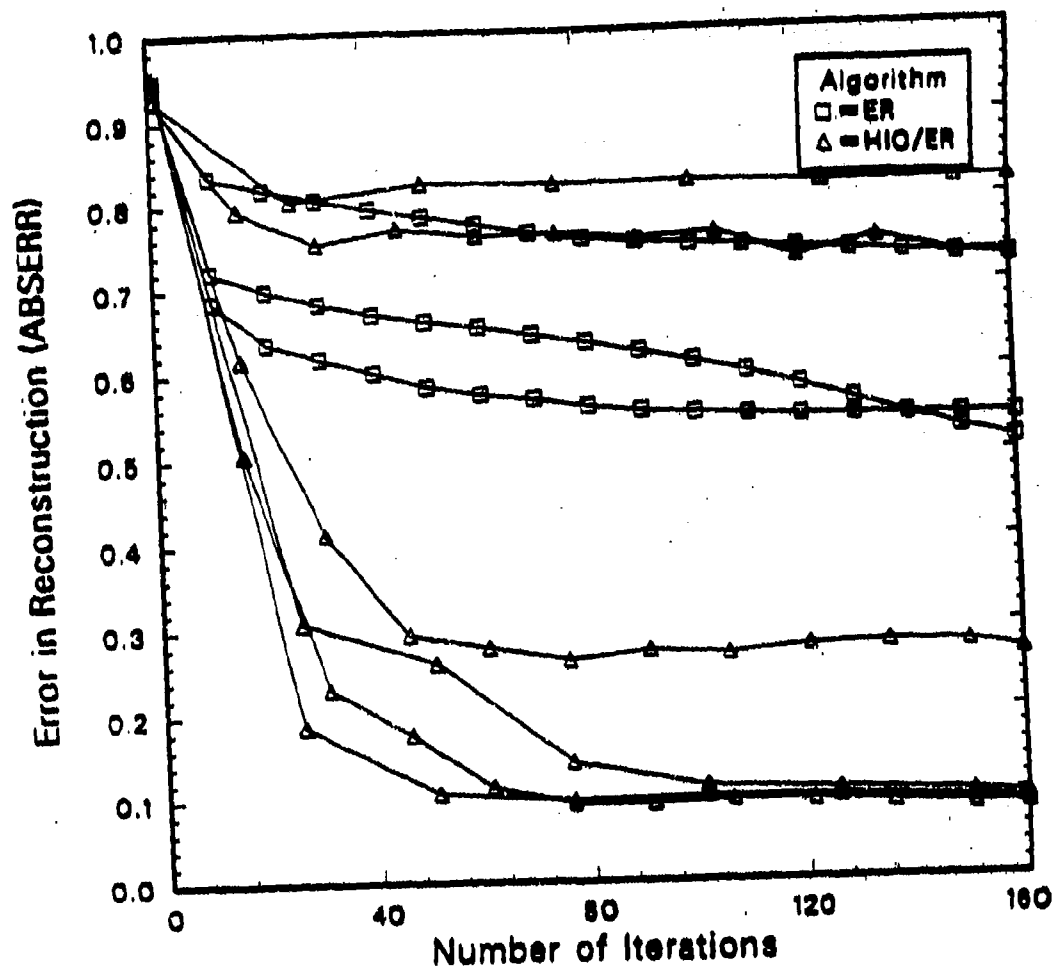## Random Inputs

FIGURE 6-3. CONVERGENCE OF THE STANDARD ALGORITHMS.

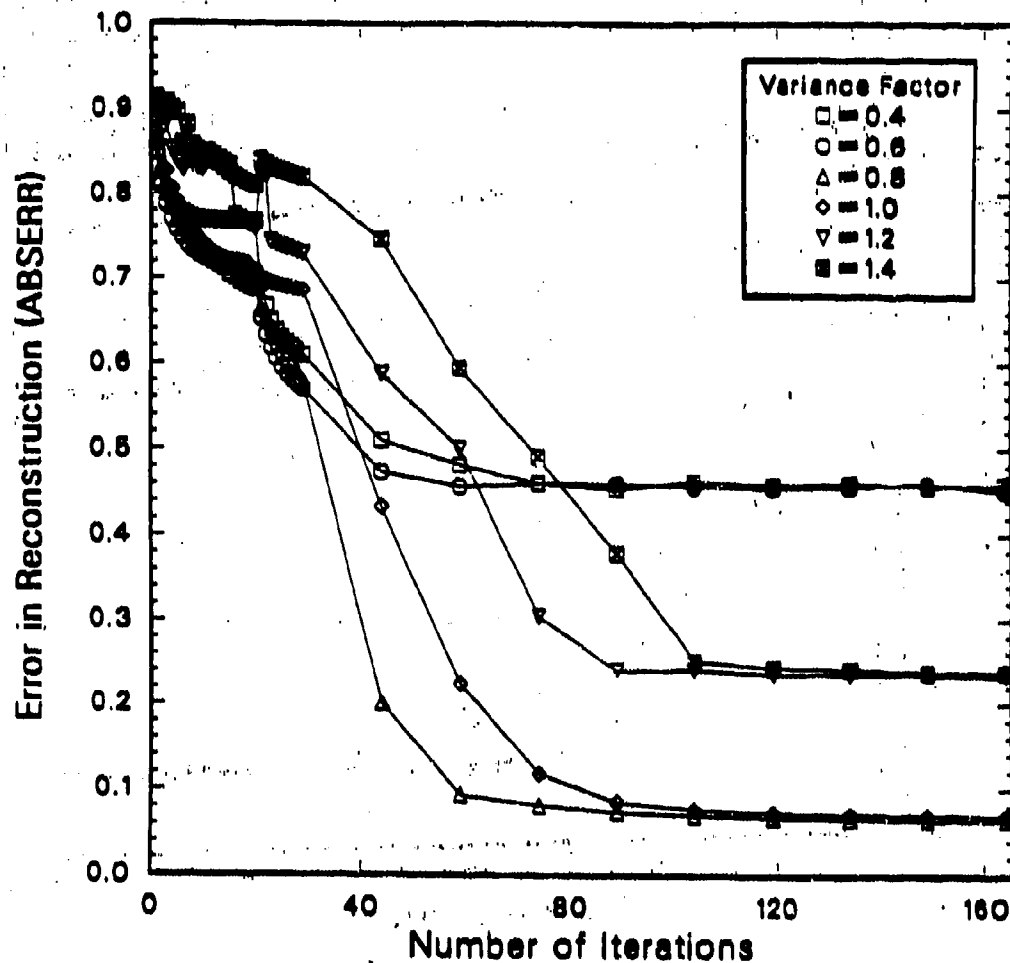# Reconstruction Using Phase Variance Algorithm
$\sigma = 2\pi/4$, corl=6

FIGURE 6-4. CONVERGENCE (ABSERR) OF THE PHASE VARIANCE ALGORITHM FOR VARIOUS C.

Reconstruction Using Phase Variance Algorithm
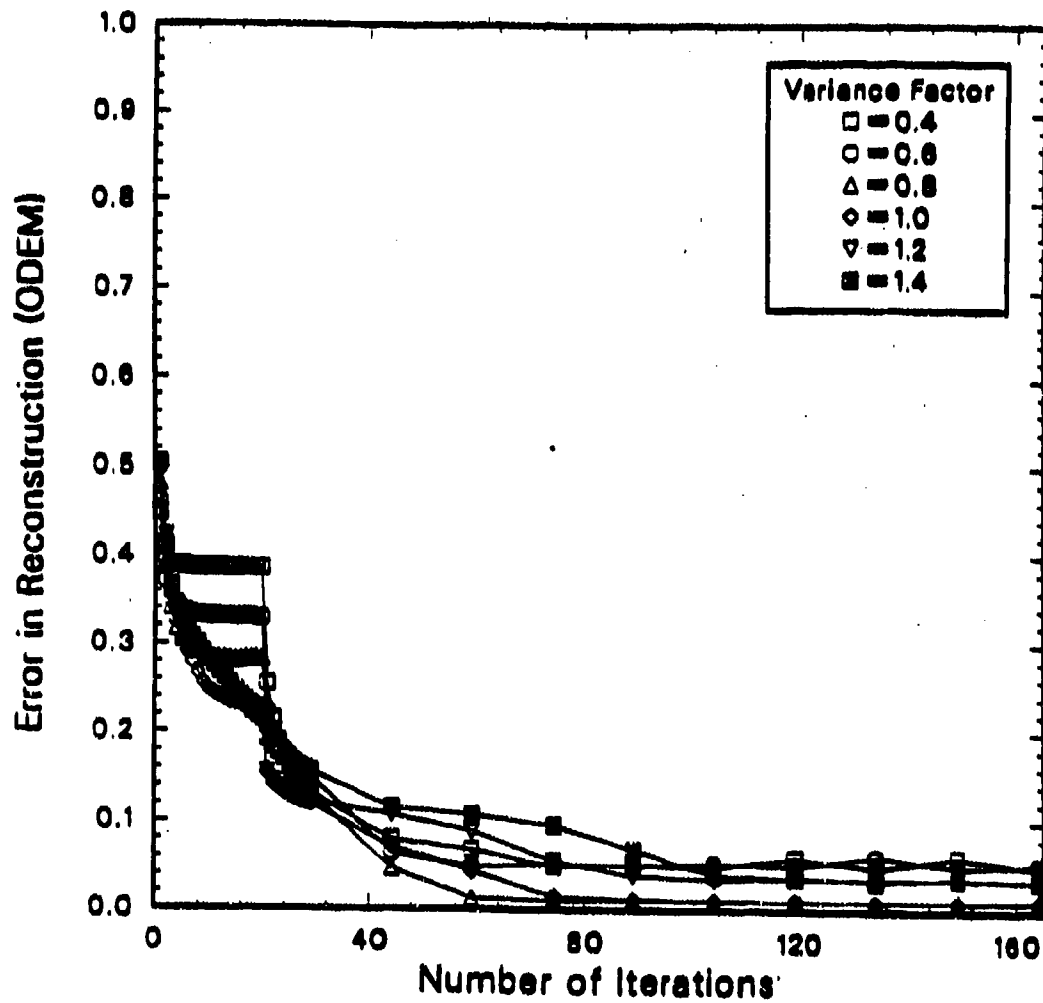## $\sigma = 2\pi/4$, corl=6

FIGURE 6-5. CONVERGENCE (ODEM) OF THE PHASE VARIANCE ALGORITHM FOR VARIOUS C.
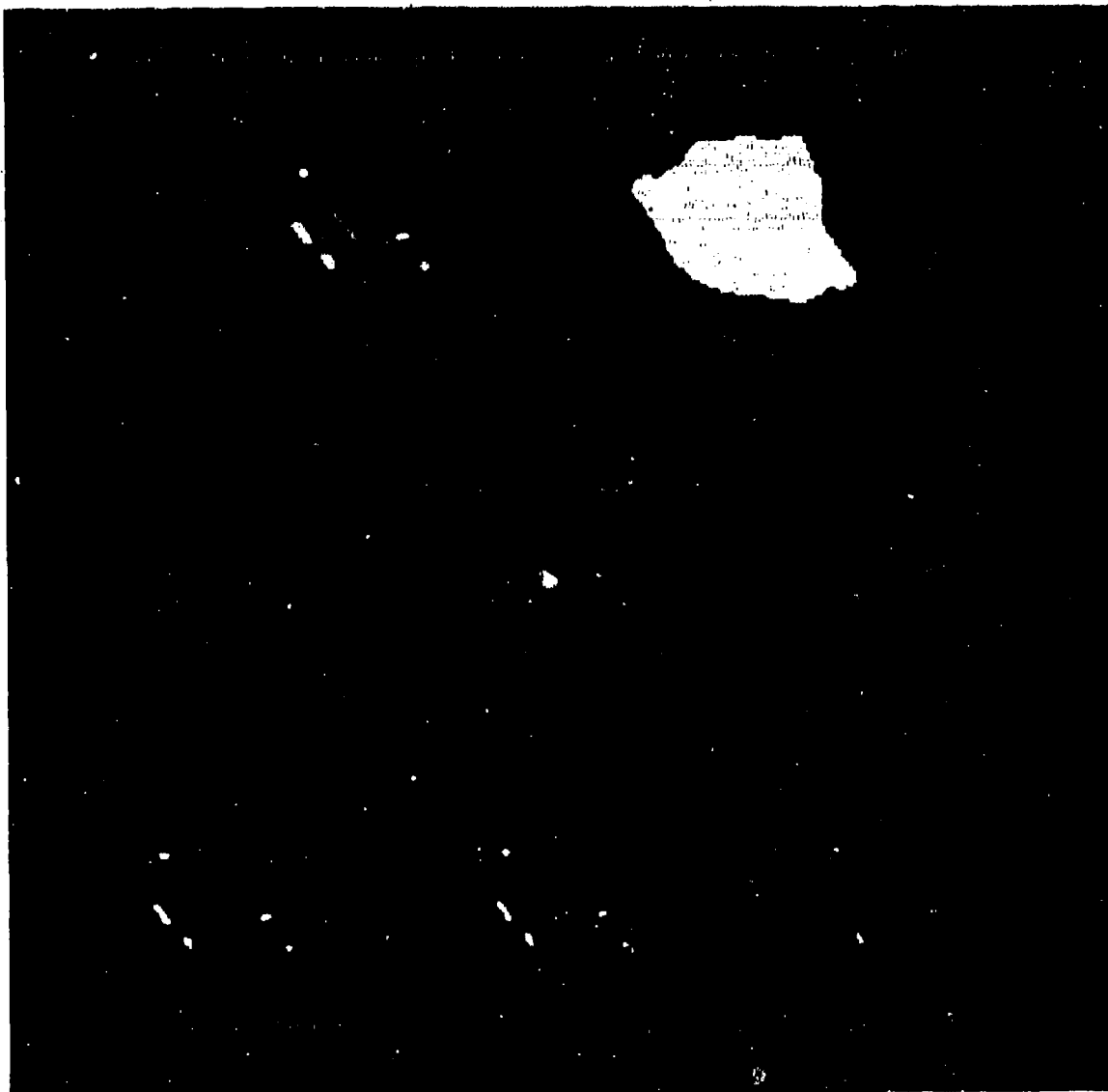
123

FIGURE 6-6. RECONSTRUCTION OF REAL, NONNEGATIVE IMAGES BY THE PHASE VARIANCE ALGORITHM. (a) Object; (b) support constrain; (c)-(d) blurred images, with (c) phase errors $\sigma = \pi/2$ radians and corl = 6 pixels, with (d) $\sigma = \pi/2$ and corl = 30, and with (e) $\sigma = \pi/5$ and corl = 6; and (f) - (h) corresponding images reconstructed by the phase variance algorithm.

same in all three cases, although the convergence was faster for the cases with the smaller given phase error.

The reconstruction of complex-valued objects is much more difficult since one no longer has the powerful nonnegativity constraint. For the complex-valued, speckled versions of the object shown in Figure 6-6, the conventional iterative transform algorithm, when starting with a random initial estimate, failed to reconstruct a recognizable image. When the noisy phase was used to start the algorithm, however, the conventional iterative transform algorithm improved the image quality substantially, although the reconstructed image remained imperfect. The phase variance algorithm similarly reconstructed a substantially improved, but imperfect image. The results from the phase variance algorithm were slightly better than those of the conventional algorithm for these cases. This is illustrated by Figures 6-7 to 6-9.

Figure 6-10 shows the convergence for the case of Fourier modulus data corrupted by photon noise. The iterations improved the RMS error of the image for the cases of more than 120 photons per aperture-plane speckle (or 10^5 total photons). However, for lower light levels, the algorithm can make the image worse. This happens when the Fourier magnitude data are noisier than the phase data; then adjusting the phase to be more consistent with the noisy modulus data is counterproductive. In such a case it would actually make sense to adjust the modulus to be more consistent with the phase data. Figure 6-11 shows the RMS error of the reconstructed image as a function of the total number of photons. Figure 6-12 shows three of the reconstructed images. 3×10^5 total photons (120 photons per speckle) were required to obtain improved imagery.

In summary, we have developed a new variation, the phase variance algorithm, of the iterative transform algorithm which reconstructs a fine resolution image when degraded Fourier phase data is available. For real, nonnegative objects it converges faster and more reliably

125

Reconstruction using Iterative Phase Retrieval Algorithm
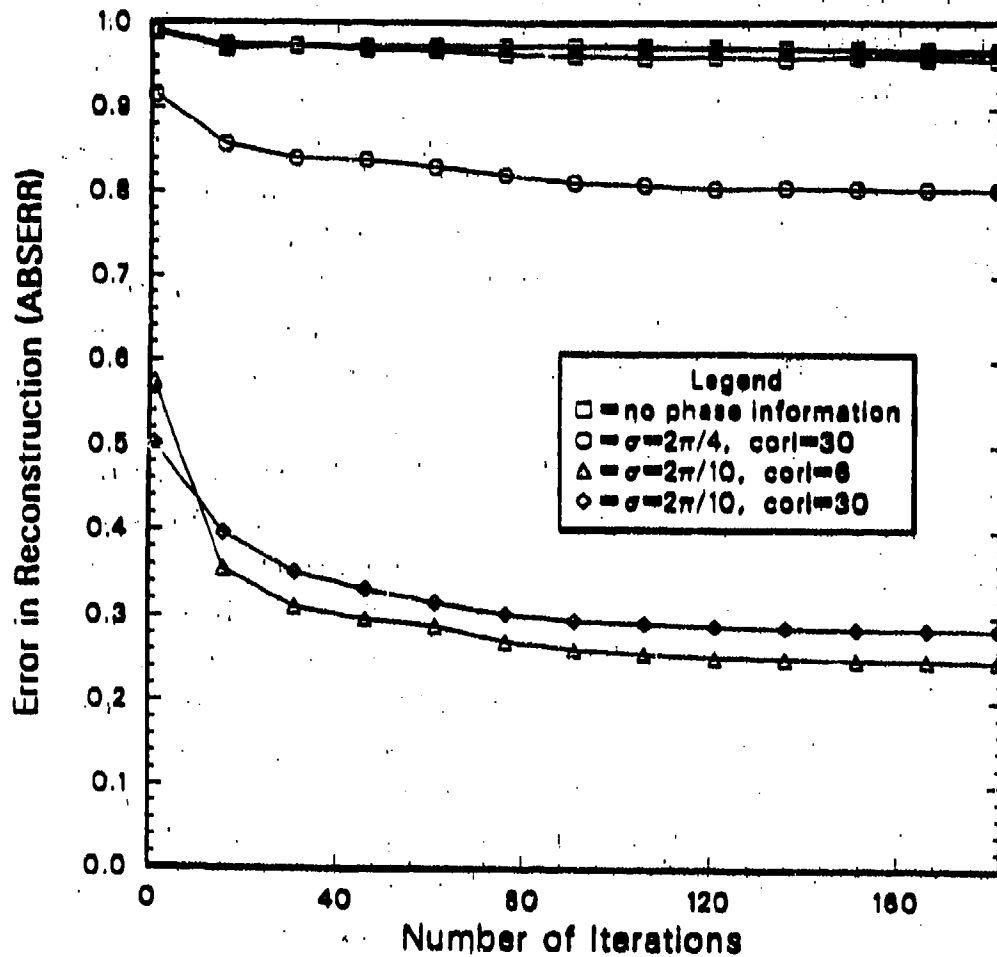## No Phase Information vs. Noisy Phase Input

FIGURE 6-7. CONVERGENCE OF THE CONVENTIONAL ALGORITHM FOR A COMPLEX-VALUED OBJECT.

Reconstruction using Phase Variance Algorithm
No Phase Information (Reg. recon.) vs.
Noisy Phase Input, Phase Variance Algorithm
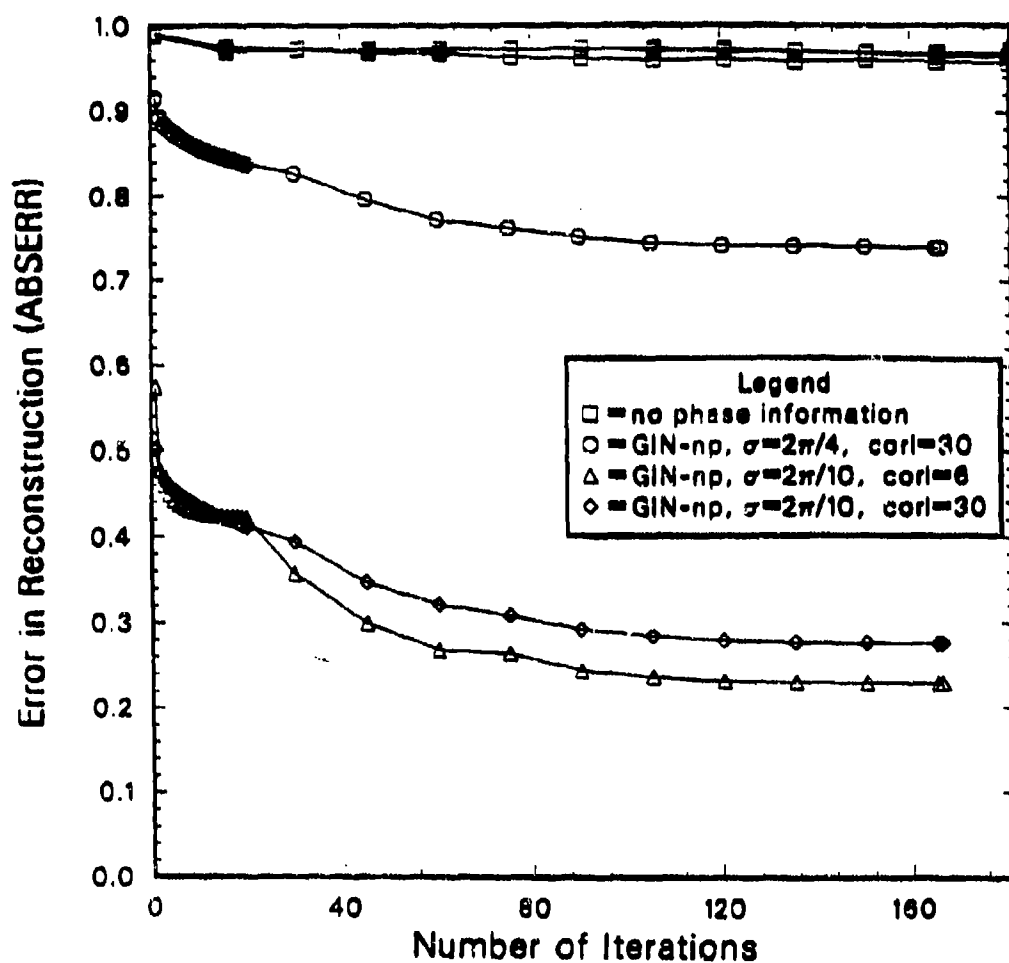
FIGURE 6-8. CONVERGENCE OF THE PHASE VARIANCE ALGORITHM FOR A COMPLEX-VALUED OBJECT.
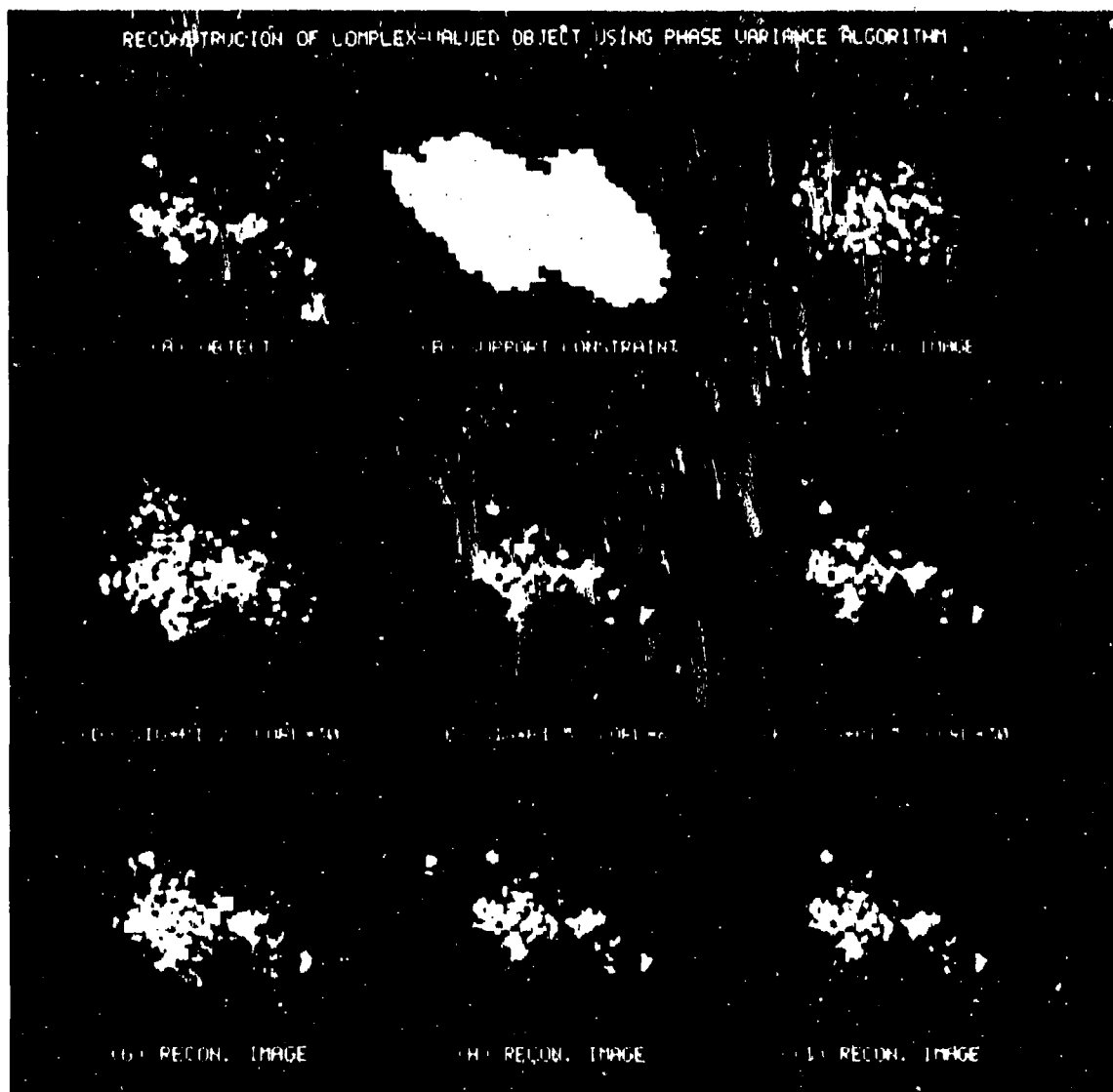
FIGURE 6-9. RECONSTRUCTION OF COMPLEX-VALUED IMAGES BY THE PHASE VARIANCE ALGORITHM. (a) Object; (b) support constraint; (c) image reconstructed with no phase information; (d)-(f) blurred images, with (d) phase errors $\sigma = \pi/2$ radians and corl = 30 pixels, with (e) $\sigma = \pi/5$ and corl = 6, and with (f) $\sigma = \pi/5$ and corl = 30; and (g) - (i) corresponding images reconstructed by the phase variance algorithm.

Reconstruction Using Phase Variance Algorithm
$\sigma = 2\pi/10$, corl $= 6$
Poisson noise added to Fourier magnitude
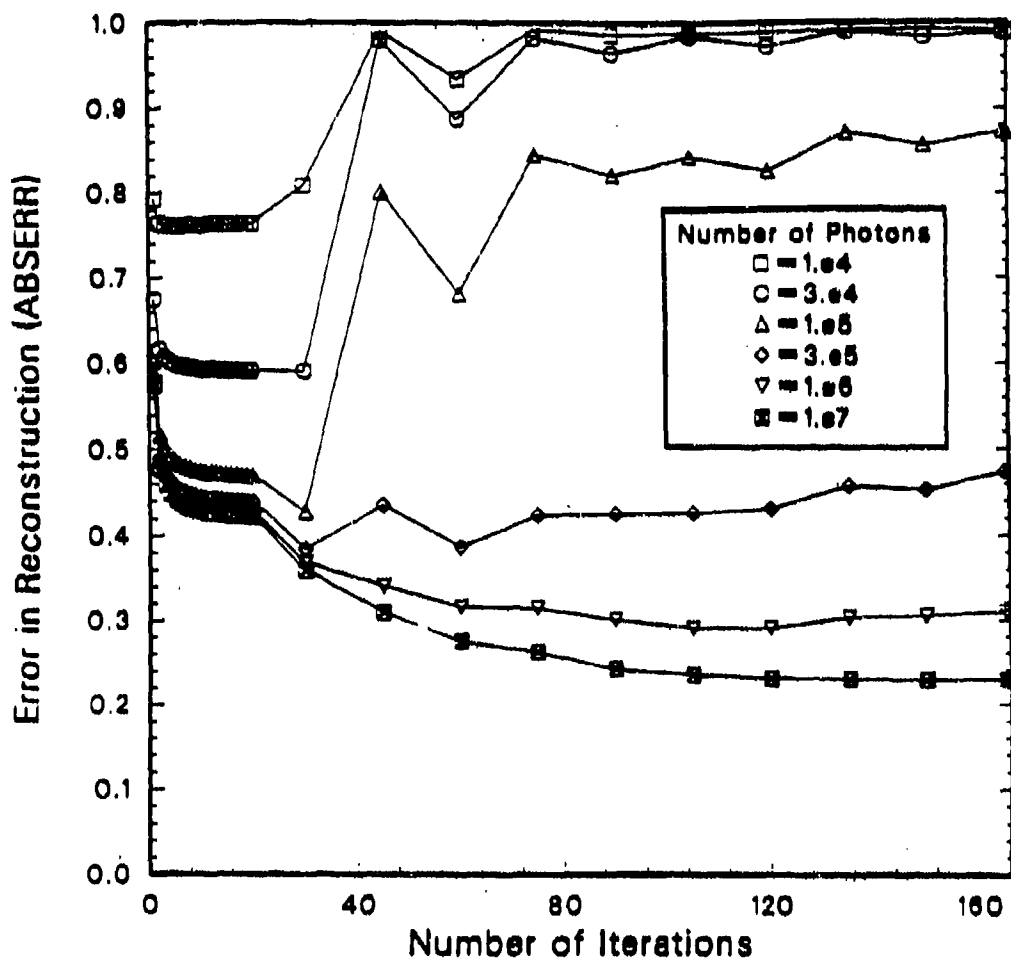
FIGURE 6-10. CONVERGENCE OF THE PHASE VARIANCE ALGORITHM FOR A COMPLEX-VALUED IMAGE FROM NOISY FOURIER MODULUS DATA. For $\sigma = \pi/5$ and corl $= 6$.

Reconstruction using Phase Variance Algorithm
Poisson noise added to Fourier intensity
$\sigma = 2\pi/10$, corl = 6
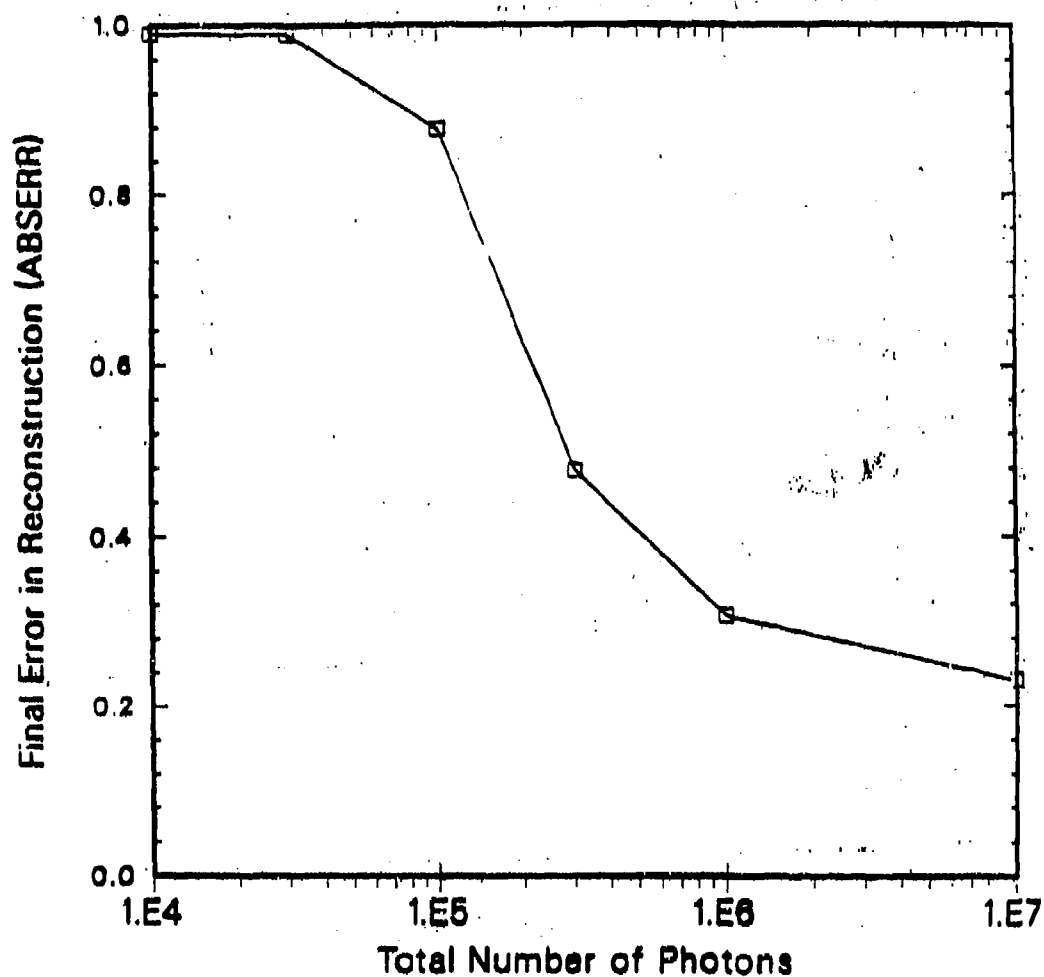
FIGURE 6-11. RMS ERROR OF THE RECONSTRUCTED IMAGES AS A FUNCTION OF THE TOTAL NUMBER OF PHOTONS.

FIGURE 6-12. RECONSTRUCTION OF COMPLEX-VALUED IMAGES BY THE PHASE VARIANCE ALGORITHM. (a) - (c) Noisy Fourier modulus estimates (their squares, the intensities, were subjected to photon noise), with (a) 10^7, (b) 10^6, and (c) 3 x 10^5 total photons; (d) - (f) images degraded by the phase error; and (g) - (i) the corresponding reconstructed images.

131

than the conventional iterative transform algorithm. For complex-valued objects, which are difficult to reconstruct, it reconstructs images of quality substantially better than that of the blurred images given by the available noisy phase data.

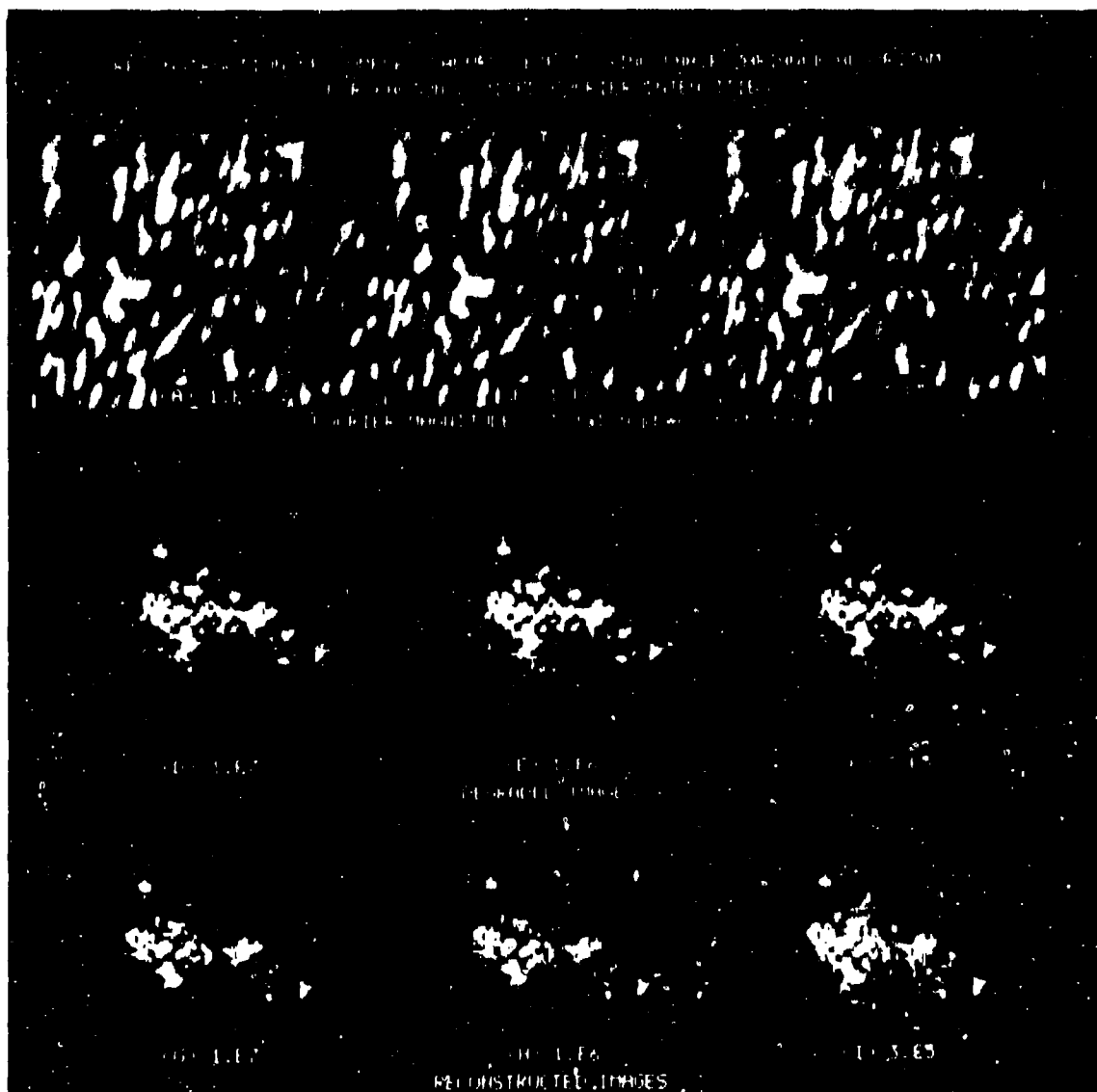Other variations of the phase variance algorithm are possible which may yield improved performance. Rather than using a formula for the new phase estimate such as Eq. (6-3) which abruptly changes at a threshold value, it may be better to have a formula that changes continuously and smoothly with the data. An example of such a formula would be

$$\phi' = \theta + c\sigma \ln[1 + |\phi - \theta|/(c\sigma)] \, \text{sign}(\phi - \theta) \tag{6-8}$$

which is approximately equal to ϕ for $|\phi - \theta| \ll c\sigma$ and departs slowly from the neighborhood of θ when $|\phi - \theta| \gg c\sigma$.

Another interesting possibility is to use the same type of operation on the modulus of the Fourier transform. That is, rather than substituting the measured Fourier modulus for the computed Fourier modulus, allow the Fourier modulus wander from the measured value according to the amount of noise present in the Fourier modulus data. Such an algorithm would reconstruct the phase from the modulus or the modulus from the phase depending on which has the higher signal-to-noise ratio at any given point in the Fourier domain.

132

REFERENCES

[6.1] T.R. Crimmins, J.R. Fienup, and B.J. Thelen, "Improved Object Support from Autocorrelation Support and Application to Phase Retrieval," accepted for publication in J. Opt. Soc. Am. A (1989).

[6.2] J.R. Fienup and A.M. Kowalczyk, "Phase Retrieval of a Complex-Valued Object Using a Low-Resolution Image," in Signal Recovery and Synthesis III, digest of papers (Optical Society of America, June 1989).

[6.3] B.L. McGlammery, "Computer Simulation Studies of Compensation of Turbulence Degraded Images," in J.C. Urbach, ed., Image Processing, Proc. SPIE 74, 225-233 (1976).

7.0 2-D SHEAR AVERAGING

Shear averaging is an algorithm invented at ERIM [7.1] originally for correcting one-dimensional (1-D) phase errors, as occur in synthetic aperture radar (SAR). Here we generalize it and apply it to the case of 2-D phase errors as would be encountered in imaging satellites as described in Section 6. In what follows it is seen that a 2-D extension to shear averaging is feasible if the phase errors are slowly varying.

7.1 2-D SHEAR AVERAGING THEORY

7.1.1 The 2-D Shear Averaging Algorithm

As in previous work [7.1], let the ideal Fourier transform be

$$F(u, v) = |F(u, v)| \exp[i\Psi(u, v)] \qquad (7\text{-}1)$$

and the actual, measured Fourier transform, with phase errors $\phi_e(u, v)$ be

$$G(u, v) = F(u, v) \exp[i\phi_e(u, v)] \qquad (7\text{-}2)$$

where $u = 0, 1, \ldots, N_o - 1$ and $v = 0, 1, \ldots, M_o - 1$. For these 2-D phase errors we form the shear average

$$S_{oa}(u, v) = \sum_{(u',v') \in B_{uv}} G(u', v') \, G^*(u', v' - a) \qquad (7\text{-}3)$$

where B_{uv} is a set of points (u', v') (the region of summation) centered at (u, v), and a is a lag smaller than the speckle size (correlation length) of F. More generally a weighted summation can be performed. Henceforth the symbol B under the summation means $(u', v') \in B_{uv}$.

135

In the earlier work [7.1] it was assumed that the phase error is one-dimensional (1-D), i.e., $\phi_e(u,v) = \phi_e(v)$. Then one can sum over one entire line, i.e., B_{uv} consists of (u',v), $u' = 1, 2, ..., N_o$, where N_o is the number of samples in the u-dimension. Then $S_{oa}(u,v) = S_a(v)$ is a function of v only and its phase can be summed to estimate $\phi_e(v)$ [7.1]. The next most complicated case is for the phase error to be 2-D but separable, i.e., $\phi_e(u,v) = \phi_{eu}(u) + \phi_{ev}(v)$. If one performs the summation of Eq. (7-1) again over one entire line, one again gets the same result as for the 1-D case: $S_{oa}(u,v) = S_a(v)$ is a function of v only and its phase can be summed to estimate $\phi_{ev}(v)$. Similarly the phase of $S_{bo}(u)$ [see Eq. (7-8)] can be summed to estimate $\phi_{eu}(u)$. Consequently the separable case can easily by handled as two 1-D problem with errors in each dimension the same as for the 1-D case [7.1]. In what follows we consider the fully 2-D case.

If the fully 2-D phase error $\phi_e(u,v)$ is smoothly varying, then we can consider a region of summation B_{uv} having an area over which ϕ_e can be approximated by a Taylor-series expansion including only linear terms:

$$\phi_e(u', v') = \phi_e(u, v) + c_{10}(u, v) (u' - u) + c_{01}(u, v) (v' - v) . \quad (7\text{-}4)$$

(Later we will consider the effect of higher-order terms.) Inserting Eqs. (7-2) and (7-4) into Eq. (7-3) and simplifying yields

$$S_{oa}(u, v) = \exp[ia\, c_{01}(u, v)] \sum_B F(u', v') F^*(u', v' - a) . \quad (7\text{-}5)$$

As in the 1-D case [7.1], provided that the area of summation is large enough, we can approximate the summation by the ensemble average

$$J(0, a) = I\, \mu(0, a) = \langle F(u', v') F^*(u', v' - a)\rangle \quad (7\text{-}6)$$

136

where $J(\Delta u, \Delta v)$, the mutual intensity, is the Fourier transform of the underlying incoherent image. Then we have

$$S_{oa}(u, v) \simeq \exp[ia \, c_{01}(u, v)] \, I \, \mu(0, a) \quad . \tag{7-7}$$

Similarly

$$S_{bo}(u, v) = \sum_{B} G(u', v') \, G^*(u' - b, v')$$

$$\simeq \exp[ib \, c_{10}(u, v)] \, I \, \mu(b, 0) \quad . \tag{7-8}$$

Then the phases of S_{oa} and S_{bo} are

$$\theta_{oa}(u, v) = a \, c_{01}(u, v) + \arg[\mu(0, a)] + 2\pi \, p_{oa}(u, v) \tag{7-9}$$

and

$$\theta_{bo}(u, v) = b \, c_{10}(u, v) + \arg[\mu(b, 0)] + 2\pi \, p_{bo}(u, v) \tag{7-10}$$

respectively, where p_{oa} and p_{bo} are integers that allow for the fact that the phase is computed modulo 2π. If the values of a and b are chosen to be small compared with the correlation distances of both μ and ϕ_e, then all the terms in Eqs. (7-9) and (7-10) will be small and $p_{oa} = p_{bo} = 0$. In the analysis that follows we will not make this assumption.

Since $\theta_{oa}(u, v)$ and $\theta_{bo}(u, v)$ represent phase derivatives, by integration over $\theta_{oa}(u, v)$ and $\theta_{bo}(u, v)$ one can arrive at an estimate of $\phi_e(u, v)$. This could be done, for example, by first integrating in the v direction for a fixed u, then integrating in the u direction for each value of v. The geometry and spacings of the regions of summation B_{uv} can take several forms. In what immediately follows we give a simple generic form that lacks detailed accuracy but explains the principal. For example, suppose B_{uv} is a rectangular area centered at (u, v) of length m_B in the v direction and n_B in the u direction. Then

137

we could compute $\hat{\phi}_e$ on a grid with spacings m_B and n_B by first summing in the v direction along u = 0:

$$\theta'_{oa}(0, 0) \equiv 0 \qquad (7\text{-}11a)$$

$$\theta'_{oa}(0, mm_B) = \sum_{m'=1}^{m} (m_B/a) \; \theta_{oa}(0, m'm_B)$$

$$= m_B \sum_{m'=1}^{m} c_{01}(0, m'm_B) + m(m_B/a) \; \arg[\mu(0, a)]$$

$$+ (m_B/a) \; 2\pi \sum_{m'=1}^{m} p_{oa}(0, m'm_B a) \quad . \qquad (7\text{-}11b)$$

Next, for each v = mm_B we sum over u:

$$\hat{\phi}_e(nn_B, mm_B) = \theta'_{oa}(0, mm_B) + (n_B/b) \sum_{n'=1}^{n} \theta_{bo}(n'n_B, mm_B) \qquad (7\text{-}12a)$$

$$\simeq m_B \sum_{m'=1}^{m} c_{01}(0, m'm_B) + n_B \sum_{n'=1}^{n} c_{10}(n'n_B, mm_B)$$

$$+ m(m_B/a) \; \arg[\mu(0, a)] + n(n_B/a) \; \arg[\mu(b, 0)]$$

$$+ (m_B/a) \; 2\pi \sum_{m'=1}^{m} p_{oa}(0, m'm_B)$$

$$+ (n_B/b) \; 2\pi \sum_{n'=1}^{n} p_{bo}(n'n_B, mm_B) \quad . \qquad (7\text{-}12b)$$

As long as (m_B/a) and (n_B/b) are integers, then the last two summations add integer 2π phase which is unimportant and can be ignored. The $m(m_B/a) \; \arg[\mu(0, a)] + n(n_B/a) \; \arg[\mu(b, 0)]$ are linear phase terms which shift the image but do not cause blurring, and so they can be ignored. The first two terms $m_B \Sigma c_{01}(0, m'm_B) + n_B \Sigma c_{10}(n'n_B, mm_B)$ are

sums over the derivative of the phase error which should give a good approximation to ϕ_e as long as Eq. (7-4) is accurate over each B_{uv}.

Two sources of error cause inaccuracies in $\hat{\phi}_e$: (1) statistical errors in approximating the finite sum in Eqs. (7-7) and (7-8) by $\hat{I}\mu$ and (2) phase errors ϕ_e that have higher-order terms within the region of summation.

7.1.2 Residual Phase Error Due to Statistical Error

The residual phase error due to the approximation of the summation over the product of the F's by the ensemble average, which is the error of $\arg[\mu(0, a)]$ and $\arg[\mu(b, 0)]$, is similar to that in the 1-D case [7.1] and has standard deviation given by

$$\sigma_a = \frac{1}{\sqrt{2N_B}\ |\mu(0,\ a)|} \tag{7-13a}$$

and

$$\sigma_b = \frac{1}{\sqrt{2N_B}\ |\mu(b,\ 0)|} \tag{7-13b}$$

where in this case N_B is the number of independent samples of F in the region B. For region B of n_B by m_B samples, $N_B = (n_B/n_c)\ (m_B/m_c)$, where n_c by m_c is the size of an independent sample of $F(u,v)$. The estimate of the phase error across the width m_B would be $(m_B/a)\ \theta_{oa}$. Hence the variance of the phase error estimate across the width m_B is

$$(m_B/a)^2\ \sigma_a^2 = (m_B^2/a^2)\ n_c m_c/[(2n_B m_B)\ |\mu(0,a)|^2]$$

$$= m_B n_c m_c/\left[2a^2 n_B |\mu(0,a)|^2\right] \ . \tag{7-14}$$

If the total array size is $N_0 = Nn_B$ by $M_0 = Mm_B$, then the variance of the phase error at the far edge of the array, assuming the simple summation of Eq. (7-11), would be

$$\sigma_M^2 = \left(\frac{M_0}{m_B}\right) \frac{m_B n_c m_c}{2a^2 n_B \, |\mu(0,a)|^2} = \frac{M_0 n_c m_c}{2a^2 n_B \, |\mu(0,a)|^2} \qquad (7\text{-}15)$$

where it is assumed that the $M = (M_0/m_B)$ errors are uncorrelated over the sum.

A similar result, exchanging m's and n's, holds for summation in the orthogonal dimension, and so the variance of the error in the corner farthest from the beginning corner is

$$\sigma_{NM}^2 = \frac{M_0 n_c m_c}{2a^2 n_B \, |\mu(0,a)|^2} + \frac{N_0 n_c m_c}{2b^2 m_B \, |\mu(b,0)|^2} \ . \qquad (7\text{-}16)$$

for the simple summation approach.

Consider the case of $n_c = m_c = 2$ samples and $a = 1$. Then, from Eq. (7-15) we see that unless n_B is comparable to M_0, σ_M will be unacceptably large (much greater than one radian).

However, there are multiple paths to sum from $\hat{\phi}_e(0, 0)$ to $\hat{\phi}_e(Nn_B, Mm_B)$. Methods used to reconstruct 2-D phase functions from phase differences (least-squares solutions, for example) can be used here; then the variance of the residual phase error should be much less than that given by Eq. (7-16). Since 2-D least-squares methods reportedly yield a phase-error estimate that has an error comparable to the error in a single phase-error difference estimate, the variance of the 2-D phase error estimate should be similar to that of Eq. (7-14).

Note from Eq. (7-15) that the statistical error of the simple 1-D summation is independent of m_B. Therefore, as far as that error is concerned, the width of B_{uv} can be anything one desires. Since using a narrow B_{uv} will reduce the effects of nonlinearities in ϕ_e (which are analyzed later), it seems that to compute $S_{oa}(u,v)$ one would want to use B_{uv} of width one sample in the v dimension by n_B samples in the u dimension, where n_B is the greatest length that does not run into severe nonlinearity problems. On the other hand, to compute $S_{bo}(u,v)$ one would want B_{uv} to be of width m_B samples in the v dimension (the largest m_B that avoids severe nonlinearity problems) by one sample in the u dimension. Thus we are lead to using very different sets of points B_{uv} for the summation of S_{oa} and S_{bo}, and different sampling grids would result as well.

In order to arrive at a rectangular grid from which we could proceed with a least squares solution, we could first sum across blocks of width m_B of the θ_{oa} and down blocks of width n_B of θ_{bo} to get samples on a grid with spacings n_B by m_B. The variance of the phase error across a block of width m_B is given by Eq. (7-14). Take the difference between the phase values at the beginning and end of each block to estimate the phase difference between those two points. These would have the same variances as mentioned above. Then we could proceed with the least squares solution.

However, from Eq. (7-14) we see that when summing over just a single block of width m_B, the variance of the error is proportional to m_B. Therefore it would be best, when using a least-squares summation, to sum over narrow blocks to reduce the statistical error as well as the nonlinearity error. This would suggest summing over blocks of width m_c for θ_{oa} and of width n_c for θ_{bo}. If the normal assumptions about the least-squares phase reconstruction were true, then the 2-D phase estimate variances would be

$$\left[m_c/a\right]^2 \sigma_a^2 = n_c m_c^2 / \left[2a^2 n_{..} |\mu(0,a)|^2\right] \qquad (7\text{-}17a)$$

for the v dimension for which $N_B = (n_B/n_c) \times 1$, and

$$\left[n_c/b\right]\sigma_b^2 = n_c^2 m_c / \left[2b^2 m_B |\mu(b,0)|^2\right] \qquad (7\text{-}17b)$$

for the u dimension, for which $N_B = 1 \times (m_B/m_c)$. However, this ignores the fact that the error of $\theta_{oa}(u,v)$ is correlated over n_B samples in the u dimension and $\theta_{bo}(u,v)$ is correlated over m_B samples in the v dimension. Consequently, the variance of the 2-D phase error estimate may be closer to $n_c m_c / [2a^2 |\mu(0,a)|^2]$. A further refinement of this analysis will be necessary to arrive at a more precise statement of the residual phase error for the 2-D case.

7.1.3 Convolutional Processing

An alternative processing scheme is suggested by Eq. (7-3), which is essentially a convolution of $G(u', v') G^*(u', v' - a)$ with B_{oo}. Letting the functional representation of B_{uv} be

$$B_{uv}(u', v') = \begin{cases} 1 & \text{for } (u', v') \in B(u, v) \\ 0 & \text{for } (u', v') \notin B(u, v) \end{cases}$$

$$= B_{oo}(u' - u, v' - v) , \qquad (7\text{-}18)$$

Eq. (7-3) can be written

$$S_{oa}(u, v) = \sum_{u',v'} B_{oo}(u' - u, v' - v) G(u', v') G^*(u', v' - a)$$

$$= [G(u,v) G^*(u, v - a)] \circledast B_{oo}(u,v) \qquad (7\text{-}19)$$

where $\otimes$ denotes cross-correlation. More generally, $B_{00}(u', v')$ could be a nonbinary function. A cross-correlation can be computed by two FFT's, a product, and an inverse FFT. For B_{uv} covering just a small area, direct cross-correlation is more efficient than the FFT method. By this approach, then, one arrives at $S_{oa}(u, v)$ for each sample of (u, v) [and similarly $S_{bo}(u, v)$], not just for the coarse grid (nn_B, mm_B). Integrating or performing a least-squares fit over this fine sampling of the phase derivative is an alternative to the use of the coarser grid.

7.1.4 Residual Phase Error Due to Higher-Order Phase Errors

The residual phase errors given by Eq. (7-14) consider only the result of averaging over a finite number of pixels to estimate the ensemble average. A second source of error is the fact that the phase errors are not constant over the area of integration. In what follows is analysis of that component of the residual phase error.

Now consider phase errors of the more general form

$$\phi_e(u', v') = \sum_{j,k=0} c_{jk}(u, v) (u' - u)^j (v' - v)^k \qquad (7\text{-}20)$$

where

$$c_{00}(u, v) = \phi_e(u, v) \qquad (7\text{-}21)$$

for the region $B(u, v)$. Inserting Eq. (7-20) into Eq. (7-3) yields

$$S_{oa}(u, v) = \sum_B G(u', v') G^*(u', v' - a)$$

$$= \sum_B F(u', v')\, F^*(u', v' - a)$$

$$\exp i\left[\sum_{j,k} c_{jk}(u, v)\, (u' - u)^j\, (v' - v)^k \right.$$

$$\left. - \sum_{j,k} c_{jk}(u, v)\, (u' - u)^j\, (v' - v - a)^k\right]$$

$$= \sum_B F(u', v')\, F^*(u', v' - a)\, \exp i\left\{\sum_{j,k} c_{jk}(u, v)\, (u' - u)^j \right.$$

$$\left. [(v' - v)^k - (v' - v - a)^k]\right\}$$

$$= \sum_B F(u', v')\, F^*(u', v' - a)\, \exp i\left\{\sum_{j,k} c_{jk}(u, v)\, (u' - u)^j \right.$$

$$\cdot\, [k(v' - v)^{k-1}\, a - \binom{k}{2}(v' - v)^{k-2}\, a^2 + \ldots$$

$$\left. + (-1)^{k-1}\, a^k]\right\} \tag{7-22}$$

where

$$\binom{k}{n} = \frac{k!}{n!(k - n)!} \quad . \tag{7-23}$$

That is, the phase error term $c_{jk}(u, v)\, (u' - u)^j\, (v' - v)^k$ results in phase terms in $S_{oa}(u, v)$ that are jth order in u' and $(k - 1)$th, $(k - 2)$th, ... order in v'. In particular all terms in ϕ_e that are zero-order (constant) in v ($k = 0$) disappear, and are therefore inconsequential.

Specifically, consider the phase error terms through cubic:

$$\phi_e(u', v') = \phi_e(u, v) + c_{10}(u' - u) + c_{01}(v' - v) + c_{20}(u' - u)^2$$

$$+ c_{11}(u' - u)(v' - v) + c_{02}(v' - v)^2$$

144

$$+ c_{30}(u' - u)^3 + c_{21}(u' - u)^2(v' - v)$$

$$+ c_{12}(u' - u)(v' - v)^2 + c_{03}(v' - v)^3 \quad (7\text{-}24)$$

where $c_{jk} = c_{jk}(u, v)$. Then

$$S_{oa}(u, v) = \sum_{B} F(u', v') F^*(u', v' - a)$$

$$\exp i\Big\{c_{01} a + c_{11}(u' - u) a + c_{02} [2a(v' - v) - a^2]$$

$$+ c_{21}(u' - u)^2 a + c_{12}(u' - u) [2a(v' - v) - a^2]$$

$$+ c_{03} [3a(v' - v)^2 - 3a^2(v' - v) + a^3]\Big\}$$

$$= \exp i(c_{01} a - c_{02} a^2 + c_{03} a^3)$$

$$\sum_{B} F(u', v') F^*(u', v' - a)$$

$$\exp i\Big\{c_{11} a(u' - u) + 2 c_{02} a(v' - v)$$

$$+ c_{21} a(u' - u)^2$$

$$+ c_{12}(u' - u) [2a(v' - v) - a^2]$$

$$+ c_{03}[3a(v' - v)^2 - 3a^2(v' - v)]\Big\} \quad . \quad (7\text{-}25)$$

Now make one further assumption. Suppose that when the summation is replaced by an ensemble average over the realizations of F, we can treat the phase error terms as being statistically independent of the F so we can replace Eq. (7-25) by

$$S_{oa}(u, v) \simeq I\, \mu(0, a)\, \exp i(c_{01}\, a - c_{02}\, a^2 + c_{03}\, a^3)$$

$$\sum_B \exp i\Big\{c_{11}\, a(u' - u) + 2\, c_{02}\, a(v' - v)$$

$$+ c_{21}\, a(u' - u)^2 + c_{12}(u' - u)\, [2a(v' - v) - a^2]$$

$$+ c_{03}[3a(v' - v)^2 - 3a^2(v' - v)]\Big\} \quad . \qquad (7\text{-}26)$$

Now further suppose that $B_{oo}(u', v')$ is symmetric in u' and in v' and separable in u' and v'. Then, individually, terms in Eq. (7-26) that are odd in $(u' - u)$ or $(v' - v)$ will have integrals (sums) of their imaginary part that will be zero (making the integral have zero phase) and no undesired phase terms will result. Consequently, of the phase error terms explicitly shown in Eq. (7-24), the single terms that cause undesired phase errors in the summation of Eq. (7-26) are those having coefficients c_{21} and c_{03}. If we assume small phase error contributions due to these terms, we can approximate

$$\sum_B \exp i\Big[c_{21}\, a(u' - u)^2 + c_{03}\, 3a(v' - v)^2\Big]$$

$$\simeq \sum_B \Big[1 + ic_{21}\, a(u' - u)^2 + ic_{03}\, 3a(v' - v)^2\Big]$$

$$\simeq n_B m_B + im_B\, c_{21}\, a \int_{-n_B/2}^{n_B/2} u'^2\, du' + in_B\, c_{03}\, 3a \int_{-m_B/2}^{m_B/2} v'^2\, dv'$$

$$= n_B m_B + im_B^3\, c_{21}\, an_B/12 + in_B^3\, c_{03}\, 3a\, m_B/12$$

$$= n_B m_B\Big[1 + ic_{21}\, an_B^2/12 + ic_{03}\, am_B^2/4\Big]$$

$$\simeq n_B m_B\, \exp i\Big[c_{21}\, an_B^2/12 + c_{03}\, am_B^2/4\Big] \quad . \qquad (7\text{-}27)$$

Therefore for ϕ_e with terms up to cubic over B, the phase of $S_{oa}(u, v)$ is given approximately by

$$\theta_{oa}(u, v) \simeq \arg[\mu(0, a)] + c_{01}\, a - c_{02}\, a^2 + c_{03}\, a\left(a^2 + m_B^2/4\right)$$

$$+ c_{21}\, a n_B^2/12 + 2\pi\, p_{oa}(u, v) \qquad (7\text{-}28)$$

(where the c_{jk} are functions of u and v).

If we ignore the fact that there are higher-order phase errors and take this phase to be due to the linear component only, then the phase difference across B will be taken to be

$$(m_B/a)\, \theta_{oa}(u, v) = (m_B/a)\, \arg[\mu(0, a)] + c_{01}\, m_B - c_{02}\, m_B\, a$$

$$+ c_{03}\, m_B(a^2 + m_B^2/4) + c_{21}\, m_B\, n_B^2/12$$

$$+ (m_B/a)\, 2\pi\, p_{oa}(u, v) \quad . \qquad (7\text{-}29)$$

At this point consider what the actual phase difference across the center of B is in the v direction. For $u' = u$, we have, from Eq. (7-24),

$$\phi_e(0, v \pm m_B/2) = \phi_e(u, v) + c_{01}(\pm m_B/2) + c_{02}(\pm m_B/2)^2 + c_{03}(\pm m_B/2)^3.$$

$$(7\text{-}30)$$

Therefore

$$\phi_e(u, v + m_B/2) - \phi_e(u, v - m_B/2) = c_{01}\, m_B + c_{03}\, m_B^3/8 \quad . \quad (7\text{-}31)$$

The residual error, the difference between Eqs. (29) and (31), ignoring $(m_B/a)\, \arg[\mu(0, a)]$ and the $2\pi p$ terms, is

res. error $= - c_{02} \, m_B \, a + c_{03} \, m_B (a^2 + m_B^2/8) + c_{21} \, m_B \, n_B^2/12$. (7-32)

Of these terms, $-c_{02} m_B a$ will probably be the worst since its coefficient will ordinarily be the largest.

The last source of error that we will consider here are the odd-function errors in Eq. (7-26) that were dropped because they added nothing to the phase-error estimate. Their deleterious effect is to reduce the magnitude of the summation over B, thereby reducing the signal-to-noise ratio. For example, the first term taken by itself would yield

$$\sum_B \exp \left[i c_{11} a(u'-u) \right] = m_B \int_{-n_B/2}^{n_B/2} \exp(i c_{11} a u') \, du'$$

$$= \pi \, m_B n_B \, \text{sinc} \left[c_{11} a n_B/(2\pi) \right] \qquad (7\text{-}33)$$

which would go to zero for $c_{11} a n_B = 2\pi$. Therefore, the contribution of such terms to ϕ_e over B must be considerably less than 2π in order to avoid a significant loss in signal-to-noise ratio.

To minimize the residual phase errors in Eq. (7-32) due to higher-order phase errors, we would want to choose small values for m_B and n_B, whereas to minimize the residual phase errors due to the statistics [see Eq. (7-16)] we would want to maximize m_B and n_B. The optimum trade-off, which depends on the spatial statistics of ϕ_e, should be determined. Another possibility is to perform the phase error correction recursively. Depending upon how $\hat{\phi}_e$ is corrected in-between the coarse sampling grid (i.e. what form of interpolation is used), some of the higher-order terms may be reduced. Then a second pass of the algorithm may improve the result.

148

It is also possible to reduce these errors substantially with more complex processing. If we use the convolutional method for computing $S_{oa}(u, v)$ at the finer sampling grid, then with closely-spaced samples of $S_{oa}(u, v)$ we can estimate the quadratic coefficient c_{02} and compensate for it appropriately. Extensions to this approach could be used to reduce other higher-order terms as well, including cross-terms such as c_{21}. The area of optimally using the data $S_{ba}(u, v)$ to estimate $\phi_e(u \quad v)$ is probably a very rich area in which great improvements could be made. One should investigate least-squares and bispectrum-like approaches, for example.

In the derivations given here we estimated edge-to-edge phase errors across the regions B, but then corrected them on a center-to-center basis. Therefore the correction equations need to be modified to account for this effect.

7.2 COMPUTER SIMULATION AND RECONSTRUCTION EXPERIMENTS

Based on the theory presented in Section 7.1, three types of spatial-frequency summations were implemented, as illustrated in Figure 7-1.

Given $S_{oa}(u,v)$ and $S_{ho}(u,v)$, estimates of phase error differences from the integrations, the method we used for reconstructing the phase error was the complex exponential phase reconstruction algorithm shown in Figure 7-2, which is taken from Reference 7.2. In that figure Pmn is equivalent to $\exp[i\hat{\phi}_e(m,n)]$, $D_u mn$ is equivalent to $S_{bo}(u,v)$, and $D_v mn$ is equivalent to $S_{oa}(u,v)$. First a simple product (phase summation) is performed along each of the two axes, then the interior points are built up recursively using a summation over two paths. Next several iterations are performed. In one iteration, each value is replaced by a summation of values taken from the four nearest neighbors. The order of the selection of the values is in an outward spiral: first a clockwise spiral, then a counterclockwise spiral. In
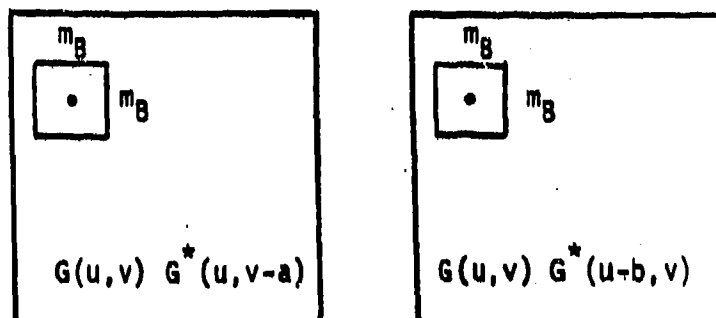
149

INTEGRATION GEOMETRIES

Case 1

Integrate over $1 \times m_B$.
Using each pixel,
Reconstruct $M \times M$ array.

$G(u,v)\ G^{*}(u,v-a)$ For $S_{oa}(u,v)$

$G(u,v)\ G^{*}(u-b,v)$ For $S_{bo}(u,v)$
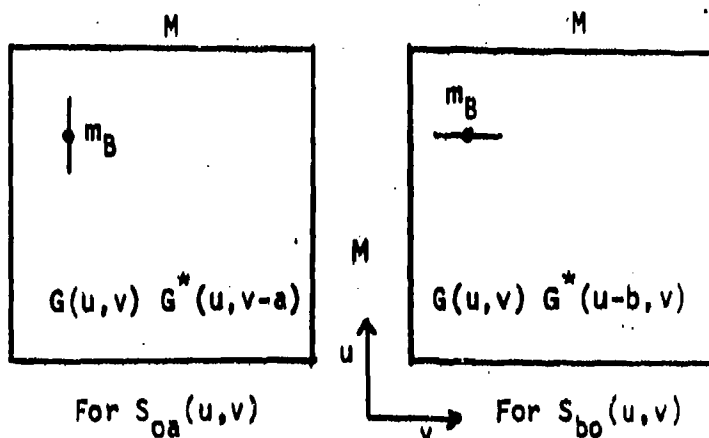
Case 2

Integrate over $m_B \times m_B$.
Using each pixel,
Reconstruct $M \times M$ array.

$G(u,v)\ G^{*}(u,v-a)$

$G(u,v)\ G^{*}(u-b,v)$

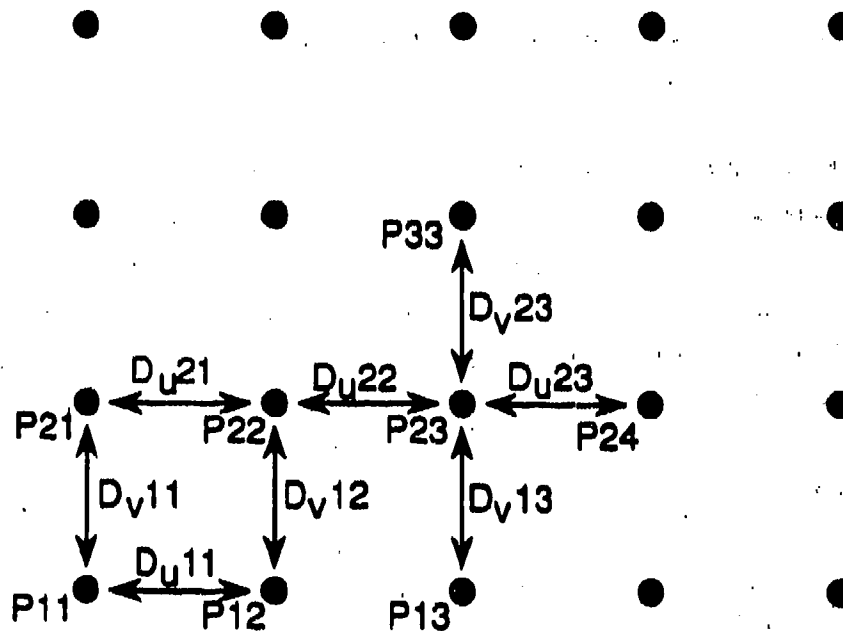**Case 3**

Integrate over $m_B \times m_B$ (like Case 2).
Using each $m_B \times m_B$th pixel,
Reconstruct $(M/m_B) \times (M/m_B)$ array from $(m_B/a)\ S_{oa}$ and $(m_B/a)\ S_{bo}$.
Interpolate to $M \times M$ array

FIGURE 7-1.   INTEGRATION GEOMETRIES FOR 2-D SHEAR AVERAGING.

COMPLEX EXPONENTIAL PHASE
RECONSTRUCTION

First estimate:

$P11 = 1$
$P12 = D_u 11\ P11/|P12|$
$P22 = (D_u 21\ P21 + D_v 12\ P12)/|P22|$
etc.

Iteration Example:

$P23 = [D_u 22\ P22 + D_v 13\ P13$
$\qquad\qquad + D_u^* 23\ P24 + D_v^* 23\ P33]/|P23|$

etc.

FIGURE 7-2. COMPLEX EXPONENTIAL PHASE RECONSTRUCTOR.

Figure 7-2, the division by |Pmn| on the right-hand side is to be interpreted as: first compute the right-hand side without |Pmn|, then divide it by its magnitude to arrive at a pure-phase function (a phase exponential).

Figure 7-3 shows a case for which the object is a delta function and the phase error is that shown in Figure 7-3(a), with $\sigma = \pi/2$ and corl=30. For display of phases, $-\pi$ is black, π is white, and the phase is wrapped (modulo 2π). The impulse response for this phase error is shown in Figure 7-3(g). The phases and magnitudes of S_{oa} and S_{bo} for Case 1 integration (see Figure 7-1) with $m_B = 8$ are shown in Figures 7-3(b)-(e). The phase-error estimate, reconstructed by shear averaging in conjunction with the reconstructor shown in Figure 7-2, is shown in Figure 7-3(f). From this it can be seen that the reconstructed phase error is similar to a smoothed version of the true phase error. The smoothing is due to the value of m_B. Figure 7-3(h) shows the impulse response due to the residual phase error gotten by subtracting the estimated phase error from the true phase error. From this it is seen that subtracting the phase error estimate removes most of the error.

Figure 7-4(a) shows the complex-valued object used for the experiments that follow. Figures 7-4(b), (c) show the magnitude and phase of the Fourier transform of the object. Figure 7-4(d) shows the added phase error ($\sigma = \pi/2$ and corl = 30). Figure 7-4(e) shows the given noisy phase [(c) plus (d), modulo 2π], and Figure 7-4(f) shows the blurred image obtained using the noisy phase.

Figure 7-5 shows a reconstruction experiment similar to that shown in Figure 7-2, with a case-1 integration (see Figure 7-1) with $m_B = 8$. Comparison of the original object in (a) with the blurred image in (c) and the reconstructed image in (h) shows that 2-D shear averaging corrected some of the phase error, but left a large residual phase error. Figure 7-6 shows the same thing for $m_B = 32$, and Figure 7-7 shows the same thing for a case-2 integration (see Figure 7-1) for $m_B = $
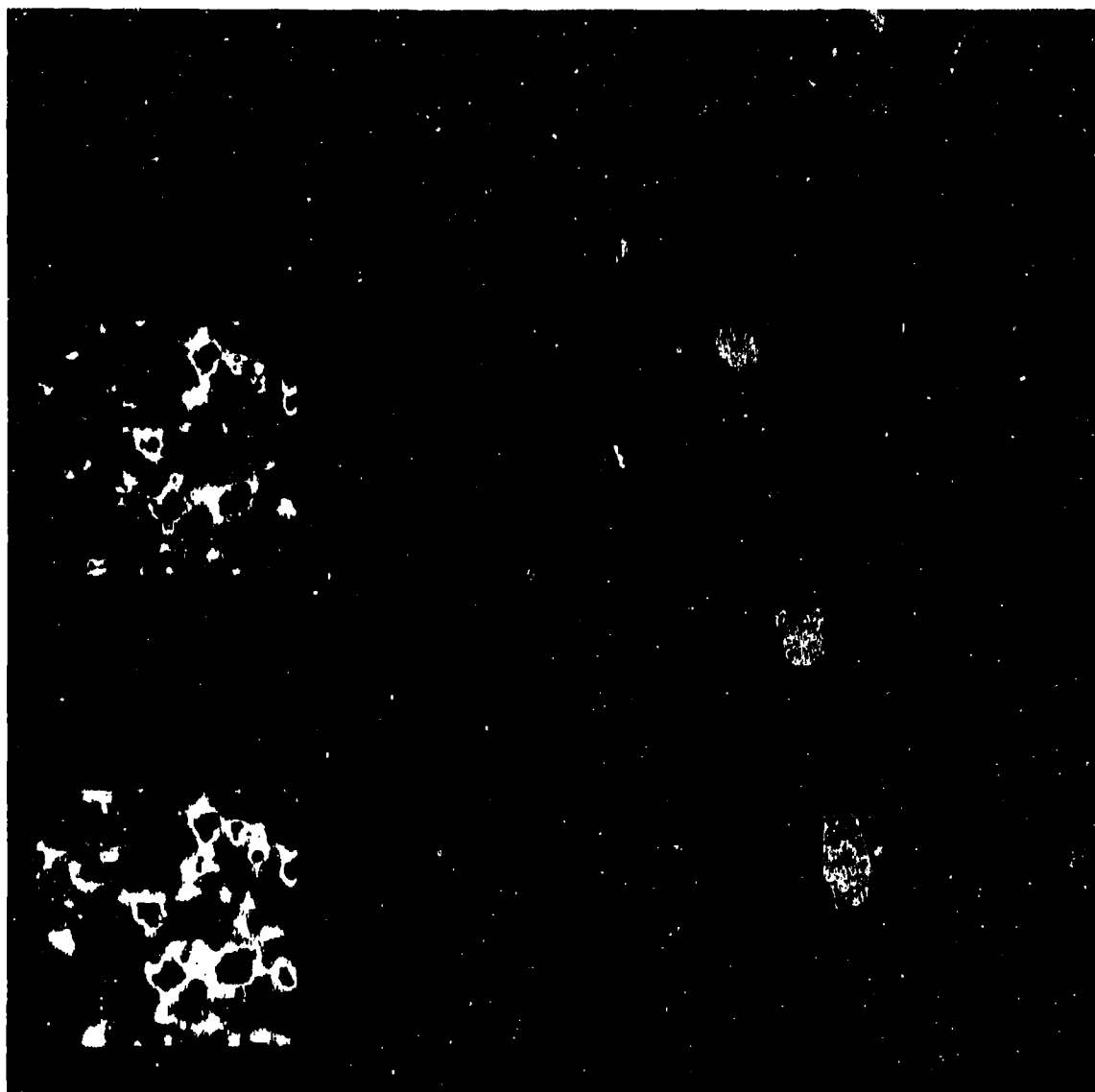
FIGURE 7-3. PHASE ERROR RECONSTRUCTION BY 2-D SHEAR AVERAGING FOR A POINT-SOURCE OBJECT. (a) Phase error function (modulo 2π); (b), (c) phase of S_{bo}, S_{oa}; (d), (e) magnitude of S_{bo}, S_{oa}; (f) reconstructed phase; (g) impulse response from (a); (h) impulse response from (a) minus (f).
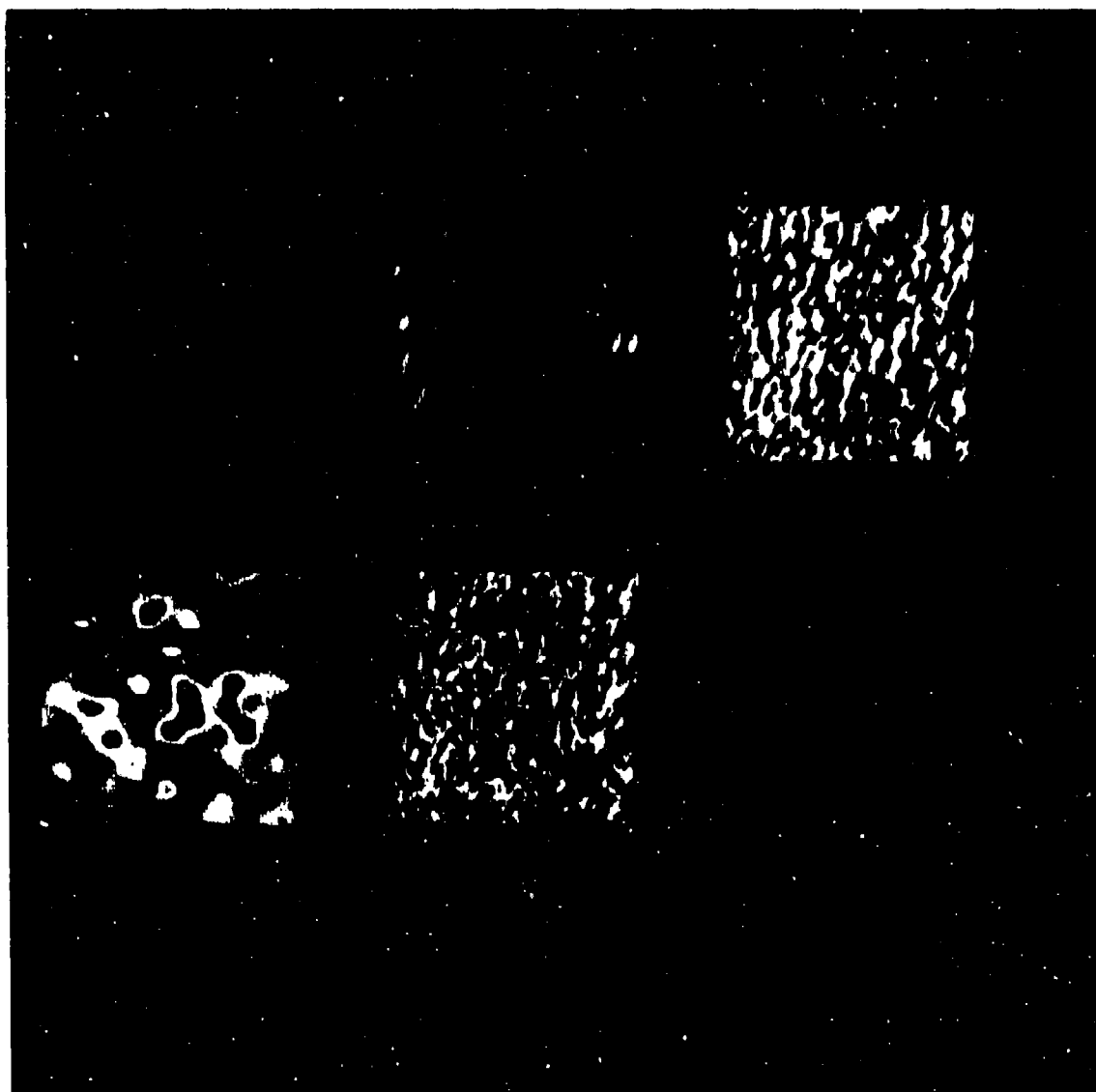
FIGURE 7-4. DATA USED IN 2-D SHEAR AVERAGING RECONSTRUCTION
EXPERIMENTS. (a) Object; (b), (c) object's Fourier magnitude and
phase; (d) phase error; (e) noisy phase estimate [(c) plus (d), modulo
2π]; (f) image blurred by the phase error.
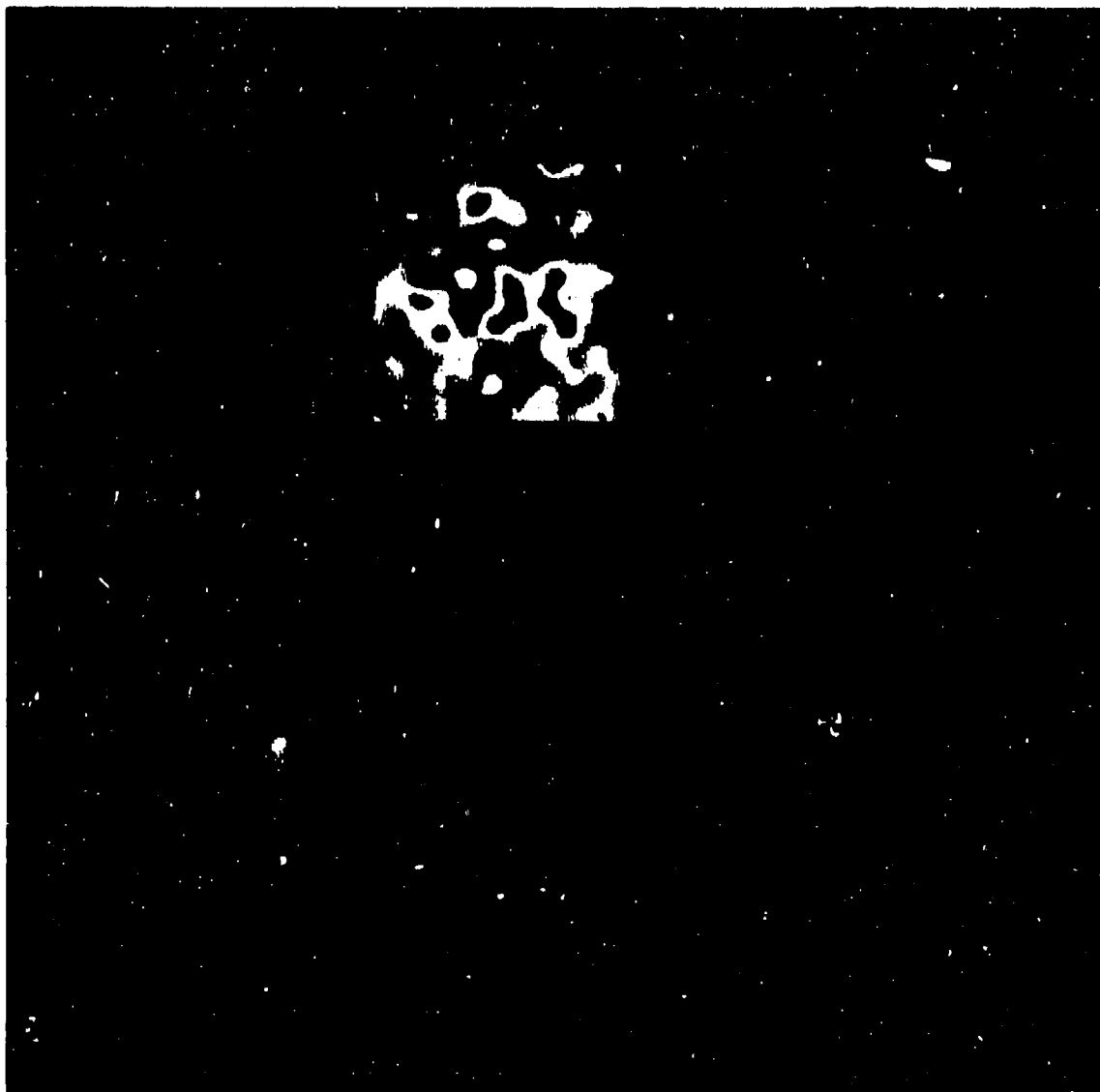
FIGURE 7-5. PHASE ERROR CORRECTION BY 2-D SHEAR AVERAGING. Case-1 integration and $m_B = 8$ were used. (a) The object; (b) the phase error; (c) the blurred image; (d), (e) the phase of S_{bo}, S_{oa}; (f), (g) the magnitude of S_{bo}, S_{oa}; (h) the image reconstructed after 2-D shear averaging.

FIGURE 7-6. PHASE ERROR CORRECTION BY 2-D SHEAR AVERAGING. Same as Figure 7-5, except $m_B = 32$ was used.
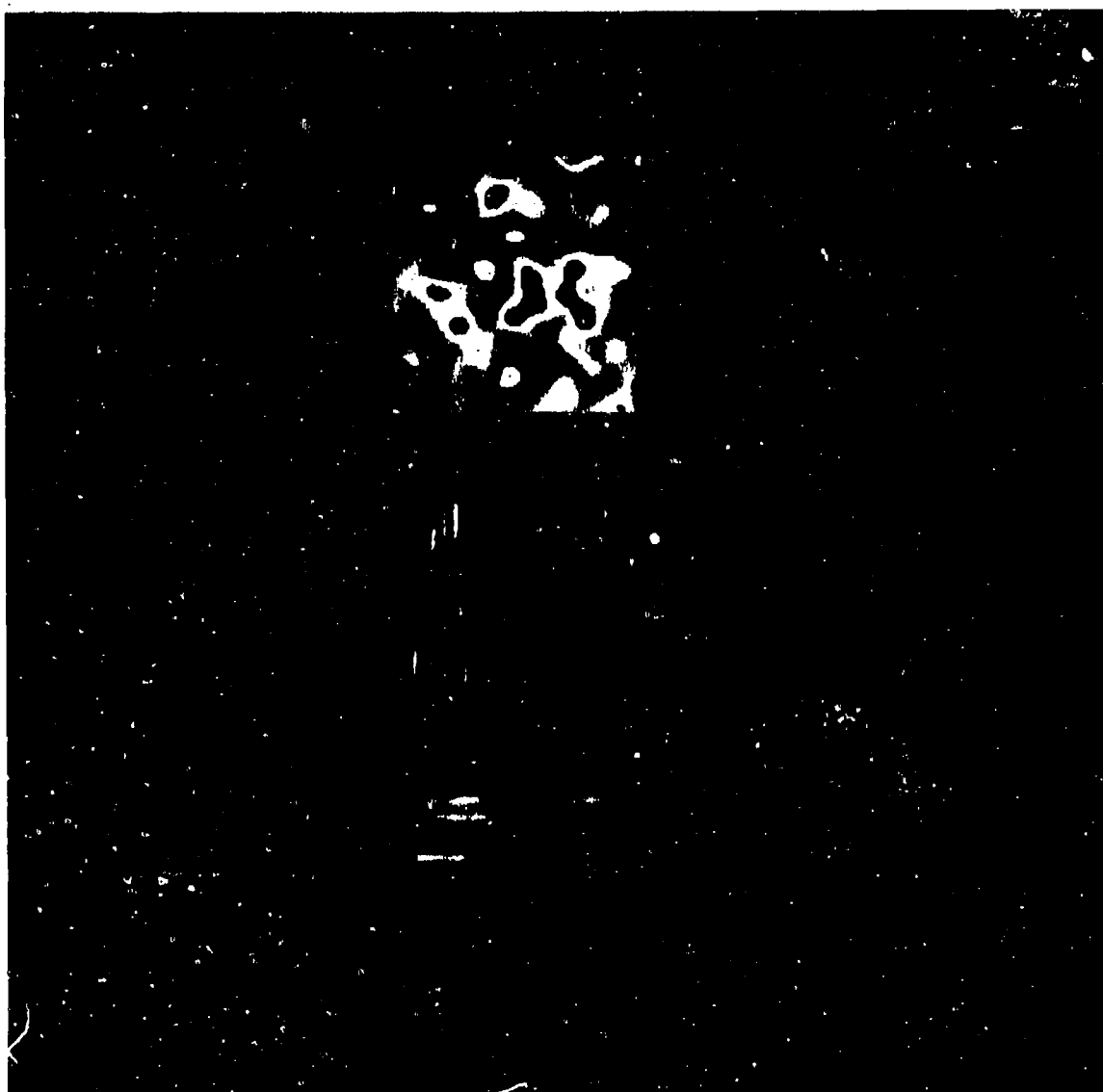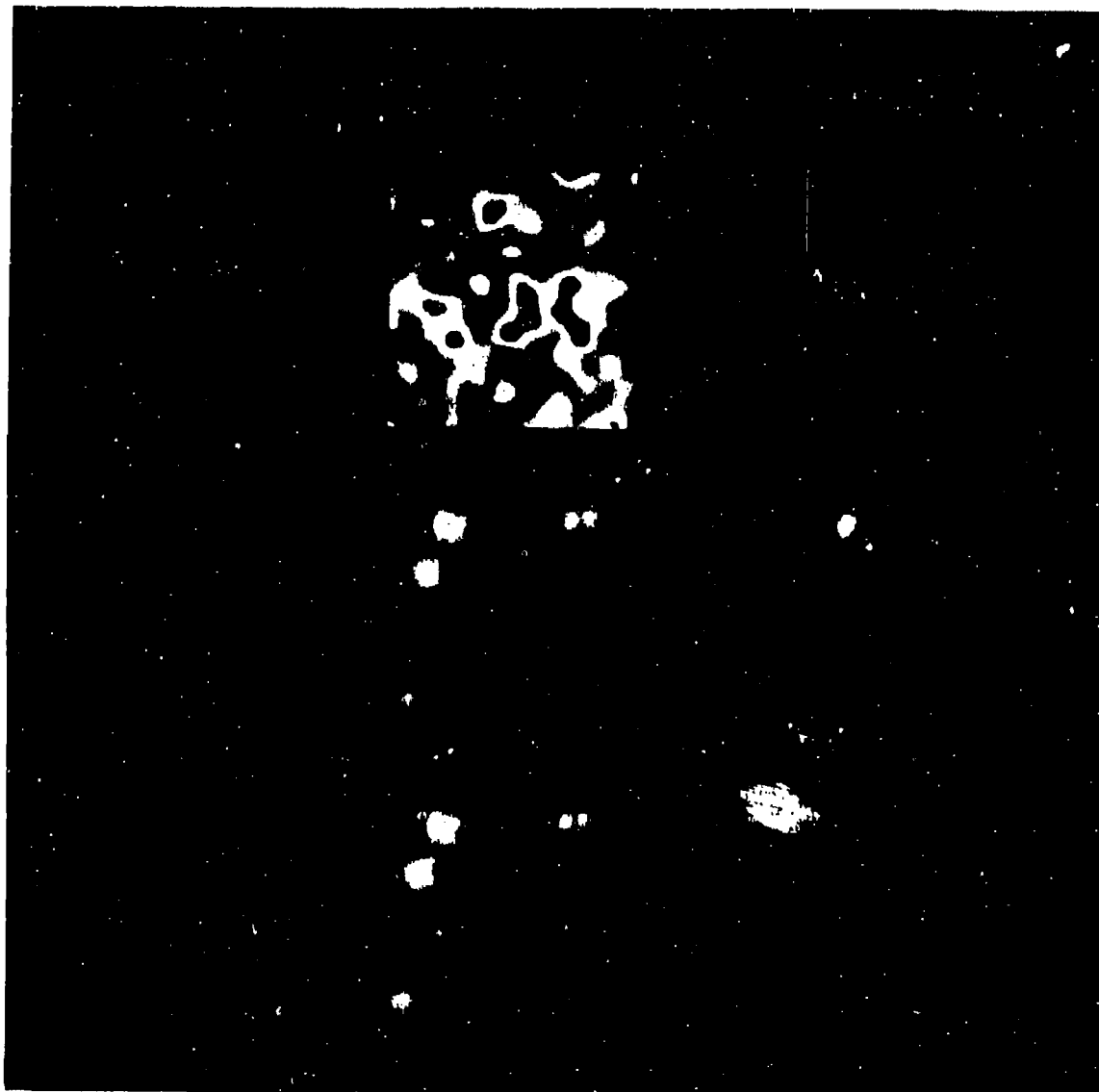
FIGURE 7-7. PHASE ERROR CORRECTION BY 2-D SHEAR AVERAGING. Same as Figure 7-5, except case-2 integration and $m_B = 32$ was used.

16. Of these, the case-1 integration with $m_B = 32$ appears to yield the best image for this example. Larger values of m_B cause the integration to be over an area over which the phase error varies too wildly, whereas smaller values of m_B cause the integration to be over a smaller region, increasing the statistical error. Comparing Figure 7- 5(c) with 7-5(h) shows that 2-D shear averaging improves the quality of the image substantially, but far from perfectly.

REFERENCES

[7.1] J.R. Fienup, "Phase Error Correction by Shear Averaging," in Signal Recovery and Synthesis III, digest of papers (Optical Society of America, June 1989).

[7.2] P. Nisenson, "Speckle Imaging with the PAPA Detector and the Knox-Thompson Algorithm," in D.M. Alloin and J.-M. Mariotti, eds., Diffraction-Limited Imaging with Very Large Telescopes, Sept. 13-22, 1988 (Kluwer Academic Publisher, Boston, 1989).

8.0 SPACE OBJECT IMAGING SENSORS

This section describes a first rough cut at comparing the numerous potential sensors for imaging space objects in earth orbit from the ground using short (visible or near-IR) wavelengths. Because no extensive investigations were performed to compare the various imaging approaches, what is contained in this section should not be considered to be a recommendation of one approach over another; rather, this should be viewed as an off-the-cuff listing of attributes and as only a first step toward comparing the various approaches. There is a need to perform a thorough analysis comparing these numerous candidate systems; this was beyond the scope of the present program, but it is recommended that such an analysis be performed to establish the basis for development of future fine-resolution imaging systems. This comparison is done primarily by means of the three matrix charts shown in Figures 8-1 to 8-3. Figure 8-1 covers the case of using only laser illumination, Figure 8-2 covers the case of using only incoherent illumination (or emissive objects), and Figure 8-3 covers mixed-coherence (coherent/incoherent) methods and other miscellaneous approaches. Further additions to the matrix could be made.

The Near-Team Feasibility column indicates our opinion of the feasibility of performing a successful experiment with present-day technology using an existing single-aperture telescope within the next six months. A successful experiment would be one in which the resolution of the reconstructed image is several times better than ($\lambda R/r_0$) at the object without the use of adaptive optics, where λ = wavelength, R = range to targ(and r_0 = Fried's parameter ($\sim$10cm). The Large Distributed Aperture column comments on the difficulty of putting together electro-optical hardware for a large distributed array of apertures suitable for imaging geosynchronous objects.

S.O.I. SENSORS USING COHERENT LASER ILLUMINATION ONLY

Sensor for Coherent Laser Illumination	Image Type	Laser Source	Detector	Large Distributed Aperture	Phase Retrieval	Additional Special Advantages	Additional Special Disadvantages	Near-Term Feasibility
C1 Laser Conventional	$|f_a|^2$	long or short CL	focal plane	difficult	very difficult T			sensor yes, processing no
C2 Laser-Aperture-Plane	f_a	pulsed, long CL	aper. plane	easy	difficult unless glint I: triple correlation?			laser close, processing too unless glint
C3 Imaging Correlography	$|f_a|^2$	medium rep-rate pulsed, long CL	aper. plane	easy	easy	OTF aperture fill	need very very realization T	laser close, bad, red, only
C4 C2 + Heterodyne Detection	f_a	long CL	aper. plane, heterodyne T	easy	easier than C2	high SNR or less laser power	heterodyne at 10.6µm, not .5µm	no
C5 Laser Dual Plane (C1 + C2)	f_a	pulsed, long CL	focal plane + aper. plane	easy	easier than C2.			laser close, processing too unless glint
C6 Laser Adaptive Optics	$|f_a|^2$	long or short CL	focal plane, wavefront sensor T	very difficult	not needed	real time, highest SNR	no coherent atmospheric sensor T	no
C7 Laser SAR	f_a	long CL, wave form T	heterodyne T + wave form	not needed	I-D only	only small rotation needed.	no for non-rotating geo-synch.?	no

Symbols: f_a: complex-valued coherent (speckled) image (a^{th} realization)
$|f_a|^2$: incoherent image
CL: coherence length. Long CL is > (twice object depth)
TBD: to be determined
T: factor making approach unsuitable for near term

Notes: Wavefront sensors do not work with coherent light from extended targets.
Phase retrieval is much more difficult for sparse apertures unless have OTF fill.
For all: need midpulse length, detector integration) $\ll 1/(\omega_{maj} \cdot$ rotation rate).

FIGURE 8-1. S.O.I. SENSORS USING COHERENT LASER ILLUMINATION ONLY.

S.O.I SENSORS USING INCOHERENT ILLUMINATION ONLY

Sensor	Bandwidth Δλ/λ	Detector	Large Distributed Aperture	Phase Retrieval	Additional Special Advantage	Additional Special Disadvantage	Near-Term Feasibility
I1 Conventional Imaging (Long Exposure)	white	focal plane	difficult	unknown		low resolution only	low res. done
I2 Adaptive Optics (AO) with Atmosphere Sensor	white λ/(4 πro)	focal plane + atmosphere sensor	very difficult	not necessary	high SNR, real-time	most difficult hardware, atmos. sensor needs bright object	done
I3 Speckle Interferometry	r_o/D	focal plane	difficult	Knox-Thompson or triple-corr. + iter.xform	most flexible reconstruction	needs 10^2 to 10^3 atms. frames; needs reference star, speckle MTF compensation so-so	yes
I4 Aperture Plane Interferometry	1/(4w)	aper. plane	difficult	iter.xform	higher SNR for each frame at high light levels.	narrower band can't combine frames easily	yes
I4A Phase Closure	1/(4w)	extra optics & detectors	difficult	may or may not be needed		more difficult hardware, less light efficient	harder
I4B1 Grating Interferometer	2/R	extra te	2-D difficult,	iter.xform			harder
I4B2 + Atmosphere Sensor	λ/(4 πro)	sense atms.	1-D easier	not needed		1-D, needs rotation	
I4C Heterodyne Detection & Electronic Correlation	$\Delta\nu/\nu$ τ ~10^{-6}	het. T	easy	easy			no
I4D Triple Shearing Interferometry	1/(2N)	aper. plane	difficult	recursive		needs 10^2 to 10^3 atms. frames, large memory	no
I5 Phase Diversity	λ/(4 πro)	focal plane + defocus plane	difficult	gradient search			yes

Symbols: R = linear space-bandwidth product
θπ/λ = (optical path difference of aberrations)/wavelength
r_o/D = (Fried's parameter)/(aperture diameter)
τ·ν = factor making approach unsuitable for near term
iter.xform = iterative Fourier transform algorithm
TBD = to be determined

Notes: Illumination is solar, thermal (both have limited availability) or active incoherent
All images are incoherent, $|I_o|^2$
Get OTF fill
Assume fast (5 msec), intensified detector

FIGURE 8-2. S.O.I. SENSORS USING INCOHERENT ILLUMINATION ONLY.

MIXED-COHERENCE AND MISCELLANEOUS S.O.I SENSORS

Sensor	Image Type	Source	Detector	Large Distributed Aperture	Phase Retrieval	Additional Special Advantage	Additional Special Disadvantage	Near-Term Feasibility
S1 Laser Dual Plane with Incoherent Atmos. Sensor	f_m	pulsed laser, long CL + incoherent	focal plane, pupil plane, atmos. sensor	easy	C-S per aper. + inter-aper.			sensor close
S2 Laser Focal Plane with Incoherent Atmos. Sensor	f_m	pulsed laser, long CL + incoherent	focal plane, atmos. sensor	easy	iter.uform + inter-aper.		need shaped aperture	sensor close
S3 Time-Resolved with Tomography	$16\mu^2$	pulsed laser, dry CL	many, over wider area	easy	not needed		larger array	TBD
S4 Bistatic Pulsed Heterodyne Imaging	$16\mu^2$	pulsed lasers, long CL, fast rep. rate, scanning, λ_1, λ_2	large light bucket, GHz	easy	not needed	real time	very widely spaced lasers	TBD

Additional symbols: C-S = Gerchberg-Saxton algorithm.

FIGURE 8-3.   MIXED-COHERENCE AND MISCELLANEOUS S.O.I. SENSORS.

8.1 INCOHERENT-ONLY SENSORS

Several incoherent approaches, including both aperture-plane and focal-plane (astronomical speckle) interferometry are feasible. Of these, the one farthest along in development is speckle interferometry (I3) using either Knox-Thompson or triple correlation to obtain an initial image (or Fourier phase) estimate which is refined by the iterative transform algorithm. This would yield an incoherent image of the object. It requires hundreds to thousands of frames with different realizations of atmospheric turbulence, and requires measurements on a reference star through an atmosphere having the same statistics as the atmosphere through which the object is imaged. It is restricted to pre-dawn or post-dusk imaging while the sensor is in night-time but the object is sun illuminated.

An extension of this method to large distributed apertures for imaging geosynchronous satellites would be difficult due to a requirement of a common focal plane.

8.2 COHERENT-ONLY SENSORS

For imaging with coherent laser illumination only, all the approaches are risky. The least risky, in terms of image reconstruction, would be a combination of Laser Dual Plane (C5) with Imaging Correlography (C3). Figure 8-4 shows a flowchart of the data processing for this combined approach. Imaging Correlography is the collection of multiple aperture-plane speckle intensity patterns, power spectrum (or autocorrelation) averaging, and image reconstruction by the iterative transform algorithm to arrive at a moderate-resolution (ρ_m) incoherent image. The resolution is limited primarily by statistical averaging noise due to a finite number of realizations of the speckle patterns. The Laser Dual Plane method is the collection of both an aperture-plane and a focal-plane speckle intensity pattern, and processing by a Gerchberg-Saxton type algorithm to arrive at the
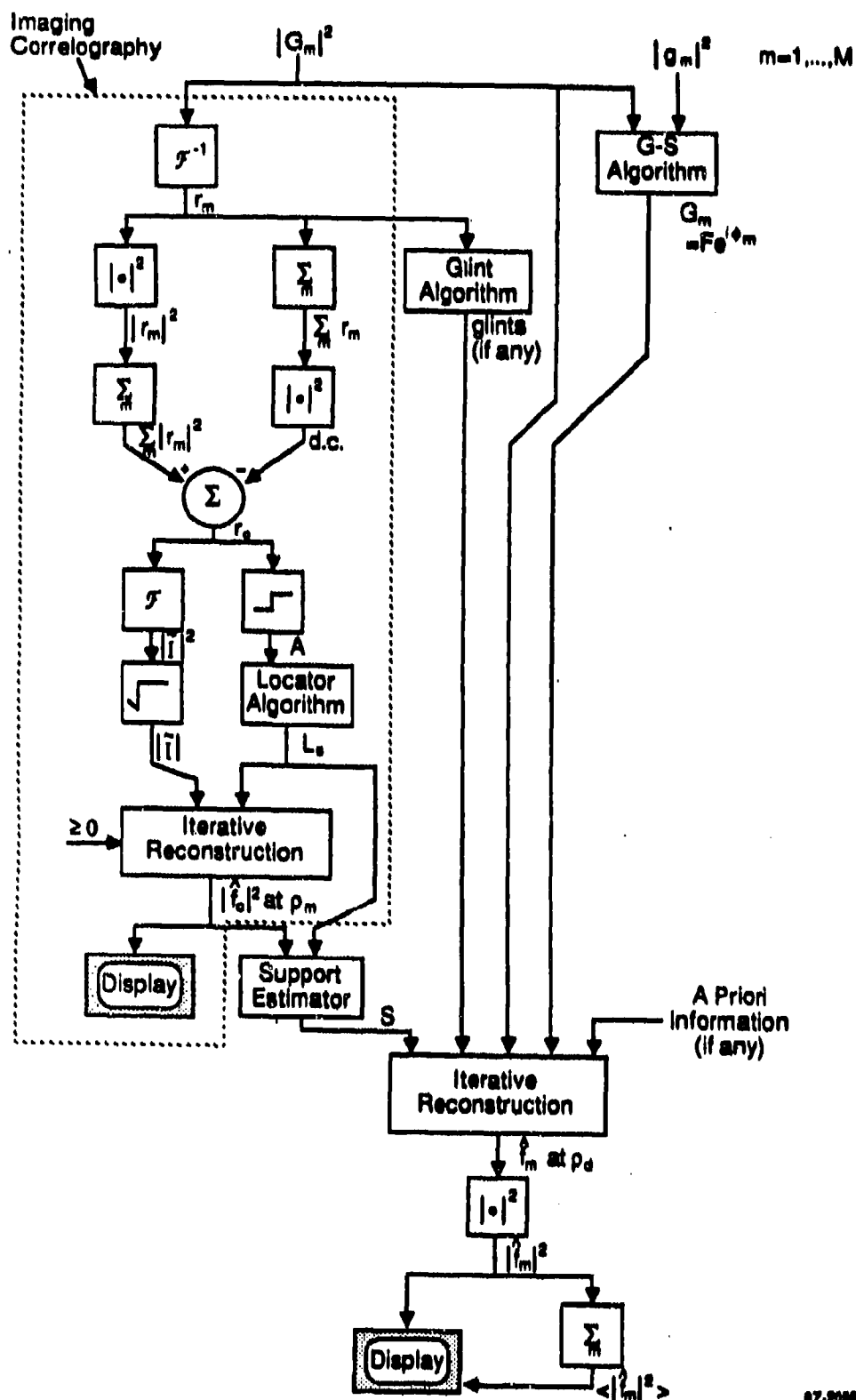
FIGURE 8-4. DATA PROCESSING BLOCK DIAGRAM FOR THE COMBINED LASER DUAL-PLANE IMAGING CORRELOGRAPHY SENSOR.

aperture-plane complex field. This gives the field, $F = |F|\exp(i\psi)$, scattered by the object times a phase factor, $\exp(i\phi_a)$, due to atmospheric turbulence; the result therefore has the degraded phase $\psi+\phi_a$. Reconstruction algorithms described in Sections 6 and 7 would be appropriate for correcting the phase error, ϕ_a.

If all the aperture-plane snapshots are processed via the Imaging Correlography approach into a moderate-resolution image, then it should be possible to use that image, in conjunction with algorithms for setting upper limits ("locator sets") on the support of the object from the support of its autocorrelation, to determine a reasonably tight support constraint on the object.

The support constraint from Imaging Correlography plus the degraded phase from the Dual-Plane approach should make diffraction-limited resolution (ρ_d) coherent image reconstruction from a single snapshot of aperture-plane intensity easier (although the question of just how easy it would be has not yet been investigated). A priori knowledge of a support constraint, which might be known for a "friendly" object, would also make image reconstruction easier. With the collection of multiple frames, one has the option of choosing which snapshot to process, and the selection of one for which a strong glint is present and favorably positioned would make reconstruction easier still. Selection of an object that is highly nonconvex would also help. Noncoherent averaging of N reconstructed images would decrease the speckle contrast to $N^{-1/2}$, approximating an incoherent image for this and all the other coherent approaches that follow.

This approach would scale well for large distributed apertures since the two detection planes and the wavefront sensing could be done independently for each aperture; however, the reconstruction of the coherent images could suffer from the sparseness of the array.

8.3 COMBINED DUAL-PLANE AND INCOHERENT ATMOSPHERE SENSING

The approach employing active illumination that is most likely to succeed is (M1), a combination of the Laser Dual-Plane Sensor (C5) with an Incoherent Atmospheric Sensor. The Laser Dual-Plane Sensor, as described above, yields the degraded phase $\psi+\psi_a$. A wavefront sensor such as a shearing interferometer, operating with incoherent light from the object, yields the atmospheric phase, ψ_a. Subtraction of the atmospheric phase from the degraded phase yields ψ, the phase due to the object. Then an image is reconstructed by inverse Fourier transformation of $|F|exp(i\psi)$.

This combined method involves fairly complex hardware: two detector planes for the laser wavelength plus a wavefront sensor for the incoherent light. Furthermore it requires both laser and incoherent (e.g. sun) illumination. However, the phase retrieval part, finding the aperture-plane field by the Gerchberg-Saxton algorithm, is low risk and the wavefront sensor is already in place as part of the CI system at AMOS.

This approach would scale well for large distributed apertures; however phase retrieval will be needed for inter-aperture phase errors.

8.4 LASER FOCAL PLANE WITH INCOHERENT ATMOSPHERE SENSOR

This method (M2) is the same as the method above (M1) except that (A) the aperture plane detector is eliminated and (B) the ordinary circular aperture is masked to form an asymmetric-shaped aperture. Then instead of using the Gerchberg-Saxton algorithm to determine the aperture-plane field from the aperture and focal plane intensities, one uses the iterative transform algorithm to determine the aperture-plane field from the focal plane intensity and the aperture-shape support constraint. The atmospheric phase is subtracted and the image is formed as in (M1) above.

8.5 CONVENTIONAL LASER IMAGING APPROACH

Although it is unlikely to be practical, we have conceived of a means whereby it would be possible to reconstruct a diffraction-limited image from a single focal-plane intensity array in coherent light. It is like the Laser Conventional approach (C1) but with a long-coherence length laser with the addition of an aperture of special shape. First, as in (M2) above, one uses the iterative transform algorithm to reconstruct the aperture-plane field from the focal plane intensity and the aperture-shape support constraint. Then we use the iterative transform algorithm to reconstruct a coherent image from the modulus of the reconstructed aperture-plane field and a support constraint on the object. This method would require a much higher data signal-to-noise ratio than method (M1) or (M2) above, since the modulus of the aperture-plane field must be known more accurately for the iterative reconstruction of the image than if the phase is known for simple Fourier-transform reconstruction of the image. Nevertheless, this two-stage reconstruction approach is theoretically very intriguing.